Influence of Morphological and Structural Properties on Organic Photovoltaic Cells

Dissertation

der Mathematisch-Naturwissenschaftlichen Fakultät

der Eberhard Karls Universität Tübingen

zur Erlangung des Grades eines

Doktors der Naturwissenschaften

(Dr. rer. nat.)

vorgelegt von

Christopher Lorch

aus Tübingen

Tübingen

2015

Gedruckt mit Genehmigung der Mathematisch-Naturwissenschaftlichen Fakultät
der Eberhard Karls Universität Tübingen.

Tag der mündlichen Qualifikation:	04.02.2016
Dekan:	Prof. Dr. Wolfgang Rosenstiel
1. Berichterstatter:	Prof. Dr. Frank Schreiber
2. Berichterstatter:	Prof. Dr. Wolfgang Brütting

Contents

Part I

Fundamentals

Chapter 1

Introduction

Organic semiconductors (OSCs) are not only from the material science point of view an interesting material class, but also from the technological perspective. During the more than 100 years since this material class was reported for the first time [1, 2], the properties of OSCs have been studied thoroughly and OSCs found application in several different kinds of devices [3]. Some of these devices, like organic field effect transistors (OFETs) [4–6] or organic light emitting diodes (OLEDs), are already commercially available, whereas others, like organic memory devices [7–9] or organic photovoltaic cells (OPV cells) [10–14] are just about to cross the border to commercial availability. In particular, the latter are very interesting nowadays, in times of a changing view on energy production towards renewable energies [15, 16]. The possibilities of using flexible substrates, low-temperature preparation procedures, roll-to-roll processing and potentially low production costs make them an attractive alternative or complement to common inorganic solar cells. In addition, solar energy is a free input, therefore the overall efficiency is not necessarily the crucial fact, but rather the cheap production costs. Nevertheless, the best OPV cells show already efficiencies better than 11 % [17]. The processes for the energy conversion in OPV cells are slightly different compared to the processes in their inorganic counterparts. The main reason for this is the excitonic nature of the photon absorption due to the relatively low electric susceptibility χ_e in organic semiconductors. In 1986, Tang reported the first multilayer junction for OPV [18]. The application of two different materials, an electron donor and an electron acceptor, in an organic solar cell provides an energy level offset between the two materials which is necessary for a successful exciton dissociation into a free electron and a free hole (Figure 1.1).

The efficiency of OPV cells is closely linked to the structure and the morphology of the organic layer and thus it is crucial to understand the thin film growth. The basic principles of OPV cells, and the relation of structure and efficiency is described in more detail in Section 2.3.1. As already mentioned above, efficient OPV cells consist of at least two different organic materials, either in a planar geometry (*i.e.* one material on top of the other, so-called planar heterojunctions

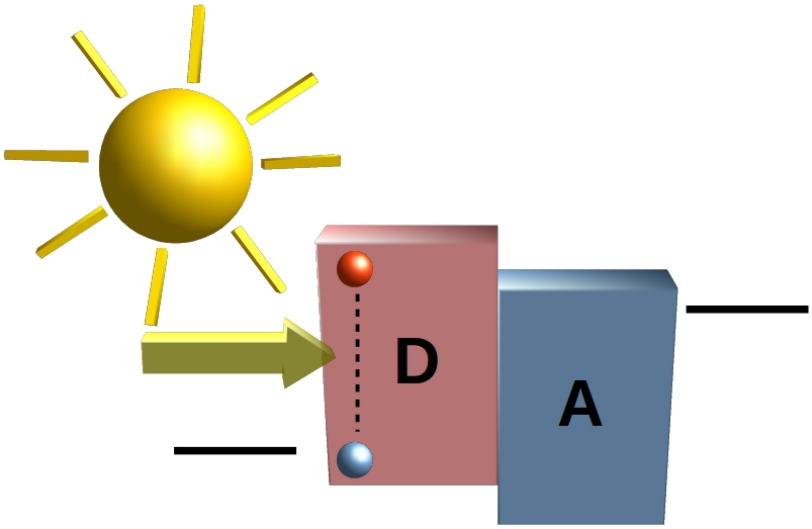

Figure 1.1: Sketch of an organic solar cell indicating the donor-acceptor junction.

(PHJs)) or in mixtures (so-called bulk heterojunctions (BHJs)) or a geometry combining both aspects (see Section 2.3.1). This implies that beside the growth of a pure organic material on a bare substrate it is necessary to also understand the growth on top of another organic material, the mixing behaviour and the growth of the mixtures. The latter can be quite different compared to the growth of the pure materials.

The term "growth" indicates already a process which is not in equilibrium. The continuous subsequent delivery of molecules, combined with the diffusion of the molecules on the substrate modify the energetic landscape permanently. Various parameters, including the substrate temperature, deposition rate and the molecular properties of the compounds, influence the growth. For a better understanding of the latter, real-time *in situ* experiments during the growth are necessary, allowing to follow transient effects and exclude the influence of ambient conditions [19, 20]. X-ray scattering techniques are suitable for non-invasive investigation of the film structure and morphology, directly during the growth [21–23].

Within this thesis the materials α-sexitiophene (6T), diindenoperylene (DIP) and buckminsterfullerene (C_{60}) were investigated. All of the three materials were successfully employed in OPV cells with both geometries BHJs as well as PHJs [24–28]. 6T and C_{60} are used as electron-donor and electron-acceptor, respectively. However, DIP due to its ambipolar transport properties [29] can be used either as acceptor or donor depending on the energy levels of the respective partner material.

The present thesis is organised as follows: The basics of organic thin films are introduced at the beginning in Chapter 2, including the fundamentals of organic

semiconductors and the growth of pure films as well as mixtures. Chapter 3 gives a short theoretical introduction to the methods employed for the investigation of organic films focussing on X-ray scattering techniques. Afterwards, the materials used are presented in more detail (Chapter 4). In Part II the results obtained are presented. There, first the growth of pure 6T is investigated, depending on the substrate temperature and the film thickness (Chapter 6). Furthermore, the growth of DIP and C_{60} on top of different 6T layers is described (Chapter 7), representing the same geometry as in PHJs. In Chapter 8 mixing of 6T and C_{60} at different substrate temperatures and mixing ratios is investigated. Furthermore, the effect of post growth annealing on the mixtures is compared to changes observed in pure 6T films. The growth of layers relevant for DIP:C_{60} BHJs is discussed in Chapter 9 and 10. There, first the effect of different modifications of the growth, *i.e.* substrate temperature, growth rate and substrate modifications, of equimolar mixtures is studied, providing methods to tailor the length scale of phase-seapartion, which is a crucially important property for the efficiency of OPV cells [30]. Thereupon, different mixing ratios are described. Chapter 11 summarizes the results and conclusions together with suggestions for the thin film growth of active layers for optimized OVP cells are presented. In addition, an outlook is given, suggesting further interesting topics.

Chapter 2

Organic Thin Films

The first part of this chapter is intended for a short introduction to the material class of organic semiconductors (OSCs). In the second part, the film growth of OSCs is described, first for single component thin films and then specifics of the films consisting of two different materials are elucidated.

2.1 Organic Semiconductors

The first organic semiconductors (OSCs) were reported at the beginning of the 20^{th} century [1, 2]. Since then, this material category has obtained significant attention and various different applications were proposed and put into practice [31–34]. In general, OSCs can be divided in two different groups, polymers and small molecules [35,36]. The two groups can mainly be distinguished according to their molecular size. Polymers consist of several repeating units, resulting in sizes of up to several 100 nms, whereas small molecules extend usually only over a few nanometers. Polymers are commonly processed using coating techniques from solutions, hence offering a cost efficient way of thin film preparation. However, polymer thin films (especially when prepared from solution) tend to show a higher degree of disorder, which can result in a lower charge mobility, compared to thin films of small molecules. The latter are usually prepared by organic molecular beam deposition (OMBD) techniques, resulting in a well controlled film growth [22,37,38]. In this thesis, only small molecule OSCs are used. For more information on polymers in general and on their application in organic solar cells it is referred to the literature [14, 39, 40].

2.1.1 Delocalized Electron System

OSCs are principally composed of several carbon atoms, and some specific OSCs may contain additionally other atoms, *e.g.* hydrogen, oxygen, sulphur, fluorine or others. The electrical conductivity in OSCs arises from a delocalized electron system in these materials due to the presence of alternating single and multiple

carbon-carbon bonds. In the case of alternating single and double bonds, as found for example in aromatic rings, the bonds between the carbon atoms are formed by sp^2-hybridisation, where the s- and p-orbitals of two carbon atoms build three energetically degenerated molecular σ-orbitals. These σ-orbitals are formed in the plane of the atoms. In contrast to this, the p_z-orbital is oriented perpendicularly to this plane and the different p_z-orbitals form collectively the molecular π-system. This resonant structure, originating from the alternating bond-types, leads to the delocalization of the electrons in the molecular π-system. Usually, theses electrons form the so called highest occupied molecular orbital (HOMO), which can be associated with the valence band in the case of inorganic semiconductors. The lowest unoccupied molecular orbital (LUMO)in OSCs corresponds to the conduction band in the inorganic counterparts. The electrons in the HOMO have the lowest binding energies and can therefore be excited to the LUMO by optical activation, *i.e.* by the absorption of a photon.

2.1.2 Interaction Between Organic Compounds

In this section the inter molecular interactions are summarized, which are important for the structure and ordering of organic compounds in pure films and blends. A more detailed description can be found in the literature [41–43].

In contrast to inorganic materials, in which the particles are often connected by either ionic, metallic or covalent bonding, the bonding in solids of organic compounds is usually dominated by electrostatic or van-der-Waals interactions [41]. In the case of non-polar molecules the intermolecular force with the strongest influence is dispersion (so-called London force [44]), arising from instantaneous polarization and formation of fluctuating dipoles. The inter molecular potential can usually be modeled by a Lennard-Jones potential

$$V_{LJ}(r) = \frac{B}{r^{12}} - \frac{A}{r^6}, \tag{2.1}$$

with r as the distance between the molecules and the constants B and A. The first term arises from repulsive interactions, such as Coulomb interactions and Pauli repulsion, preventing the crystal lattice of a collapse and the second term takes only the dipole-dipole interactions into account.

Most of the small molecule OSCs are non-polar (note that there are exceptions) with the consequence that the quadrupole moment is the first non-zero multipole moment. Fig. 2.1a depicts a schematic representation of the quadrupole moment of a benzene ring [45], which can be seen as prototypical molecule for OSCs with aromatic rings. In the gas or liquid phase two benzene molecules try to minimize the interaction energy originating in the electrostatic forces and arrange themselves in a perpendicular face-to-edge (T-shape) orientation (Fig. 2.1b) [45]. The face-to-face orientation (Fig. 2.1c) is favoured by van-der-Waals forces since in this case the polarizable contact area of the two molecules is maximized. In

the case of benzene the electrostatic interaction is dominating the van-der-Waals influence [45]. Obviously, in a solid usually more than two molecules are con-

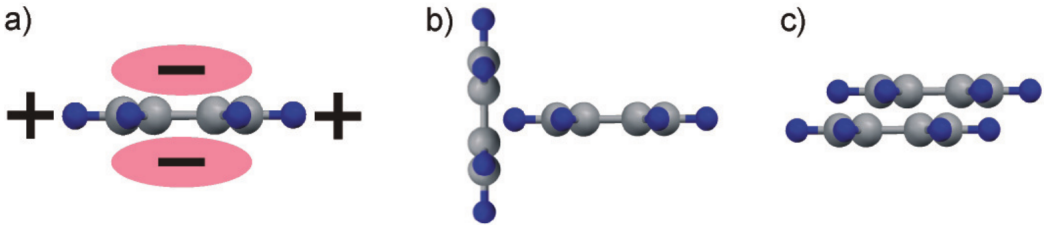

Figure 2.1: a) Schematic representation of the quadrupole moment of benzene. b) Face-to-edge configuration formed of two benzene molecules in the liquid or gas phase. c) Face-to-face configuration of two benzene molecules, maximizing the polarizable contact area of the two molecules. Image taken from Ref. [46].

sidered. The crystal structure, which is formed by the molecules is the result of minimization of the overall free energy of the system. The minimization of the combination of both types of interactions the electrostatic one as well as the van-der-Waals one leads often (but not always) to the formation of a so-called herringbone structure (depicted in Fig. 2.2 [47, 48]).

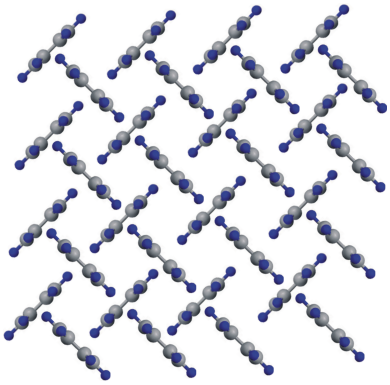

Figure 2.2: Benzene molecules arranged in a herringbone structure.

The description presented above is limited to molecules of just one material. As soon as two or more materials are mixed together further interaction effects have to be considered. Different effects occurring upon mixing are described in Sec. 2.2.3. Note that there is a significant difference in the quadrupole moment for molecules in which the hydrogen atoms are replaced by fluorine atoms. Fluorine is strongly electronegative and withdraws the electrons from the carbon ring, leading to an inversion of the signs in the quadrupole moment. In particular for mixtures of molecules and their perfluorinated counterparts the different alignment of the quadrupole moments leads to interesting and relevant effects for the

mixing scenario. In this thesis no fluorinated molecules are studied, therefore it is referred to the literature for further information and examples [49–52].

2.2 Organic Thin Film Growth

There are several different ways to prepare organic thin films, *inter alia*, organic molecular beam deposition (OMBD) [22, 37, 38], spin coating [53], doctor blade coating [54] and inkjet printing [55]. Small organic molecules are usually poorly soluble in organic solvents and are mostly very stable against high temperatures. Due to these properties, most often OMBD is used for the preparation of thin films of small organic molecules. This method allows the well-controlled preparation of high-quality thin films and the fine adjustment of preparation parameters.
In the following, first details of the growth of a single organic material using OMBD are described. Afterwards, specifics of the growth of one organic material on top of another organic material are outlined and finally aspects of the simultaneous deposition of two organic molecules and the different mixing scenarios of the materials are introduced.

2.2.1 Growth of One Single Organic Material

2.2.1.1 Processes During Organic Molecular Beam Deposition

Already from the terminology it is clear that the "growth" of organic thin films is a dynamic process and not in equilibrium. In OMBD the organic molecules are usually deposited from some type of evaporator, ideally from Knudsen cells [56] that are directed towards a substrate. This results in a flux of new molecules impinging on the substrate, where different processes can occur. Figure 2.3 schematically depicts the various processes occurring during the film growth via OMBD. Basically, molecules arriving on the substrate perform one or several of the steps listed below. The probability for the different steps depends essentially on the interaction energies between the molecules themselves, on the interaction energies between the surface and the molecules, and on the kinetic energy of the molecules. Please note that these processes are described for atomic like particles. Peculiarities of extended molecules are illustrated in Sec. 2.2.1.3.

- **Condensation** – It is possible that the arriving molecule attaches itself immediately to the substrate or the already existing film, directly at the position where it impinges on the sample. This is most likely the case if the kinetic energy of the molecule itself is relatively low, *e.g.* in the case of a low substrate temperature, and constitutes usually the last step of a molecule in the film formation process.

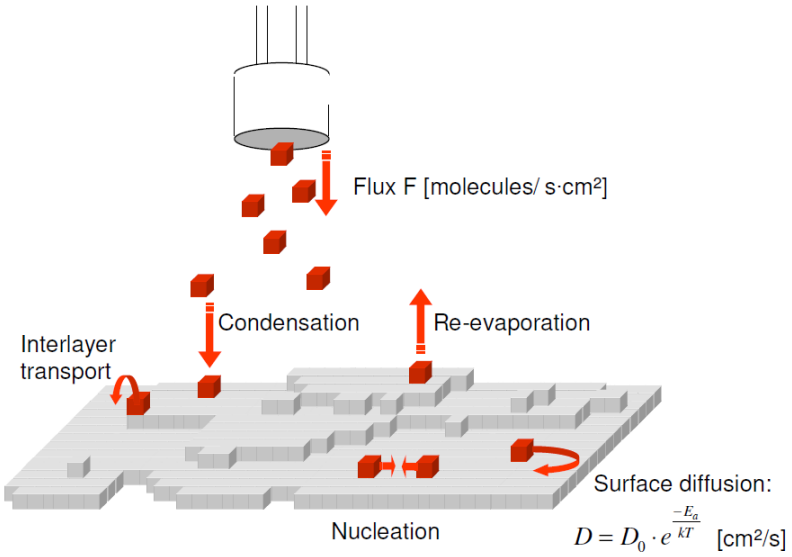

Figure 2.3: Schematic representation of the various processes occurring during the film growth via OMBD. The processes are idealized for atomic like particles. Peculiarities of extended organic molecules are mentioned in the text. Image taken from Ref. [23].

- **Re-evaporation** – Molecules can desorb from the sample again, after reaching it. This happens for example if the kinetic energy of the molecules is too high. This process is usually not desired during thin film growth.

- **Surface diffusion** – After a molecule reaches the sample it might have enough kinetic energy to diffuse on it and to attain an energetically more stable position. In the case of multilayer growth, a molecule can reach step-edges between different layers during this diffusion process. If the molecule is on the higher layer, this might be followed by a hopping down to the subjacent layer if the so-called Ehrlich-Schwoebel barrier can be overcome [57, 58] or that the molecule is captured at the step-edge. The Ehrlich-Schwoebel barrier can strongly depend on the film thickness [59,60]. If the molecule is on the lower layer it might either step-up to a higher layer, attach to the step-edge or diffuse along it, again the probabilities of the single options depend on the interplay of the different interaction energies.

- **Nucleation** – If the interaction potential between the single molecules is an attractive one, like in the case of van-der-Waals-type of interactions, the formation of pairs or aggregates is favored. So, if molecules meet each other after diffusing they might form aggregates which reduces the probability of further diffusion or desorption.

2.2.1.2 Thin Film Growth – Growth Modes

In this section the most relevant facts of thin film growth and the different growth modes are summarized. A more detailed discussion of the topics can be found in the literature [61–66].

As mentioned previously, crystal or thin film growth is a non-equilibrium kinetic process and the resulting film or crystal depends strongly on the occurring processes which are described in Section 2.2.1.1. There are different approaches to explain and describe thin film growth, either by wetting theory [67, 68] or by the interaction and binding energies of atoms on surfaces or in the bulk, respectively [69]. These descriptions have the drawback that they consider only equilibrium energies, and, therefore, can be seen only as approximations. In this section the classical wetting theory of liquids is used to describe the thin film growth, following Ref. [67].
The free energy $U(t)$ of a liquid film of thickness t can be expressed as

$$U(t) = \gamma_{sl} + \gamma_{la} + P(t). \tag{2.2}$$

γ_{sl} and γ_{la} are the tensions at the solid/liquid and at the liquid/air (or vacuum) interface, respectively. $P(t)$ describes the long range van-der-Waals interaction

$$P(t) = \frac{A}{12\pi t^2}, \qquad \text{with} \qquad l_m \ll t. \tag{2.3}$$

Here, $A = A_{sl} - A_{ll}$ is the difference between the Hamaker constants of the solid-liquid species and of the liquid species. Two important points are to note: A can be larger or smaller than 0 and this theory holds true only for film thicknesses larger than the molecular size l_m.
In the case of a very small film thickness, $U(t)$ is basically reduced to the spreading coefficient S on a dry substrate,

$$P(t \to 0) = S = \gamma_{sub} - \gamma_{sl} - \gamma_{la}. \tag{2.4}$$

γ_{sub} is the surface energy of the substrate. A and S are independent and both can be positive or negative. This leads to four possible combinations of the two parameters, resulting in different wetting/growth scenarios:

- $S > 0$ and $A > 0$: For these parameters complete wetting of the substrate is observed. In the case of molecular thin film growth, this corresponds to the Frank-van-der-Merwe (or layer-by-layer) growth mode (Figure 2.4a).

- $S > 0$ and $A < 0$: In this case the free energy $U(t)$ has a minimum at a certain thickness t_m; referred to as *pseudo* partial wetting. In the case of a classic liquid, this leads to a droplet with a finite contact angle and a completely covered substrate. In thin film growth this corresponds to the Stranski-Krastanov (layer-plus-island) growth (Figure 2.4b).

- $S < 0$ and $A > 0$: In this case a finite contact angle of the film on the bare substrate is observed, that is partial wetting. In thin film growth this scenario corresponds to the direct formation of islands, *i.e.* Volmer-Weber growth (Figure 2.4c).
- $S < 0$ and $A < 0$: This case can be either *pseudo* partial wetting or partial wetting. In this case, the concrete values of A and S have to be considered, leading to either a minimum in $U(t)$, which results again in the Stranski-Krastanov growth, or to a monotonic increase of $U(t)$, which basically results in dewetting.

For some typical organic molecules, the literature reports values of the van-der-Waals interaction constant [70, 71] which allow the calculation of the homomolecular Hamaker constant, which refers to A_{ll} mentioned above (Appendix A). The value for the rod-like molecule pentacene (PEN) is $\sim 2.1002 \cdot 10^{-19}$ J ($\widehat{=}126.475\,\mathrm{kJ/mol}$) and for C_{60} one obtains $\sim 1.8144 \cdot 10^{-19}$ J ($\widehat{=}109.264\,\mathrm{kJ/mol}$). These values are relatively large compared to the values of SiO_2 [72] with $A_{SiO_2} = 6.5 \cdot 10^{-20}$ J. An approximated Hamaker constant for the interaction between SiO_2 and the organic material can be calculated by $A_{SiO_2-\mathrm{organic}} \simeq \sqrt{A_{SiO_2} A_{\mathrm{organic}}}$, which corresponds to A_{sl} mentioned above. For the two examples discussed here, A_{SiO_2} is smaller than A_{organic} and therefore $A < 0$ which should result most of the times in a Stranski-Krastanov type growth.

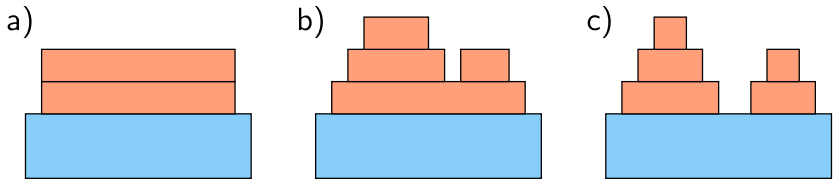

Figure 2.4: Schematic of the different growth modes in organic thin film growth: a) Frank-van-der-Merwe, or layer-by-layer growth, b) Stranski-Krastanov, or layer-plus-islands growth, c) Volmer-Weber, or island growth.

2.2.1.3 Growth of Organic Molecules

The processes described above in Section 2.2.1.1 are for atomic like particles. In the case of organic molecules additional aspects, due to their spacial extension and electrical multipole interactions have to be considered. In the following, aspects specific to extended organic molecules are summarized. These deliberations are mainly based on Ref. [38].

Organic molecules have internal degrees of freedom since they are extended objects. This implies that the molecules can take different orientations during the growth (Figure 2.5a). For example, rod-like molecules can basically be oriented

in lying-down or standing-up configuration (or with a certain angle to the surface normal). Obviously, the orientation of the molecules has significant influence on the macroscopic physical properties of the film, *e.g.* exciton diffusion, conductivity or absorption [73, 74]. Differences in the energies between standing-up and lying-down configurations in the thin film growth can also lead to transitions from one orientation to the other during the film growth process [75–78].
Moreover, organic molecules have vibrational degrees of freedom. These vibrations can change the diffusion behavior, the adsorption and can also have an influence on the interactions with the substrate or other molecules.

The interactions between organic molecules are mostly of a van-der-Waals like type (Section 2.1.2) and hence different from the ones dominant in the atomistic like growth. These 'softer' interactions are the reason that organic molecules can potentially accommodate more strain than atoms, and therefore critical thicknesses for changes to a different growth mode (due to accumulated strain effects) are usually higher, compared to 'hard' particles [76, 79].
Furthermore, the relatively low interaction potentials can lead to polymorphisms in organic thin films [80–83].
The lower interaction-energies per atom are the reason that usually the molecules are processed at a lower temperature scale, and also the relevant temperature for diffusion processes is usually significantly lower than for inorganic materials. However, the interaction energy summed over a whole molecule is comparable to the one of absorbing atoms.
The surface potential of organic thin films is usually weaker than the one of inorganic substrates, since the molecules are mostly of a closed-shell type and form van-der-Waals-type crystals without dangling bonds.
In the case of strongly interacting substrate, the diffusion of the organic molecules on the substrate might be hindered, which leads to films with a low structural ordering. Due to the sizes of organic molecules, the dimensions of their unit cells are usually larger than the ones of commonly used substrates. This leads to a smearing-out of the lateral variation of the substrate potential and reduction of the effective corrugation of the substrate experienced by the molecules, compared to atomistic adsorbates.
In addition, the mismatch between the lattice structure of the substrate and the molecules can lead to an increase in the number of translational domains (Figure 2.5b). The fact that organic molecules usually crystallize in low-symmetry structures can further increase the number of domains. Each domain boundary can be seen as a kind of disorder, having an impact on the charge-transport properties of the films [84, 85].

The facts mentioned above can also influence the interactions between single molecules or the molecules and the substrate and therefore have a direct influence on the diffusion and the other processes mentioned in Section 2.2.1.1. This leads to changes in the growth dynamics and not only to the final static film structure.

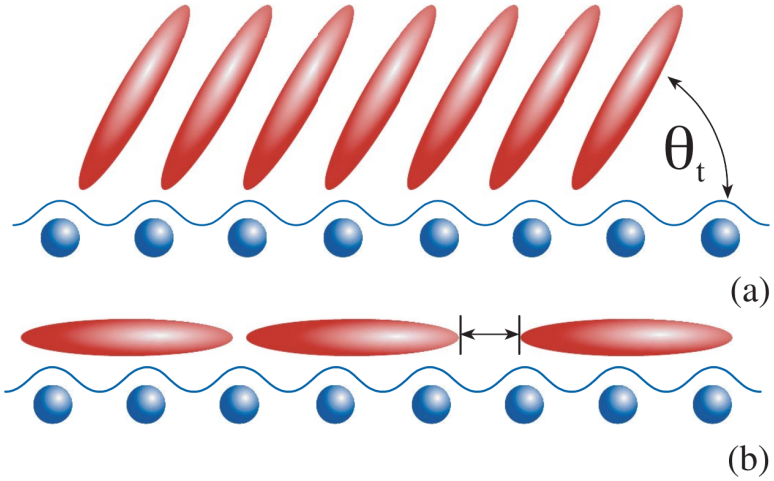

Figure 2.5: Schematic of specific issues related to the growth of organic molecules. a) Rod-like molecules on a substrate, depicting the possibility of different orientations. b) Organic molecules being larger than the unit cells of the substrate can result in translational domains and a smearing-out of the substrate potential. Image taken from Ref. [38].

2.2.2 Growth of One Organic Material on Top of Another Organic Material

This and the following section should give a short introduction into the growth of systems consisting of two different organic compounds. A more detailed study can be found in Ref. [86] and the references therein.
Heterojunctions, in which one material is deposited on top of the other are interesting for organic photovoltaic (OPV). This geometry is called planar heterojunction (PHJ) and mostly found in OPV cells, which consist of small molecules. In this case the preparation of the organic layers is usually performed using OMBD, resulting in a well defined film structure.
The growth of the overlayer can strongly depend on the film properties of the materials underneath. The interactions between different organic materials might be drastically different compared to the ones between a bare substrate and an organic compound and can have a strong influence on the growth [86]. These interactions depend *inter alia* on the type of energetic arrangement, *i.e.* whether dipole interactions or higher-order electronic interactions dominate the van-der-Waals interaction, on the steric compatibility of the materials, which can lead to strain in the growth of the overlayer, and on the orientation of the bottom material, *e.g.* lying-down or standing-up orientation of rod-like molecules. These different aspects can lead to various scenarios in the growth of the overlayer, which can include the following:

- **Epitaxial growth:** In organic heterostructures, the observed effects are usually weaker than the ones typically described by the term epitaxial growth in inorganic heterostructures (where at least one crystallographic orientation in the overlayer is adopted from the substrate) [87], since usually the unit cells of the two organic materials, and hence the surface potential, do not match perfectly. Basically, the in-plane (azimuthal) orientation of the bottom layer can be adopted by the molecules in the overlayer, as reported for α-sexithiophene (6T) and *para*-sexiphenyl (6P) [88–90]. Furthermore, for sphere-like molecules like C_{60} a growth, following chains of 6T [91–93] or 6P [94] are reported.

- **Orientation of molecules in the toplayer:** For rod-like molecules one can generally distinguish between molecules in the standing-up and lying-down orientation. In PHJs, molecules in the overlayer can adopt the orientation of the molecules in the bottom layer, which might be different to the one, in which these molecules would usually arrange [95].

- **Roughness evolution:** For the roughness evolution of an organic film during the deposition of a second material on top basically all three possible scenarios are observed: 1) A smoothing of the surface can occur, if the second material fills the voids between the islands of the first material [96]. 2) The roughness evolution of the organic layer is almost independent of the bottom layer [97]. 3) The roughness increases faster than in the case of a growth on an inorganic substrate, which can be related to either a preferred nucleation at step edges [98, 99] or to dewetting of the second material [100, 101].

Additionally, the growth of a second material on top of an organic thin film can also alter the film structure of the bottom film, as, for example, reported for diindenoperylene (DIP) on top of fluorinated cobalt-phthalocyanine, where a reconstruction of the layers close to the interface occurs [100, 102].

2.2.3 Growth of Mixed Films of Two Organic Materials

Mixtures of at least two organic compounds show interesting effects during the growth of thin films. Furthermore, under certain circumstances such mixtures can be successfully employed in OPV cells, where this geometry is usually called bulk heterojunction (BHJ). The mixing scenario of two organic compounds depends on several aspects, *inter alia* on the steric compatibility and the interaction energies between the two materials, but also between the materials and the substrate, and also on the preparation conditions, such as substrate temperature and deposition rate. Following a mean-field approach the free energy of a mixture can be written

as [86, 103, 104]:

$$\frac{F_{mix}}{k_B T} = x_A \ln x_A + x_B \ln x_B + \chi x_A x_B. \tag{2.5}$$

Here, x_A and x_B are the concentrations of the two materials and χ is a dimensionless interaction parameter depending on the interaction energies between molecules of the same species W_{AA}, W_{BB} and of the different species W_{AB}, respectively, and can be expressed as:

$$\chi = \frac{1}{k_B T} \left[W_{AA} + W_{BB} - 2W_{AB} \right]. \tag{2.6}$$

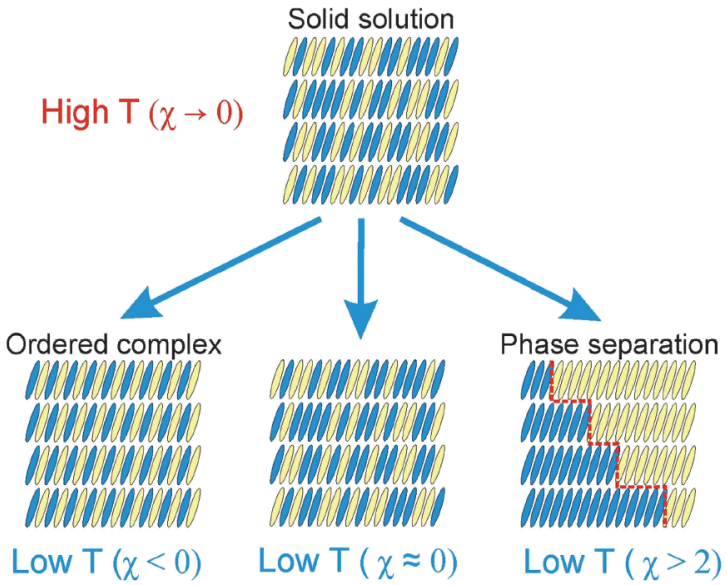

Figure 2.6: Sketch of the different mixing scenarios usually observed in binary mixtures of organic semiconductors. At high temperatures the molecules usually arrange in a solid solution, whereas at lower temperatures, depending on the intermixing parameter χ, either a mixed crystal, a solid solution or phase separation can occur. Image taken from Ref. [86].

Please note that this equation does not depend on the shape and dimensions, *i.e.* steric compatibility, of the two molecules. In general, a good mixing behavior is favored by a good steric compatibility. Depending on the value of the interaction parameter χ, three different mixing scenarios can occur (Figure 2.6):

- **Solid solution:** At high temperatures or if the interaction energies between the two species are similar to the ones within one specie (*e.g.* $\chi \approx 0$) the formation of a solid solution is favored. In this case a molecule of one species can be substituted by one of the other. Such a mixing can usually be observed in systems of compounds with a similar shape and energetic arrangement, like PEN and DIP [105].

- **Phase separation:** If the two materials are sterically incompatible or the interaction energies within the single materials are significantly more attractive than the interaction between the different species ($\chi > 2$), usually a phase separation of the materials is observed [106].
- **Ordered complex:** An ordered complex is usually formed if the interaction energies between the two different materials are higher than the interaction energies within one species and the materials are sterically compatible [105, 107, 108].

2.3 Application of Organic Semiconductors

OSCs can be used in a variety of applications and devices. Some of these are already commercially available (like organic light emitting diodes) but others are still in the early stages (like organic novolatile memory devices). In this section especially organic photovoltaic cells (OPV cells) and the photon-to-current conversion process are described. Other important types of OSC applications are shortly introduced. However, the latter are not treated in full details and further information can be found in the literature [35, 109].

2.3.1 Organic Solar Cells

In this section, the fundamentals of OPV cells are described. Yet, a complete discussion of this device type is beyond the scope of this part and for further information, it is referred to the literature [11, 14, 110–113].

Basically, two different architectures are common. On the one hand, the donor and the acceptor material might be deposited on top of each other, resulting in a planar geometry, which is called planar heterojunction (PHJ). On the other hand, the donor and acceptor can be intermixed in one film, which is called bulk heterojunction (BHJ). Independent of the architecture, the energy conversion in an OPV cell can be divided in four sub-processes [12], each having a specific efficiency. The product of all the specific efficiency is the overall efficiency, also known as internal quantum efficiency (IQE).

$$\eta_{int} = \eta_{Abs} \cdot \eta_{ED} \cdot \eta_{CT} \cdot \eta_{CC}. \tag{2.7}$$

The efficiencies of the single steps can be described as follows:

- **Photon absorption and exciton generation η_{Abs}:** This describes the probability to absorb a photon and convert it into an exciton, which is a bound electron-hole pair.
- **Exciton diffusion η_{ED}:** The formed exciton needs to diffuse to the donor-acceptor interface, where it can be dissociated into a free electron and a free hole.

- **Charge separation** η_{CT}**:** At the interface, the exciton can be first dissociated into an electron and a hole and then separated into the two different materials.

- **Charge collection** η_{CC}**:** Finally, the separated charges need to reach the electrodes and the charges need to be extracted.

The different processes in an energetic landscape of a donor-acceptor interface are schematically depicted in Figure 2.7.

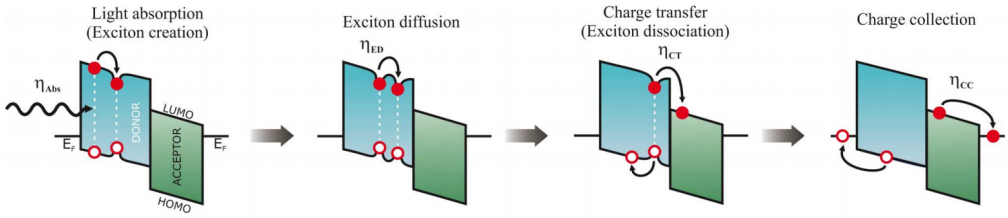

Figure 2.7: Schematic of the processes relevant for the energy conversion in an organic solar cell. LUMO and HOMO stand for the lowest unoccupied molecular orbital and for the highest occupied molecular orbital, respectively. E_F denotes the Fermi energies of the contacts. The different process steps are described in the text together with their respective efficiencies. Image taken from Ref. [30].

For most of the specific efficiencies the structure of the active layer plays a crucial role. For the absorption of photons the orientation of the single molecules is crucial. The coupling of the incoming light to the molecules depends on the relative orientation of their transition dipole to the wavevector of the incoming light. Typically, the exciton diffusion length in organic materials is of the order of 10 nm. Only excitons which are created within a certain distance to the donor-acceptor interface can diffuse to it. After the exciton has reached the donor-acceptor interface and is separated there into an electron and a hole, the two charge carriers need to be extracted over the electrodes. For this process well-defined percolation paths from the donor-acceptor interface to the electrodes are beneficial.
In Section 11.5 in the Summary Chapter the relationship between the efficiencies of the single steps and the relevant structural features are elaborated in more detail and suggestions are made, how the structure might be optimized.

2.3.2 Further Organic Electronic Devices

Beside OPV cells, OSCs can be used for different other organic electronic devices. In the following only a short overview of the most important ones is given. For further details it is referred to the respective literature mentioned in the single

paragraphs. The benefits of almost all these devices are potential low-cost production costs and utilization of flexible substrates, which results in new fields of application [33, 109].

- **Organic light emitting diodes (OLEDs)** are devices which are based on the inverse process of the photo current generation in OPV cells. Commonly, at least two different organic materials are used in a planar geometry. OLEDs are ready for the market, however, they are still subject of basic research for further improvement, especially to enhance their lifetime [114].
- **Organic field effect transistors (OFETs)**: The structure of OFETs is quite similar to their inorganic counterparts. They are especially promising for the use in radio frequency identification tags (RFIDs) and in electronic paper. However, due to smaller mobilities in the OSCs, their switching times are lower than the ones of inorganic devices [6, 115, 116].
- **Organic spintronics:** Organic materials are promising for spintronic applications due to their relatively long spin relaxation times originating in the usually weak spin orbit coupling. Potential applications are magnetic random access memories due to spin-polarized transport characteristics [117].
- **Organic nonvolatile memory devices** are interesting for completely printed electronic structures. Basically, switching mechanisms based on light-material interactions as well as reprogrammability by voltage or current have been demonstrated. In particular, metallic particles embedded in an organic host matrix might be potentially interesting [9, 118, 119].

Chapter 3

Methdods

X-ray scattering techniques are a well established and, under controlled conditions, non-invasive technique to measure and characterize organic thin films. By using special Beryllium windows and suitable vacuum equipment these techniques can be applied directly under vacuum conditions, therefore allowing the *in situ* and real-time investigation of the film growth. The description of the X-ray scattering techniques are based on Refs. [120–122] and further details can be found therein.

3.1 X-ray Scattering Techniques

3.1.1 Scattering at Interfaces and Thin Films

Generally, X-ray scattering provides very powerful methods to investigate the structure of interfaces. The reflectivity of an ideal flat interface, similar to common optics, can be described by the Fresnel equations, which can be simplified for X-rays even further (see below).
X-rays are basically nothing else but electromagnetic waves with a wavelength in the order of an Ångström. The electric field of such a wave at a certain point $\vec{r}$ can be written as

$$E(\vec{r},t) = A_0 \exp(i\vec{k}\vec{r} - \omega t). \tag{3.1}$$

where A_0 is the maximal amplitude, $\vec{k}$ the wavevector in direction of the propagation of the wave and ω the frequency of the wave. The magnitude of the wavevector $\vec{k}$ is the wavenumber k and depends as follows on the wavelength λ:

$$k = \frac{2\pi}{\lambda}. \tag{3.2}$$

3.1.1.1 Reflection and Absorption

Again, similar to visible light the propagation of X-rays in vacuum or a medium can be described with the help of the refractive index n:

$$n = 1 - \delta + i\beta, \tag{3.3}$$

where δ is the dispersion and β the absorption. If the energy of the X-ray beam is far away from an absorption edge of the scattering material, δ can be expressed as follows:

$$\delta = \frac{2\pi}{k^2}\rho_{el}r_0, \tag{3.4}$$

with ρ_{el} being the electron density of the material and r_0 the Thomson scattering length, or classical electron radius with

$$r_0 = \left(\frac{e^2}{4\pi\epsilon_0 mc^2}\right) \approx 2.82 \cdot 10^{-5}\text{Å}. \tag{3.5}$$

In condensed matter, ρ_{el} is usually found to be around 1 electron/Å^3. For X-rays with k around 4 Å^{-1}, δ results in something of the order 10^{-6} and is always positive. Therefore, it follows directly that $\Re(n)<1$ in condensed matter.
The absorption β can be written as a function of the material specific absorption coefficient μ via

$$\beta = \frac{1}{2k}\mu. \tag{3.6}$$

μ arises from effects like photoelectron generation and Compton scattering in the material and is a measure of the decrease of the intensity ($I = I_0 e^{-\mu z}$) of the wave travelling a distance z through the material. Typically for organic materials β is in the order of 10^{-9}.

3.1.1.2 Snell's Law and Fresnel Equations

At the interface between vacuum and a dense medium Snell's law describes the beam path of an incident wave with wavevector k_I and a transmitted wave (wavevector k_T) and relates the incident angle α and the transmitted angle α'

$$\cos\alpha = n_{\text{medium}}\cos\alpha'. \tag{3.7}$$

As seen above, in the X-ray regime $n < 1$ inside a dense medium. From this follows that there is an incident angle α_c below which the incident wave is reflected almost completely and the intensity of the transmitted wave is almost 0 (so to say $\alpha' = 0$). δ and β in $n = 1 - \delta + i\beta$ are usually distinctively smaller than

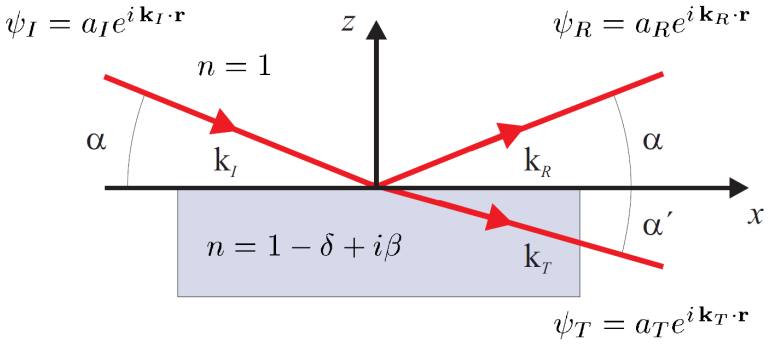

Figure 3.1: Beam path of X-rays at the interface between two media, *e.g.* vacuum and a dense medium. Image taken from Ref. [120].

unity, allowing us to limit α and α' to small values and hence to use the Taylor expansion of the cosine, leading finally to

$$\alpha_c = \sqrt{2\delta}. \tag{3.8}$$

The ratio of the amplitudes of the reflected, transmitted and incident wave can be calculated via the Fresnel equation for the X-ray regime

$$r = \frac{a_R}{a_I} = \frac{\alpha - \alpha'}{\alpha + \alpha'}, \tag{3.9}$$

$$t = \frac{a_T}{a_I} = \frac{2\alpha}{\alpha + \alpha'}, \tag{3.10}$$

where r is the amplitude reflectivity and t the transmittivity. The corresponding intensity of the reflected (R) or transmitted (T) wave are the absolute squares of the amplitude reflectivity and transmittivity, respectively. Here, α' is a complex number for a given incidence angle α. The intensity of the transmitted wave is decreased by a factor of $1/e$ within the penetration depth Λ:

$$\Lambda = \frac{1}{2k\Im(\alpha')}. \tag{3.11}$$

r, t and Λ depend on the incident angle α, the electron density of the material, the absoption in the medium and on the wave vector. Basically, one can distinguish between two limiting cases:

- $\alpha \ll \alpha_c$: If the incident angle is smaller than the critical angle, the reflected wave is out-of-phase with the incident wave and the transmitted wave propagates along the surface with a penetration depth of $\Lambda = 1/2k\alpha_c$. This so called evanescent wave can be used for the in-plane characterisation of thin films, via grazing incidence X-ray diffraction (GIXD) (Section 3.1.7).

- $\alpha \gg \alpha_c$: In this case the reflected wave is in phase with the incident wave and the intensity of the reflected wave R falls as $R \approx (\alpha_c/2\alpha)^4$; the penetration depth is $\Lambda = \alpha/\mu$, hence there is almost complete transmission.

3.1.2 Reflection from Multiple Layers - Parratt's Formalism

The considerations above were taking only one interface, namely the one between vacuum or air and a dense medium, into account. However, real samples can usually be modelled by several interfaces, or slabs having a finite thickness. In this case, the reflection, and also higher orders of the wave reflected back inside the medium, have to be considered. Figure 3.2 indicates schematically the beam path and resulting reflectance of (a) a slab with infinite thickness and (b) with a finite thickness. As indicated in the right hand part of Figure 3.2b) the total amplitude of the reflectivity can be described as a geometric series, which can be evaluated to

$$r_{slab} = r_{01} + t_{01}t_{10}r_{12}e^{i2k\sin(\alpha_1)\Delta}\frac{1}{1 - r_{10}r_{12}e^{i2k\sin(\alpha_1)\Delta}}. \tag{3.12}$$

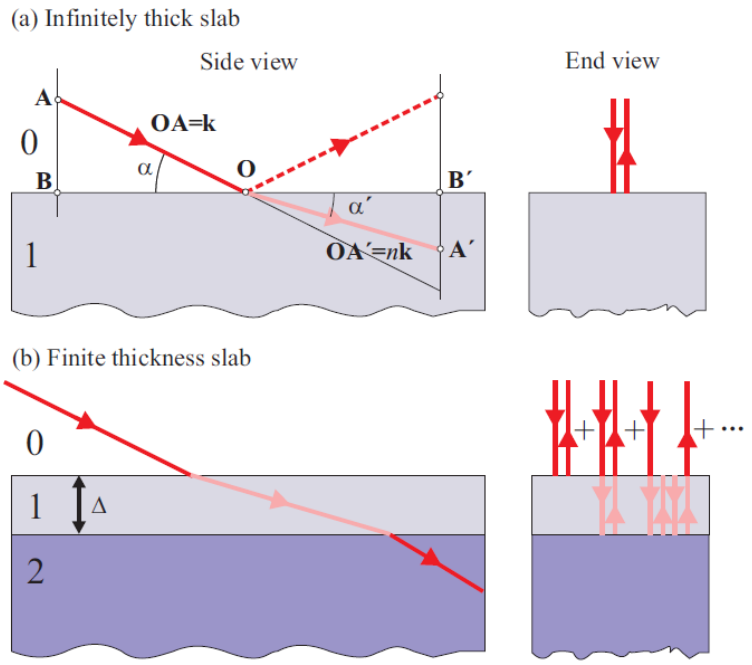

Figure 3.2: Beam path and total reflectance of a) a slab with an infinite and b) a finite thickness. Image taken from Ref. [120].

Here, r_{01} is the amplitude of the reflection at the top interface between air and the medium, r_{12} is the reflection at the interface between the bottom of the slab and the substrate, and t_{01} and t_{10} are the transmissions at the interface 0 to 1 and 1 to 0, respectively. For adding up the waves it is very important not to forget the phase factor $e^{i2k\sin(\alpha_1)\Delta}$ with the slab thickness Δ.

The idea of slabs can be extended to describe multilayer samples, as usually investigated *e.g.* in organic samples (where the molecules might stack up on top of each other, forming bilayers of an electron dense part and a gap with a lower electron density in between). In 1954, L. G. Parratt published a recursive algorithm to calculate the reflectivity of a sample consisting of N layers, each with a refractive index $n_j = 1 - \delta_j + i\beta_j$ and a thickness Δ_j on top of an infinite thick substrate [123]. Analogously to the reflection at the top of a layer (Section 3.1.1.2) the reflectivity amplitude between the N^{th} layer and the infinite thick substrate (where no multiple reflections occur)

$$r'_{N,\infty} = \frac{\alpha_N - \alpha_\infty}{\alpha_N + \alpha_\infty}. \tag{3.13}$$

As a next step, the reflectivity of the interface between the N^{th} and the $N-1^{th}$ layer can be calculated using Equation (3.12) and further simplification, via the following expression

$$r_{N-1,N} = \frac{r'_{N-1,N} + r'_{N,\infty} e^{i\Delta_N 2k_N \sin(\alpha_N)}}{1 + r'_{N-1,N} r'_{N,\infty} e^{i\Delta_N 2k_N \sin(\alpha_N)}}. \tag{3.14}$$

This series can be continued for the interface between the $N-2^{th}$ and $N-1^{th}$ layer and so on, up to finally obtain the total reflectivity amplitude $r_{0,1}$ from the interface between air/vacuum and the top of the entire sample.

3.1.3 Extension from Flat to Graded Interfaces

The interfaces in Section 3.1.1.2 and 3.1.2 have been considered to be perfectly sharp. However, most real-world samples cannot be described with this simplification, but the interfaces show a certain roughness which can be described as a graded interface with a normalised electron density profile $f(z)$, for which $f(z) \to 0$ as $z \to -\infty$ has to be fulfilled. The amplitude reflectivity for a graded interface can be expressed as

$$r(2k\sin(\alpha)) = r_F(2k\sin(\alpha))\phi(2k\sin(\alpha)), \tag{3.15}$$

where $r_F(2k\sin(\alpha))$ is the Fresnel reflectivity and $\phi(2k\sin(\alpha))$ describes the gradation and is defined as

$$\phi(2k\sin(\alpha)) = \int_{-\infty}^{\infty} f'(z) e^{i2k\sin(\alpha)z} dz. \tag{3.16}$$

The Parratt formalism presented in Section 3.1.2 and the deliberations on graded interfaces within this Section can be combined and implemented in (computer) algorithms to model reflectivity curves.

3.1.4 X-Ray Reflectivity - XRR

X-ray reflectivity (XRR) is a method to probe the structure of a sample perpendicularly to the substrate surface. The scattering geometry is depicted in Figure 3.3a). In the case of XRR, the incident angle Θ_{in} and the exit angle Θ_{out} are the same. The scattering vector $\vec{q}$ is purely perpendicular to the substrate surface (the in-plane components are both zero) and the out-of-plane component q_z can be expressed as

$$q_z = \frac{4\pi}{\lambda} \sin\left(\frac{\Theta_{in} + \theta_{out}}{2}\right). \tag{3.17}$$

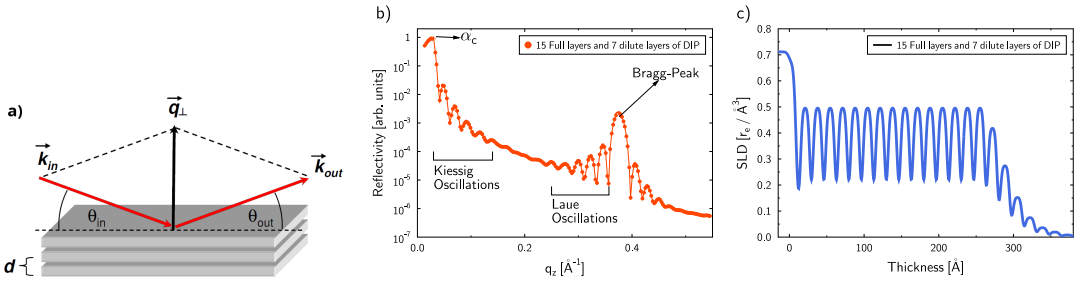

Figure 3.3: a) Scattering geometry of an X-ray reflectivity (XRR) measurement. The image is taken from Ref. [23] and modified. b) Simulated data of an XRR measurement of 15 completely filled and seven dilute layers of diindenoperylene on native SiO. c) Electron density profile of the 15 completely filled and seven dilute diindenoperylene layers which can be extracted from the data in (b) by fitting it using Parratt's formalism.

An exemplary XRR dataset of 15 completely filled and seven diluted diindenoperylene layers is shown in Figure 3.3b). From the data several information of the sample can be extracted:

- α_c – The critical angle α_c and therefore the total reflection edge are a measure of the averaged electron density of the sample.

- **Kiessig oscillations** – The oscillations in the low q_z range stem from interference effects from the top of the sample and of the substrate [124]. So the spacing between these oscillations can be used to calculate the averaged total film thickness. These oscillations are damped out with increasing surface roughness of the film, hence by fitting them it is possible to extract the averaged film roughness.

- **Bragg peak** – Bragg peaks arise from constructive interference of an out-of-plane well ordered lattice. In organic thin films this kind of lattice arises

from an ordered stacking of the single molecules and hence a periodic variation of the electron density. The Bragg position can be calculated using Bragg's Law

$$n\lambda = 2d \sin \Theta_n \quad n \in \mathbb{N}^+, \tag{3.18}$$

where d is the lattice spacing. Please note that the position of the Bragg peak in XRR might be slightly shifted compared to the one of crystal powder data due to effects like multiple scattering and other optical effects.

- **Laue oscillations** – The oscillations adjacent to the Bragg peak stem from interference effects of the out-of-plane lattice planes, therefore the periodicity can be used to estimate the out-of-plane coherently scattering crystal size.

Parratt's formalism (Section 3.1.2) and an appropriate assumption of a model can be used to fit XRR data. From the fit it is usually possible to extract the full electron density profile (or scattering length density (SLD)) of the sample along the out-of-plane direction as shown in Figure 3.3c). This might be useful to extract various film parameters and get a profound understanding of the film growth. As already mentioned above the absorption β in organic thin films is usually in the order of 10^{-9} and hence can be neglected for the calculation of the reflectivity of such films.

3.1.5 Roughness of Thin Films

Typical organic thin films are not perfectly flat but exhibit a certain roughness. In Section 3.1.3 it is already described how the roughness can be included for a multi-slap description of thin films. However, organic thin films can grow in an island-like growth (Section 2.2.1.2) for which the roughness which can be directly extracted from the fitting parameters of an XRR curve, is not sufficient. In this case the roughness of the film can be described by the root mean square roughness (σ_{rms}). The following considerations are mainly based on the work of Névot and Croce [122, 125, 126]. A schematic of a thin film surface including roughness is depicted in Figure 3.4a). z_f is the average height of the film and the height distribution can usually be described with a Gaussian of the following form

$$P_z = \frac{1}{\sqrt{2\pi}\sigma_{rms}} \exp\left(-\left(\frac{z - z_f}{\sqrt{2}\sigma_{rms}}\right)^2\right). \tag{3.19}$$

The SLD profile of an organic thin film can be fitted by the complementary Gaussian error-function ($erfc$) (Figure 3.4b)

$$\mathrm{SLD}(z) = a \cdot \mathrm{erfc}\left(\frac{z - z_f}{\sqrt{2}\sigma_{rms}}\right), \tag{3.20}$$

where a is a constant and $erfc$ is defined as follows

$$\mathrm{erfc}(x) = 1 - \mathrm{erf}(x) = \frac{2}{\sqrt{\pi}} \int_x^\infty \exp(-t^2)\,\mathrm{d}t. \tag{3.21}$$

From Equation (3.20) the final film thickness (z_f) and the nominal σ_{rms} can be directly extracted.

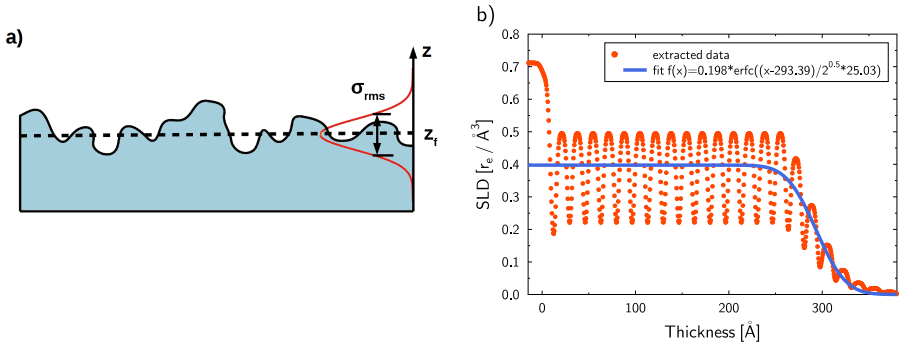

Figure 3.4: a) Schematic of an organic thin film including the average thickness z_f and the Gaussian-shaped roughness distribution with the full-width at half-maximum σ_{rms}. b) Example data of an electron density profile with a fitted erfc function for the extraction of the film parameters.

3.1.6 Rocking Scans

Rocking scans are used to probe the mosaicity of an organic sample. Figure 3.5 is a schematic representation of the mosaicity. On the left hand side the crystallite domains are perfectly aligned, and on the right hand side the domains are slightly misaligned with respect to each other. The latter can lead to grain boundaries in the thin film which might reduce the conductivity of the film.
Rocking scans are performed with a fixed absolute momentum transfer $|q|$, which is selected to correspond to a Bragg condition of the material and the sample is rocked under this condition. Usually, the intensity is plotted as a function of the rocking angle ω and the width of the rocking curve can be used as a gauge of the distribution of the crystal orientations [121].

3.1.7 Grazing Incidence X-Ray Diffraction - GIXD

Grazing incidence X-ray diffraction (GIXD) is a method used to characterize the in-plane structure. The geometry of such an experiment is shown in Figure 3.6. The X-rays impinge onto the sample in a shallow angle, usually slightly smaller than the critical angle. Since the measurements are performed below the critical angle the penetration depth is finite, however in most cases the complete organic

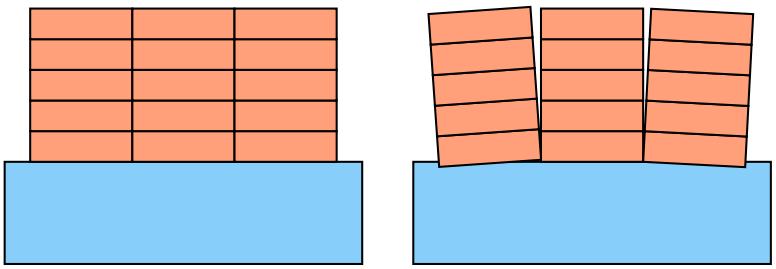

Figure 3.5: Schematic representation of mosaicity. On the left hand side all crystallite domains are perfectly aligned. On the other hand, on the right hand side the domains are slightly misaligned with respect to each other.

film is probed and the results are an average over the whole film. The out-of-plane detector angle is kept constant, equal to the incoming angle $\Theta_{in} = \Theta_{out}$ and the in-plane detector angle 2Φ is varied. The scattering angle has therefore a fixed out-of-plane component and the in-plane components can be calculated as follows:

$$q_x = \frac{2\pi}{\lambda} \left(\cos(\Theta_{out}) \cos(2\Phi) - \cos(\Theta_{in})\right), \tag{3.22}$$

$$q_y = \frac{2\pi}{\lambda} \left(\cos(\Theta_{out}) \sin(2\Phi)\right). \tag{3.23}$$

Since for most of the organic thin films the in-plane structure is isotropic (no preferred orientation of the in-plane crystallites) the GIXD data resembles the one of powder diffraction. The total in-plane momentum transfer can be expressed as follows:

$$q_{xy} = \sqrt{q_x^2 + q_y^2}. \tag{3.24}$$

For organic thin films usually Bragg peaks in the $q_{xy} = 0.7 - 3.0\,\text{Å}^{-1}$ range can be observed in the data. From the positions of these Bragg peaks the lateral crystal lattice spacings can be extracted and the width of the peaks are a measure for the in-plane coherently scattering crystal size (Section 3.1.8).

3.1.8 Scherrer's Formula

The analysis of the coherently scattering domain size of the films D_{hkl} can be performed by fitting the Bragg peaks with Gaussian functions followed by using Scherrer's formula [127, 128] in angular space

$$D_{hkl} = \frac{K\lambda}{B_{hkl} \cos\theta_{hkl}}, \tag{3.25}$$

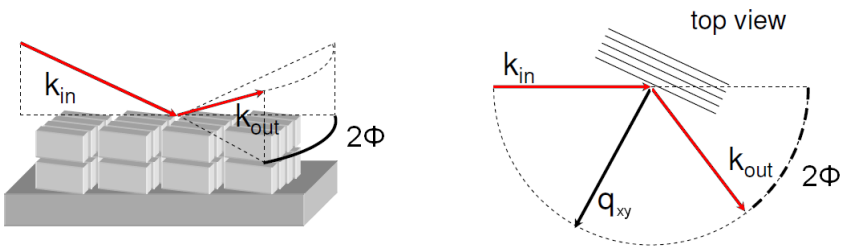

Figure 3.6: Scattering geometry of a grazing-incidence X-ray diffraction (GIXD) experiment, which can be used to probe the in-plane crystal structure. The image is taken from Ref. [23] and modified.

which can be simplified to the reciprocal space, using

$$\Delta q_{hkl} = \frac{4\pi}{\lambda} \cos\theta_{hkl} \frac{B_{hkl}}{2} \tag{3.26}$$

to

$$D_{hkl} = \frac{2\pi K}{\Delta q_{hkl}}. \tag{3.27}$$

Here K is Scherrer's constant, which is app. 0.94 for spherical like particles [129] and Δq_{hkl} is the broadening of the Bragg peak in reciprocal space [130]. This formula can be used to determine the out-of-plane as well as the in-plane coherently scattering domain size. Please note that the domains are likely to be not perfectly spherical, hence the K might not be perfectly accurate, but K is not very different for differently shaped domains and always in the order of unity. Furthermore, the broadening of the experimental setup is not taken into account, resulting in lower limits of D_{hkl}. In spite of that, the values of D_{hkl} presented within this work can be compared to each other and also the absolute values are sufficiently accurate to be compared to other values reported in literature.

3.1.9 Grazing Incidence Small Angle X-Ray Scattering - GISAXS

Grazing incidence small angle X-ray scattering (GISAXS) is a highly surface sensitive technique, usually used to probe the surface morphology. This method can be employed to characterized the film morphology after the growth as well as directly in real-time during the growth, by using a special vacuum chamber as described in Sec. 3.2. Here only a brief introduction is given to GISAXS and more information can be found in the literature [131–134].
The general scattering geometry is shown in Fig. 3.7. The X-ray beam impinges on the substrate under a grazing angle α_i and the scattering signal is recorded

for small angles around the origin of the reciprocal space, usually with an area detector. α_i is chosen close to the critical angle α_c so that an evanescent wave is created with a penetration depth which is usually limited to the sample, hence the information stemming from the substrate is suppressed. The information obtained close to the origin of the reciprocal space corresponds to relatively large length-scales in real-space, *i.e.* inter-island distances and island sizes on the surface.

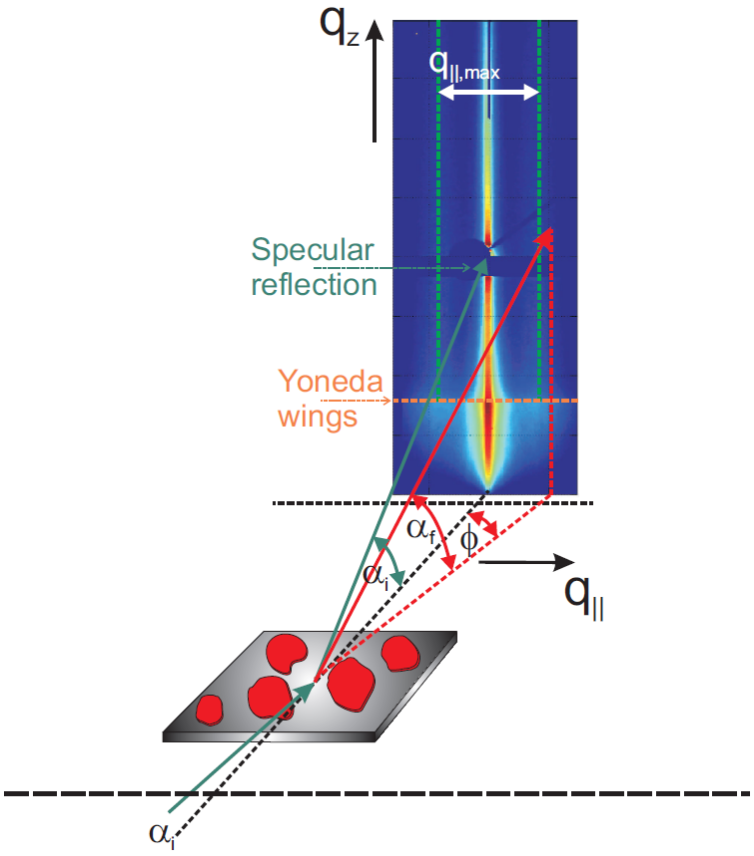

Figure 3.7: Scattering geometry for GISAXS experiments indicating the positions from which information are obtained. The image is taken from Ref. [135].

The different regions indicated in Fig. 3.7 have distinct reasons and comprise different information on the morphology of the sample.

- **Specular reflection:** Under specular conditions ($\alpha_i = \alpha_f$ and in-plane angle $\phi = 0$) the intensity of the signal is usually orders of magnitude higher than the diffuse signal from the surface, therefore usually this signal is blocked with a beamstop that the information in the diffuse region is not lost due to the limited dynamic intensity acceptance range of the area detector.

- **Yoneda wings:** This feature arises around the critical angle of the sample ($\alpha_f = \alpha_c$) and cannot be described purely by the first-order Born approximation. The maximum of the diffuse signal arises from the coherent superposition of multiple scattering events taken into account in the distorted wave Born approximation [136]. More details can be found in Ref. [131,132].

- **Specular rod:** Following the distorted wave born approximation, the intensity around the specular condition (finite α_f and $\phi = 0$) arises from a combination of the number of scatterers N and the mean form factor F at the origin. However, the intensity of the specular rod is altered by various additional effects, which lead to a loss of coherence, *e.g.* detector-acceptance, microscopic sample-curvature, energy- and angular-resolution. Due to these reasons, a description of this information is mostly very difficult [132].

- **Increased intensity at finite** q_{xy}: Please note that in Fig. 3.7 q_{xy} is denoted as $q_{\|}$. Centered around $q_{xy} = 0$ usually intensity maxima are observed which are extended in q_z direction. These peaks correspond to nearest-neighbour distances on the surface, *e.g.* average inter-island distances.

3.2 Vacuum Chamber for Film Preparation

Most of the films investigated for this thesis were prepared in a portable ultra-high vacuum (UHV) chamber depicted in Figure 3.8 and described in more detail in Ref. [137]. The chamber was pumped by a turbo molecular pump and an ion pump, resulting in a typical base pressure lower than 1×10^{-9} mbar. The substrate temperature can be controlled between app. 170 and 800 K by a combination of liquid nitrogen cooling and resistive heating. Usually, two home-build Knudsen cells were used for the evaporation of the molecules and the evaporation was monitored with a water-cooled quartz crystal microbalance (QCM). The beryllium window in the middle part of the chamber allowed the *in situ* and real-time investigation of the film growth using X-rays. The experiments were performed at the ID03 and ID10 beamlines (both at the European Synchrotron Radiation Facility (ESRF)) and at the MS-Surf-Diffraction beamline (Swiss Light Source (SLS)), respectively.

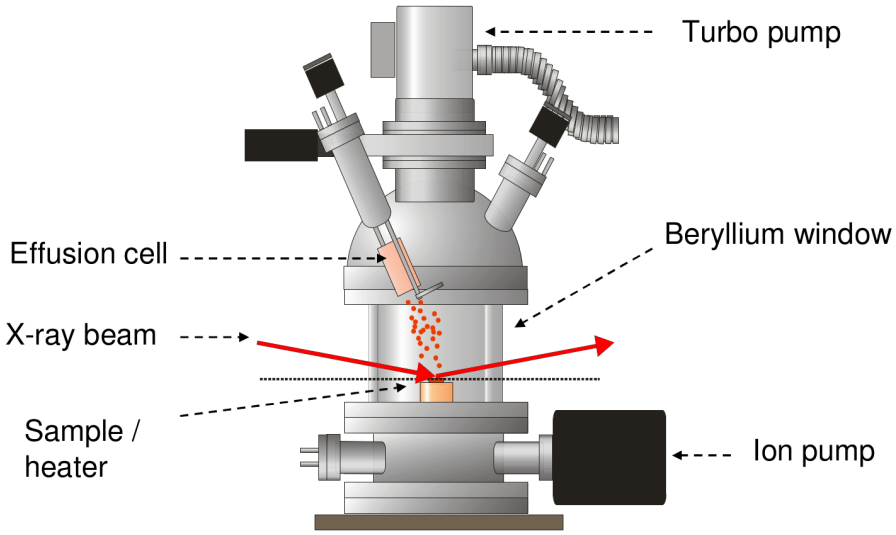

Figure 3.8: Portable UHV chamber for the thin film preparation, allowing the real-time and *in situ* investigation of the thin film growth. The image is taken from Ref. [23] and modified.

Chapter 4

Materials

For this thesis three different materials, all previously successfully used in organic photovoltaic cells, were investigated. First, α-sexithiophene (6T) is introduced. In Chapter 6 results of the pure 6T growth at different substrate temperatures are reported. In the second part buckminsterfullerene (C_{60}) is described, which was used in planar geometry bilayers together with 6T (Chapter 7) and in mixed films with 6T (Chapter 8) as well as in mixtures with diindenoperylene (DIP) (Chapter 9 and Chapter 10). DIP is described in the last part of this chapter. Within this thesis, the growth of DIP on top of 6T was investigated (Chapter 7) and it was used in mixtures together with C_{60} (Chapter 9 and Chapter 10).

4.1 α-Sexithiophene (6T)

Oligothiophenes are an important class of OSC materials. In particular, α-sexithiophene (6T) (chemical formula $C_{24}H_{14}S_6$) (Figure 4.1a) is considered very promising. It has shown a high open circuit voltage in combination with diindenoperylene in OPV cells [27] and high hole mobility of up to $4 \cdot 10^{-2}\,\mathrm{cm^2V^{-1}s^{-1}}$ in OFETs [138]. As in many other small molecule OSCs, the crystal structure as well as the crystal defect density are crucial for the performance of devices [29, 139, 140]. In this study we focus on the growth and structure of 6T on native silicon oxide (nSiO).
In general, depending on the substrate, the preparation conditions and the sample state (*i.e.* thin film or single crystal), there are several phases of 6T with different crystal structures reported [141–144]. The different lattice parameters are summarized in Table 4.1. In thin films on substrates with low interaction energies, mostly the so called low-temperature phase (LT-phase) of single crystals, reported by Horowitz *et al.* [143], and the thin film β-phase [141, 142] are found. The high temperature crystal phase is found in single crystals prepared by melt growth [144]. Figure 4.1a depicts the unit cell of the LT crystal phase, which includes four molecules.

For 6T on SiO_2 several studies of growth, structure, and charge transport

Phase	a [nm]	b [nm]	c [nm]	α [°]	β [°]	γ [°]
LT-phase [143]	4.4708	0.7851	0.6029	90.00	90.76	90.00
β-phase [141]	0.5667	0.7800	4.7288	90.00	100.6	90.00
HT-phase [144]	0.91404	0.56843	2.0672	90.00	97.78	90.00

Table 4.1: Lattice parameters of the different structures of 6T.

report that 6T molecules are oriented mostly in a way where the long molecular axis is almost perpendicular to the substrate [82, 141, 142, 145–148]. Different anisotropic growth scenarios on fused silica and stretched polyethylene substrates were measured via absorption spectroscopy by Oelkrug *et al.* [149]. On TiO_2 the formation of domains of the LT-phase [143] was observed [150, 151]. Highly ordered pyrolytic graphite (HOPG), mica and KCl have also been used as substrates for the growth of 6T [152–156]. The adsorption of 6T on single crystal Cu surfaces was studied by scanning tunneling microscopy, X-ray photoelectron spectroscopy, and near-edge X-ray absorption fine structure [157] as well as X-ray diffraction [158] revealing mainly lying-down 6T domains following closely the substrate lattice. On metal single crystal substrates the molecular orientations and adsorption structures of 6T have also been studied [159–162]. Furthermore, 6T was used as a templating layer for the growth of *p*-sexiphenyl and vice versa, leading in both cases to an epitaxial relationship between the two organic compounds [88–90].

Films prepared on thermally oxidized silicon wafers (SiO_x) are particularly interesting for applications like OFETs and also for hybrid inorganic-organic devices. For relatively thick 6T films (100 nm) deposited on thermally oxidized silicon wafers it has been reported that 6T arranges in different phases for various substrate temperatures at moderate deposition rates (6-30 nm/min) [142]. It has also been demonstrated that the deposition rate has a huge impact on the resulting crystal phase [82]. For relatively low deposition rates, the molecules adopt a thermodynamically favorable packing (LT-phase), whereas at higher rates (about 36-48 nm/min) the films crystallize predominantly in a phase similar to a frozen smectic state (β-phase) [82].
6T used in this thesis was purchased from Sigma-Aldrich and purified twice by temperature gradient sublimation prior to use.

4.2 Buckminsterfullerene (C_{60})

Buckminsterfullerene (C_{60}) is a sphere-like all carbon molecule, already theoretically predicted in 1970 [163,164] and first synthesized in 1985 [165]. Since then C_{60} itself and various derivatives were employed in numerous applications [166, 167].

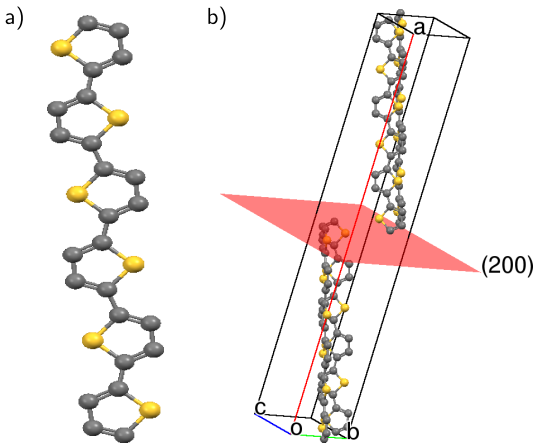

Figure 4.1: a) Structure formula of a single α-6T molecule. b) The crystal unit cell of the LT-phase [143] together with the (200) plane, responsible for the main reflections in the standing-up configuration of the molecules. o corresponds to the origin of the unit cell and a, b, c indicate the directions of unit cell vectors. The lattice parameters of the depicted crystal structure are $a = 44.708(6)$ Å, $b = 7.851(3)$ Å, $c = 6.029(2)$ Å, $\alpha = 90°$, $\beta = 90.76(2)°$ and $\gamma = 90°$ [143]. Image taken from [83].

In OPV cells C_{60} and its derivatives are commonly used as electron acceptors due to their high electron affinity [168] and to its reasonable absorption overlap with the solar spectrum [169]. C_{60} can form crystallites in either a face centered cubic (fcc) or hexagonal closed packed (hcp) structure [170, 171] or, at low temperatures ($T \leq 249\,\mathrm{K}$) simple cubic (sc) structure [172]. In the latter case, the single C_{60} molecules are locked in an orientation where the electron-rich short inter-pentagon bonds face the electron-poor pentagon centres of the neighbouring molecule [173], whereas the van-der-Waals bond molecules can rotate freely around their center of mass, at higher temperatures [174]. The crystal lattice parameters are summarized in Table 4.2. In thin films on only weakly interacting substrates, like nSiO or indium tin oxide (ITO), C_{60} tends to form polycrystalline films with randomly oriented crystallites with no preferred out-of-plane order [175, 176].

Phase	a [nm]	b [nm]	c [nm]	α [°]	β [°]	γ [°]
fcc [171]	1.4156	1.4156	1.4156	90.00	90.00	90.00
hcp [171]	1.0009	1.0009	1.6338	120.00	90.00	90.00
sc [172]	1.404	1.404	1.404	90.00	90.00	90.00

Table 4.2: Lattice parameters of the different structures of C_{60}.

C_{60} used for this thesis was purchased from Creaphys with a purity of 99.9 %.

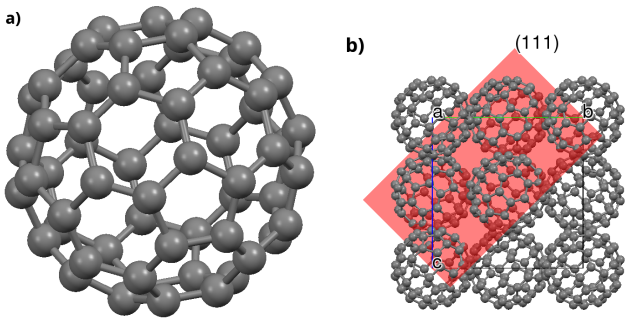

Figure 4.2: a) Structure formula of a single C_{60} molecule. b) The crystal packing of the C_{60} fcc structure with the (1 1 1) plane, from which scattering in thin films is often observed.

4.3 Diindenoperylene (DIP)

Diinendoperylene (DIP) is a red dye with the chemical structure $C_{32}H_{16}$. Figure 4.3a depicts the structure of this planar perylene derivate, also known as Periflanthene, with the two indenogroups attached at the ends of the long perylene axis. For DIP single crystals, two different crystal phases are reported. On the one hand, in the low-temperature (LT) triclinic phase the unit cell contains four molecules where two molecules are conformationally different. On the other hand, in the high-temperature (HT) monoclinic phase the unit cell contains two almost planar molecules [29,177]. In both cases the molecules form a herringbone structure. In thin films on nSiO, DIP is usually found in a thin film phase which is very similar to the HT phase [178]. The crystal lattice parameters of the three different phases are summarized in Table 4.3. In thin-film growth on nSiO, at

Phase	a [nm]	b [nm]	c [nm]	α [°]	β [°]	γ [°]
LT-phase [177]	1.166	1.301	1.497	98.44	98.02	114.55
HT-phase [177]	0.717	0.855	1.680	90.00	92.42	90.00
Thin film phase [178]	0.709	0.867	1.690	90.00	92.2	90.00

Table 4.3: Lattice parameters of the different structures of DIP.

substrate temperatures between 300 and 400 K, DIP arranges usually with almost upright standing-up molecules, *i.e.* *ab*-plane of the unit cell parallel to the substrate surface (so-called σ-orientation) [76, 178], whereas, at lower substrate temperatures DIP molecules tend to orient in a lying-down orientation (so called λ-orientation) [179]. For a substrate temperature of $\sim$ 400 K DIP grows in an almost perfect layer-by-layer mode for the first few monolayers and afterwards shows an unusual rapid roughening of the film-growth [79].
DIP used in this thesis was purchased from 3. Physikalische Institut, University

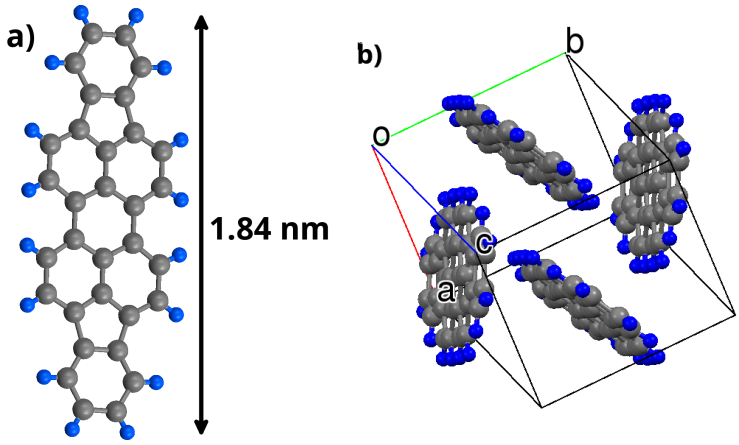

Figure 4.3: a) Structure formula of a single DIP molecule. b) The crystal unit cell of the HT-phase [177].

of Stuttgart or PAH Forschung Greifenberg (Germany), and purified twice by temperature gradient sublimation prior to use.

Part II

Results

Chapter 5

Overview

In this part the results and conclusions obtained by our experiments are presented. Different aspects and scenarios of organic thin film growth were investigated in this project.
First, the growth of pure 6T was investigated in detail (Chapter 6). Real-time GIXD experiments have shown that two different crystal phases (low-temperature crystal phase (LT) and β-phase) are competing in the crystal growth of 6T under the preparation conditions employed here. Different substrate temperatures promote the growth of one or the other crystal phase. However, close to the substrate the β-phase is dominant, independent from the substrate temperature.
Second, the influence of a bottom layer of 6T on the growth of C_{60} and DIP was examined, representing the PHJ geometry commonly used in small molecule OPV cells (Chapter 7). A strong templating effect of the 6T is observed leading to a size correlation of the in-plane coherently scattering domains of the overlayer to the 6T.
In the third part, mixtures of 6T and C_{60} are evaluated (Chapter 8). This kind of mixture corresponds to the BHJ geometry in OPV cells. Different mixing ratios and different substrate temperatures were used to modify the growth and mixing scenario showing a strong influence of the C_{60} on the growth of 6T. Furthermore, annealing experiments on pure 6T and the mixtures were performed showing that the film quality, *i.e.* the crystallinity and phase-purity, can be strongly improved by a post-growth annealing process on pure 6T films, whereas a similar annealing performed for the mixture has no influence at all.
Moreover, mixtures of DIP and C_{60} were studied (Chapter 9). There, different preparation strategies, *i.e.* variation of the substrate temperature or deposition rate, systematic interruption of the growth process and the introduction of surface modification layers, were used to tailor the length scale of phase separation in equimolar DIP:C_{60} mixtures.
Non-equimolar mixtures of DIP and C_{60} were also investigated and the results are presented in Chapter 10 showing that mixtures with an excess of DIP grow similar to films of pure DIP films. Nevertheless, these mixtures do not show a

rapid-roughening, as seen for pure DIP [79], but rather an almost perfect layer-by-layer growth. On the other hand, equimolar and C_{60} dominated mixtures show a growth behavior which is more similar to the growth of pure C_{60}.

Chapter 6

Results of Thin Film Growth of α-Sexithiophene

The results presented in this chapter are published in Ref. [83][1].

6.1 Introduction

For the understanding of the growth of thin films in a planar geometries (material A on B) or in a mixture (material A and B deposited at the same time), the understanding of the single component film is crucial. Here, the growth scenario of α-sexithiophene (6T) (Sec. 4.1) at different substrate temperatures was studied using real-time and postgrowth X-ray scattering techniques. We used different substrate temperatures to prepare thin films comprising the β-phase and the LT-phase. Our time-resolved (and hence film thickness dependent) measurements provide important insights into the evolution and competition of the different crystalline phases of 6T and their dependence on the preparation conditions. Since the growth of organic thin films is in general not in equilibrium, it is imperative to employ real-time measurements to investigate the growth kinetics [78, 180–182]. The real-time investigations are necessary to observe possible effects of transient crystal phases. Furthermore, we can follow the evolution and competition of different structural features which is not possible post-growth.

6.2 Experimental

The substrate temperature during growth was 233 K, 308 K or 373 K and all films were aimed at a nominal film thickness of 20 nm. The used deposition rate varied

[1] C. Lorch, R. Banerjee, C. Frank, J. Dieterle, A. Hinderhofer, A. Gerlach, and F. Schreiber, J. Phys. Chem. C **119**, 819 (2015): *Growth of Competing Crystal Phases of α-Sexithiophene Studied by Real-Time X-ray Scattering.*

between 0.13 and 0.16 nm/min. The experiments were performed at the MS-X04SA/Surface Diffraction beamline at the Swiss Light Source (SLS) [183] using an energy of 12.4 keV (corresponding to a wavelength of 0.999 Å) and a PILATUS II area detector. Slits placed directly in front of the detector were used to mimic a point detector for the real-time and post-growth scans.

6.3 Results

6.3.1 X-Ray Reflectivity

XRR is used to obtain information about the film structure in a direction perpendicular to the surface of the film [120]. Figure 6.1 depicts the measured XRR data of the different samples. For all the films the Kiessig oscillations in the low q_z range beyond the total reflection edge are not very pronounced. This is a strong indication that the top surfaces of the films are relatively rough.
In the plot, corresponding to the sample prepared at 373 K, Bragg peaks up to an out-of-plane momentum transfer $q_z \approx 1.4\,\text{Å}^{-1}$ are visible. This is an indicator that this sample exhibits a high out-of-plane crystalline order. The Bragg peaks marked with vertical black solid lines are due to reflections from crystallites with a lattice spacing of $d = 44.73\,\text{Å}$. These crystallites can be identified as the almost upright standing molecules in the LT-phase ($d = 44.708\,\text{Å}$) [143]. The fringes around the Bragg reflections ("Laue oscillations") correspond to the coherent out-of-plane crystallite size ($D_{coh\perp}$), calculated from the periodicity of the oscillations (Δq_z) by $D_{coh\perp} = 2\pi/\Delta q_z$. For the LT-phase crystallites in the 373 K film one obtains $D_{coh\perp} = 23 \pm 3$ nm. Comparing this to the nominal film thickness of 20 nm leads to the conjecture that crystallites are formed with a size similar to the total film thickness, in a continuous columnar growth from the substrate to the top of the film. Weak Bragg reflections are observed at $q_z = 0.248\,\text{Å}^{-1}$ and $0.513\,\text{Å}^{-1}$ for the sample prepared at 373 K. These reflections correspond to crystallites of the β-phase.
In the XRR data of the film prepared at 308 K (black line in Figure 6.1) the Bragg reflections of the standing LT-phase are weak with no Laue oscillations, implying that the out-of-plane coherent crystallite size of the LT-phase is rather small. However, Bragg reflections of the β-phase are observed very close to the q_z values expected from the literature [82, 142]. The fringes close to the (200) Bragg reflection of the β-phase correspond to an out-of-plane coherent crystalline size of $D_{coh\perp} = 17 \pm 2$ nm.
For the film prepared at 233 K no peaks having their origin in the standing-up phase of the LT-phase are observed. The first and second order of the β-phase (h00) reflections are seen at $q_z = 0.256\,\text{Å}^{-1}$ and $q_z = 0.513\,\text{Å}^{-1}$, respectively. Presumably, the out-of-plane coherent length of the crystallites causing these reflections is rather small, and therefore no Laue oscillations are observable.

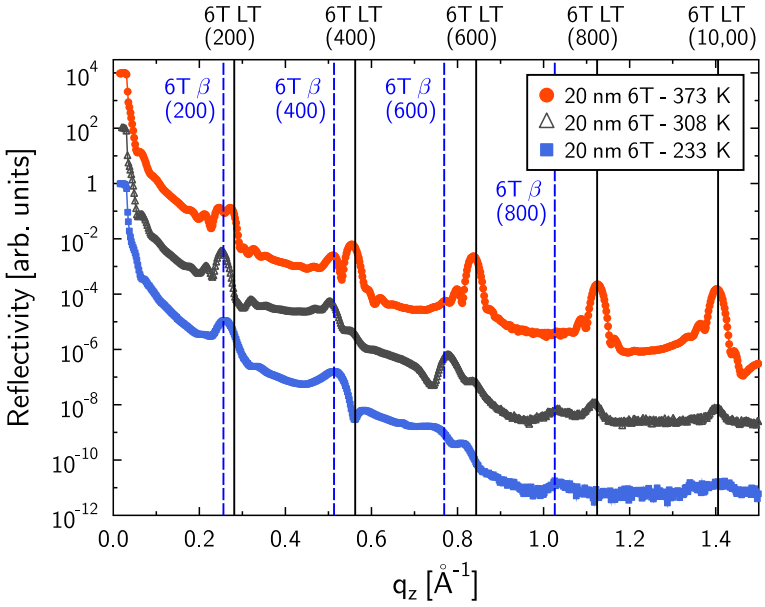

Figure 6.1: XRR measurements of 6T grown at different substrate temperatures. For 373 K (red solid dots) one can identify several orders of the Bragg reflections corresponding to the 6T LT bulk crystalline phase (positions marked with black vertical lines). In the films prepared at 308 K (black triangles) and 233 K (blue squares) the observed Bragg peaks can be mainly allocated to the β-phase (Bragg positions corresponding to domains of upright standing molecules are marked with blue dashed lines).

The XRR data were fitted with the Parratt formalism [123] using the GenX-software [184]. Since the texture of the films consists of various crystalline phases, a model was used where the entire film is described by only one box having a certain thickness, surface roughness, and electron density. The data were fitted in the range $q_z = 0 - 0.171\,\text{Å}^{-1}$ in order to extract the film thickness and the roughness of the films (Figure 6.2a). These are given in Table 6.1. Comparing the resulting film thickness d with the roughness σ one can see that for the film prepared at 233 K the ratio $d/\sigma = 4.3$ of film thickness to roughness is significantly smaller compared to 308 K and 373 K ($d/\sigma = 6.0$ and $d/\sigma = 6.2$, respectively). For amorphously growing organic compounds one would expect a higher roughness for high temperature films [185] and usually the crystallinity of thin organic films improves with increasing substrate temperature [86,186]. That this correlation is not observed here can be attributed to the fact that at different substrate temperatures, the dominant crystalline phase varies between the LT-phase and the β-phase or a mixture of both phases of 6T.
Figure 6.2b shows the extracted electron densities for the different samples (Table 6.1). The fitted values ($0.38\,\text{Å}^{-3}$, $0.45\,\text{Å}^{-3}$ and $0.46\,\text{Å}^{-3}$ for 373 K, 308 K and 233 K, respectively) are all lower than the values obtained by calculations using the unit cell volume ($0.48\,1/\text{Å}^3$ and $0.46\,1/\text{Å}^3$, for the LT-phase and the β-phase,

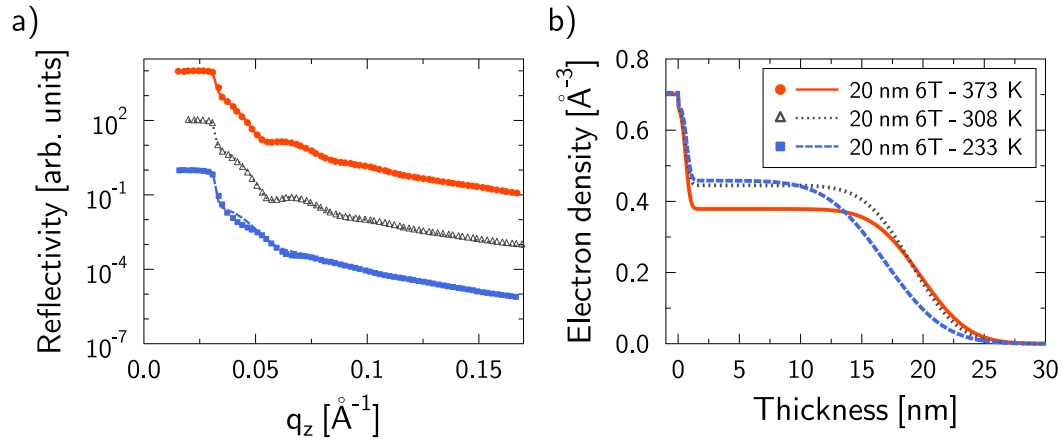

Figure 6.2: a) Experimental XRR data (symbols) and the simulated values using a one-box-model (lines) up to $q_z = 0.171\,\text{Å}^{-1}$ for three growth temperatures are shown. b) Corresponding electron density profiles extracted from the fits.

respectively). This leads to the assumption that the thin films do not form perfectly filled layers, meaning that the packing fraction is below one. Furthermore, the electron density increases for lower substrate temperatures, showing that also the substrate temperature influences the packing fraction.

Table 6.1: Summary of the films deposited at different temperature with thickness d, roughness σ, the thickness-to-roughness ratio d/σ, and electron densities ρ_e (at a thickness of 5 nm) extracted from the electron density profiles from the XRR fits. The coherent out-of-plane crystallite size $D_{coh\perp}$ values are calculated from Laue oscillations.

Substrate Temperature	Thickness d [nm]	Roughness σ [nm]	d/σ	Electron density ρ_e [Å^{-3}]	$D_{coh\perp}$ [nm]
373 K	19.2 ± 0.2	3.1 ± 0.2	6.2 ± 0.4	0.38 ± 0.02	23.1 ± 3.1
308 K	18.5 ± 0.4	3.1 ± 0.1	6.0 ± 0.5	0.45 ± 0.02	17.4 ± 2.3
233 K	16.2 ± 0.9	3.8 ± 0.3	4.3 ± 1.2	0.46 ± 0.02	-

6.3.2 Grazing Incidence Diffraction

The in-plane crystalline structure of the samples was investigated via GIXD measurements [120]. The GIXD data of the films prepared are shown in Figure 6.3. For the film with a substrate temperature of 373 K, the peaks corresponding to the standing-up 6T LT-phase are prominent. The peak at $q_{xy} = 1.38\,\text{Å}^{-1}$ can be associated with the β-phase [82]. For the sample prepared at 308 K all peaks can be associated with standing-up 6T molecules corresponding to the β-phase

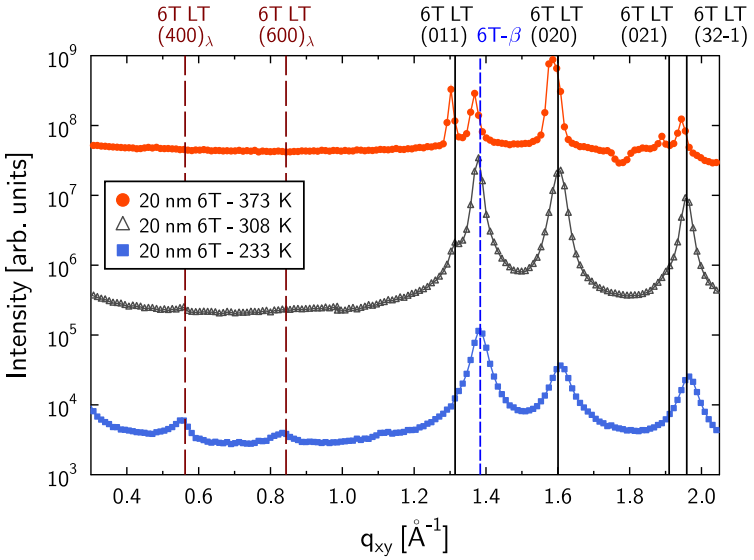

Figure 6.3: GIXD measurements of 6T grown at different substrate temperatures at an incident angle of $\alpha_{in} = 0.13°$. For the films prepared at 233 K (blue squares) and 308 K (black triangles) the peak corresponding to the β-phase is the dominant one (marked with a blue dashed line). At 233 K weak reflections from lying crystal domains are observed (vertical brown dashed lines and marked with λ). For the film prepared at 373 K the LT-phase Bragg peaks are dominant.

or the LT-phase with similar intensities.
In the data of the film prepared at 233 K the β-phase peak is again the one with the highest intensity. The (011) LT peak is not observed. Furthermore, the intensities of the (020) and (021) LT peaks are weaker than the corresponding ones in the other films. Additionally, small peaks at lower q_{xy} values ($q_{xy} = 0.55\,\text{Å}^{-1}$ and $0.82\,\text{Å}^{-1}$) are detected. These peaks correspond to domains of lying 6T molecules (LT-phase) with a small coherent size. On comparison of the films at the three different temperatures, a slight shift of almost all peaks toward lower q_{xy} values with increasing temperature is observed. This shift corresponds to a change in the in-plane lattice parameter by approximately 1%. This can be attributed to a small change in the orientation, *e.g.* a slightly different tilt angle, of the molecules, due to different diffusion energies of the molecules at different substrate temperatures, or due to different interaction potentials of the surrounding molecules, oriented in different crystal phases. However, using the given experimental setup and resolution it is not possible to quantitatively estimate any systematic variation.
The observed peaks of the films were fitted and the Scherrer formula [127] $D_{coh||} = 2\pi K/fwhm$ was used to calculate the in-plane coherent crystallite size ($D_{coh||}$). Here, $K = 0.94$ is Scherrer's constant for spherically shaped grains and $fwhm$ is the full width at half-maximum of the fitted peaks. Since no in-

strumental line-broadening was taken into account, the reported values are only lower limits but all are well below the resolution limit of the in-plane experiments $\Delta D_{coh||} \approx 100\,\text{nm}$. $D_{coh||}$ values for all samples are summarized in Table 6.2.

Table 6.2: Summary of the in-plane coherent crystallite sizes of different 6T films.

Substrate Temperature	Lower limit of coherent crystallite size $D_{coh\|\|}$ [nm]			
	LT-phase (011)	(020)	(32-1)	β-phase
373 K	50.1	20.1	29.8	30.7
308 K	21.7	17.0	22.0	26.1
233 K	-	11.0	11.5	15.3

There is a significant difference in the in-plane coherent crystallite sizes between the films prepared at 233 K and 373 K. $D_{coh||}$ of the LT-phase domains increases from 11.0 nm to 20.1 nm and from 11.5 nm to 29.8 nm for the (020) and (32-1) peak, respectively. For the β-phase domains an increase from 15.3 nm to 30.7 nm is observed. Hence, this increase by a factor of approximately two is independent of the crystal phase and seems to depend merely on the change in the preparation conditions (here the substrate temperature).

Figure 6.4 depicts 2D reciprocal space maps of the three different films in a q_{xy} range of $1.2 - 1.7\text{Å}^{-1}$. One can clearly recognize the Bragg reflections related to the β-phase and the (020) peak of the LT crystal phase. The peak corresponding to the β-phase is very broad in q_z direction, indicating a small out-of-plane coherent crystallite size.

6.3.3 Real-Time Grazing Incidence Diffraction

During the growth of the samples prepared at 308 K and 373 K real-time GIXD scans, monitoring the evolution of the β peak ($q_{xy} = 1.38\,\text{Å}^{-1}$) and of the (020) LT-phase peak ($q_{xy} = 1.60\,\text{Å}^{-1}$), were performed [20, 22, 96, 106]. With these measurements we are able to follow and understand the competition between different crystal phases. This is necessary since conventional GIXD measurements mostly probe the structure of the entire organic film (apart from penetration depth effects) and hence do not provide time-resolved information. The peaks were fitted using pseudo-Voigt functions. The shape of the peaks (*i.e.* the full-width half maximum and the mixing coefficient for the pseudo-Voigt function) did not vary significantly during the film growth. Hence, $D_{coh||}$ does

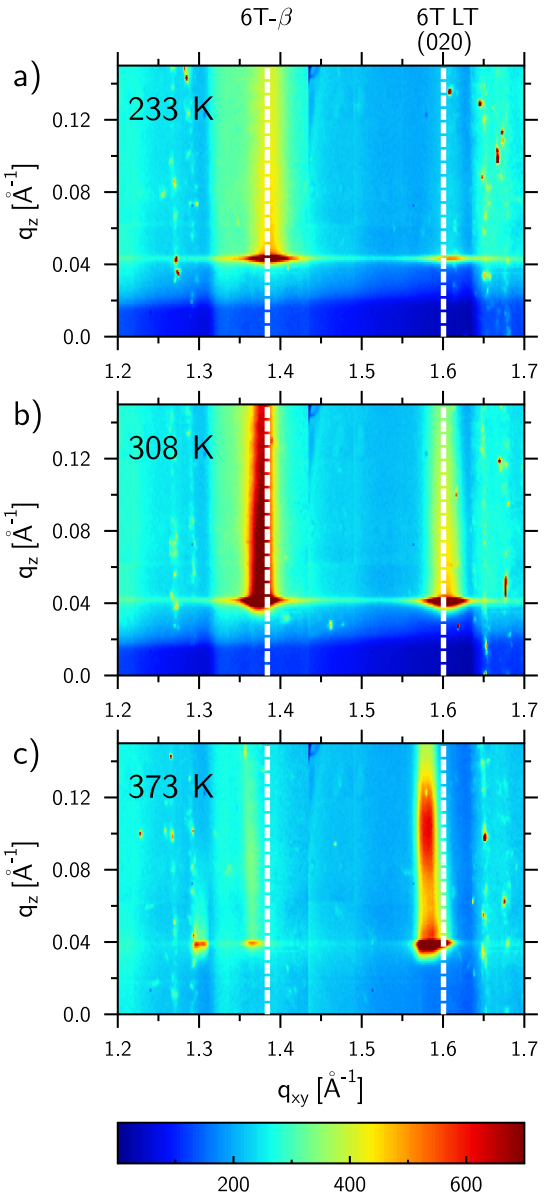

Figure 6.4: 2D reciprocal space maps at a) 233 K b) 308 and c) 373 K. The images are a combination of two pictures (first one covers a q_{xy} range of $1.2 - 1.44\,\text{Å}^{-1}$ and the second one covers a q_{xy} range of $1.44 - 1.7\,\text{Å}^{-1}$) and were taken at an incident angle of $\alpha_{in} = 0.13°$. The white dashed lines mark the positions of the reflections arising from the β-phase ($q_{xy} = 1.38\,\text{Å}^{-1}$) and the LT-phase ($q_{xy} = 1.60\,\text{Å}^{-1}$), respectively. In the films prepared at 233 K and 308 K, the reflection corresponding to the β-phase is broadened and extended in q_z indicating a relatively small out-of-plane coherent crystallite size.

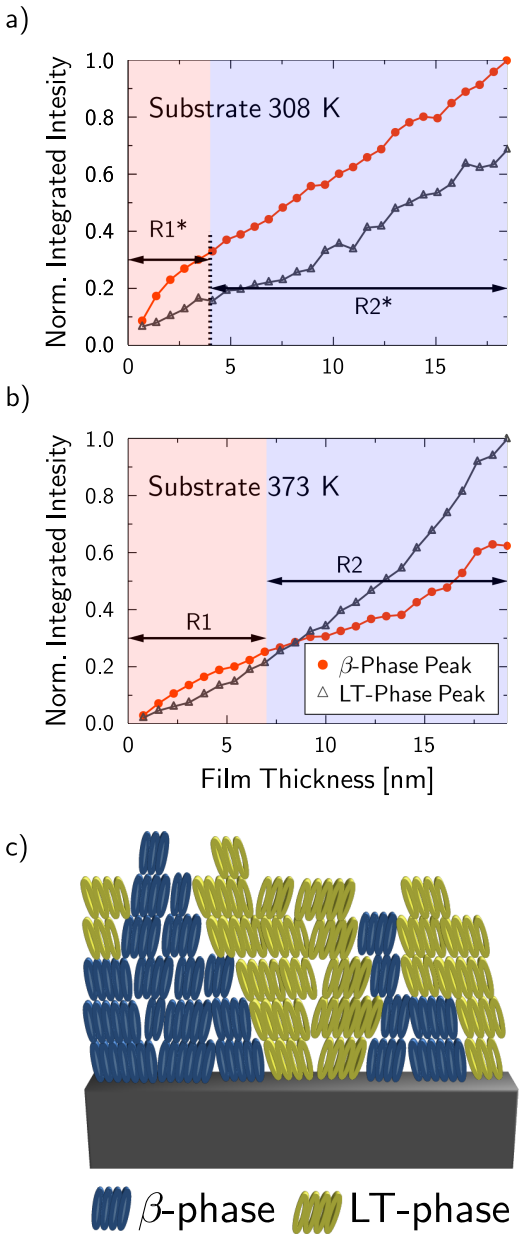

Figure 6.5: Peak intensity evolution of the β-phase ($q_{xy} = 1.38\,\text{Å}^{-1}$) and LT-phase ($q_{xy} = 1.60\,\text{Å}^{-1}$) during growth of 6T films prepared at a) 308 K and b) 373 K substrate temperature, respectively. For 373 K the β-phase dominates for the first 8 nm. Above this thickness the LT-phase is the dominating crystal phase. However, for 308 K the β-phase is predominant during the entire film growth. c) Sketch of the film growth behavior at 373 K. At the beginning the β-phase is dominant, but above a certain thickness the LT-phase grows predominantly at the expense of the β-phase.

not significantly increase during the growth under the conditions employed. However, the amount of material forming the specific domains increases as the growth progresses. Figure 6.5 depicts the evolution of the peak intensity (the area under the fitted curves) of the β-phase and of the LT-phase peak vs. the film thickness. The signals were normalized to the value of the highest peak at the end of the growth. We note that the x-axes show slightly different ranges due to different film thicknesses extracted from the fitted XRR data. For the sample prepared at 308 K the formation of domains belonging to the β-phase is faster than the one of domains of the LT-phase up to a film thickness of approximately 4 nm (region marked with R1* in Figure 6.5a). Beyond this thickness (region R2*) the intensities of both phases grow simultaneously and linearly with film thickness, with the β-phase being slightly faster than the LT-phase.
For the sample grown at a substrate temperature of 373 K (Figure 6.5b) the growth of β-phase domains is faster than the one of LT-phase domains only for low film thicknesses up to 7 nm (region R1). Furthermore, the intensity of the peak corresponding to the LT-phase increases non-linearly in region R1. In the thickness range from 7 to 19.2 nm (region R2) the intensity increase of the β-phase is significantly slower than for the LT-phase. The peak intensity of the LT-phase seems to accelerate over the whole film thickness. At approximately 8 nm this intensity overtakes the one of the β-phase.

6.4 Discussion

The observations of the film growth previously presented, indicate that close to the substrate, *i.e.* in the first 2 to 3 monolayers, 6T seems to arrange preferably in the β-phase. With increasing substrate temperature (from 303 K to 373 K) the thermal energy of the molecules is enhanced. Therefore, it is more likely for the molecules to arrange in a thermodynamically favorable configuration. This results in the formation of larger crystal domains of the LT-phase. However, still some β-domains are formed at a substrate temperature of 373 K, presumably due to a templating effect of the β-domains formed in the first few monolayers. This is schematically indicated in Figure 6.5c.
After approximately 7 nm the film growth seems to be mostly decoupled from the substrate interaction. Above this thickness the diffusion of the molecules is dominated by the inter-molecular interaction.
Overall, the results appear to be a rather typical case of competition of phases similar in energy in small molecule OSCs. However, due to the subtleties in the energy landscape, each system has to be studied individually. Nevertheless, for different organic semiconductors similar effects have been reported. For instance, pentacene exhibits two different phases in thin film growth, depending *inter alia* on the substrate temperature [187], similar to the results reported in this paper.

A substrate induced layer is mainly formed up to a critical thickness, and above this the film predominately grows in the bulk crystal phase [188]. For diindenoperylene, a low substrate temperatures can lead to the formation of lying domains (λ-orientation) which are energetically unfavorable, but kinetically favored, since for an orientation in the standing phase (σ-orientation), which decreases the total surface energy, an energy barrier for the formation of a σ-nucleus needs to be overcome. At higher substrate temperatures this energy barrier might be overcome [78,179]. We find a similar behavior for 6T (Figure 6.3) indicating that this might be a general effect for rod-like oligomers [38, 189]. These different phases affect strongly the usually anisotropic optical properties in OSCs [139, 190]. Also, the electrical transport is affected, in particular by phase boundaries [191].

6.5 Conclusion

In conclusion, we used X-ray scattering experiments to identify and study the competing interactions of different crystal phases in the thin film growth of α-sexithiophene. We found that the substrate temperature has an important influence on the formation of the different phases. By comparing our findings with the results reported by Moser *et al.* [82], we find that the effect of decreasing the substrate temperature is similar to increasing the rate of deposition of the molecule and one obtains at least qualitatively similar films. Increasing the substrate temperature from 233 K to 373 K leads also to an increase of the in-plane coherent crystallite size by a factor of two, for both crystal phases. From real-time GIXD data we deduce that the β-phase is induced by the substrate and only prominent during the early phase of growth. For the film grown at a substrate temperature of 373 K, we find a critical thickness of approximately 8 nm beyond which the LT-phase dominates the growth of the film. We conclude that the initial phase of the growth is dominated by the influence of the substrate and after a certain temperature-dependent thickness the growth is more or less decoupled from the substrate and dominated by temperature effects. Still templating effects of the initial crystal-phase are relevant and lead to the formation of further β-phase domains.

Chapter 7

Templating Effects of α-Sexithiophene on C_{60} and Diindenoperylene

The results presented in this chapter are published in Ref. [192][1].

7.1 Introduction

The material combination of α-sexithiophene (6T) (Fig. 7.1 left) and C_{60} buckminster fullerene (Fig. 7.1 middle) is an interesting donor-acceptor pair for OPV cells [24, 27]. Interestingly, for this material combination, as well as for the combination of 6T and diindenoperylene (DIP) as donor-acceptor pair, a dependence of the open circuit voltage on the relative orientation and structure of the molecules, together with surface morphologies of similar organic blends have been reported [28]. For BHJs of 6T and C_{60} or C_{70}, post-preparation treatments, such as annealing were used to improve the solar cell parameters but no changes in the structure are reported [25, 193]. Furthermore, the 6T in combination with C_{60} was used as one of the first ambipolar OFETs [194]. The growth of C_{60} on 1 or 2 monolayers of 6T prepared in a lying-down orientation, follows a self-organised mechanism in stable chains and chain arrays [91–93, 195]. For the same configuration on Ag substrates, a charge transfer from the substrate directly to the C_{60} through the neutral 6T has been reported [196, 197].
For 6T OPV cells using the PHJ geometry, an extraordinarily high open circuit voltage, utilizing DIP (Fig. 7.1 right) as electron acceptor material, is reported [27]. In contrast to the sphere-like C_{60}, the perylene derivate DIP is rod-like and hence sterically more compatible to 6T. DIP itself has shown interesting

[1] C. Lorch, R. Banerjee, J. Dieterle, A. Hinderhofer, A. Gerlach, J. Drnec, and F. Schreiber, J. Phys. Chem. C, **119**, 23211 (2015): *Templating Effects of α-Sexithiophene in Donor-Acceptor Organic Thin Films.*

effects as a templating layer, *i.e.* improving the crystal structure of C_{60} deposited on top [176], or leading to a void-filling growth scenario of perfluropentacene (PFP) on DIP [96] and exhibiting also a strong templating effect on PFP [198].

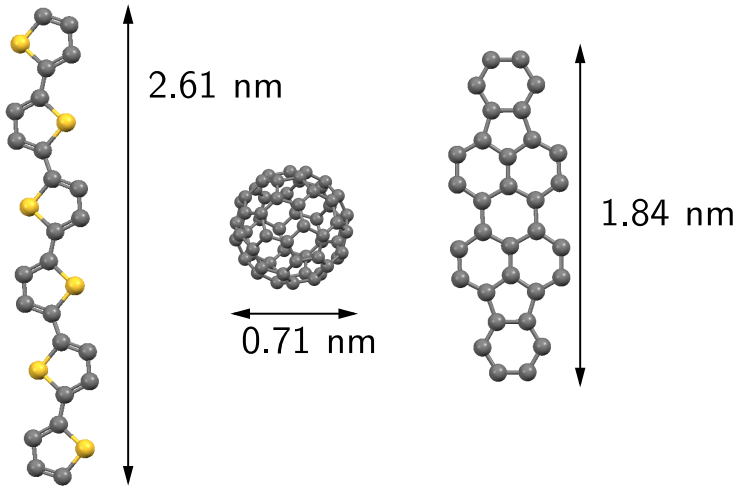

Figure 7.1: Schematics of the different molecules used in this study. 6T ($C_{24}H_{14}S_6$) on the left (size from Ref. [143]). In the center C_{60} (size from Refs. [199,200]) and on the right DIP ($C_{32}H_{16}$) (size from Ref. [186])

.

For both OPVs and OFETs the crystalline structure of the films is highly relevant for the efficiency of the device. As shown for other material combinations the impact of the bottom (organic) material has a huge influence on the film formation process of the material deposited on top [86, 96, 176, 198]. *In situ* X-ray diffraction experiments provide an ideal tool to investigate the thin film structure. Since the experiments are performed under ultra-high-vacuum (UHV) conditions, effects from exposure to ambient conditions, possibly changing the film structure, can be precluded. Additionally, real-time experiments allow us to follow the dynamics of structure formation and the investigation of transient effects [78, 135, 180, 201].

In this study we focus on the correlation of the growth conditions to the overall structure of the PHJ. We prepared different layers of 6T on nSiO, in order to investigate the influence of these templating layers on the growth behavior of C_{60} and DIP. For the preparation of the 6T films different substrate temperatures and film thicknesses were used, whereas for the growth of C_{60} only the substrate temperature, and hence the kinetics of the growth, was varied. Similarly, the growth of DIP was studied for different substrate temperatures during the evaporation of the materials.

For both acceptor materials, C_{60} as well as DIP, when deposited on top of 6T, we observe a strong correlation between the coherently scattering in-plane island size between the templating 6T layer and the top material. Furthermore, the

C_{60} crystal structure improves drastically when deposited on top of 6T compared with nSiO, showing the importance of the surface interaction on the growth of molecular small compounds. In addition, the deposition of the top material alters the structure of the templating 6T layer, indicating that post-growth treatment can impact the film structure.

7.2 Experimental

6T was purchased from Sigma Aldrich and purified twice by temperature gradient sublimation before usage. C_{60} was purchased from Creaphys and used without further purification. DIP was received from PAH Forschung Greifenberg (Germany). The samples were prepared and measured in a portable UHV chamber [137]. Before the installation the silicon substrates with a native oxide layer (nSiO) of approximately 1.8 nm were cleaned in an ultrasonic bath with acetone, isopropanol and purified water. Before each sample preparation the substrates were heated up to approximately 770 K to remove the old film. The base pressure of the system was below 10^{-9} mbar, increasing to approximately 3×10^{-9} mbar during the evaporation of the materials. The evaporation rate, monitored with a water-cooled quartz crystal microbalance, calibrated via X-ray reflectivity (XRR), varied between 0.13 and 0.16 nm/min. The temperature of the substrates was controlled and kept constant via a combination of resistive heating and liquid nitrogen cooling.

The substrate temperatures and other parameters used for the thin film growth are given in Table 7.2 and Table 7.3, respectively. The experiments using C_{60} were performed at the ID03 beamline at the European Synchrotron Radiation Facility (ESRF) using an energy of 11.0 keV (λ=1.126 Å) and a four chip MaxiPix area detector [202]. The DIP sample series was prepared and measured at the MS-X04SA/Surface Diffraction beamline at the Swiss Light Source (SLS) [183] using an energy of 12.4 keV (λ=0.999 Å) and a PILATUS II area detector. In both cases, slits directly in front of the detector were used to mimic a 0D point detector. The critical angles of the C_{60}/6T/nSiO and DIP/6T/nSiO systems are $\alpha_c = 0.15°$. The incidence angle used for all the in-plane measurements was $\alpha_i = 0.13°$. Real-time XRR of the deposition of C_{60} on the 6T templating layers were also performed. The duration of one scan was approximately 190 s which corresponds approximately to a thickness difference of 0.5 nm per scan. For DIP on 6T we performed real-time GIXD measurements. The time span between successive scans was 6 min which corresponds to a time-resolution of approximately 1.0 nm/scan. The Bragg peaks were fitted with Gaussians and Scherrer's formula was used to estimate the coherently scattering in-plane or out-of-plane crystalline size $D_{coh} = 2\pi \cdot 0.94/fwhm$, where 0.94 is Scherrer's constant for spherical crystallites and $fwhm$ is the full-width at half maximum of the fitted peaks. Note that no broadening due to the experimental setup is included in any calculations

of the coherently-scattering island size and hence the reported values have to be seen as lower limits. The XRR data were fitted with the Parratt formalism [123] using the GenX software [184]. The Kiessig oscillations in the low q_z region of the films were used to calculate the total film thickness. For the designation of the different peaks the crystal structures listed in Table 7.1 were used.

Table 7.1: **Crystal structures of 6T, C_{60} and DIP**

	a [nm]	b [nm]	c [nm]	α [°]	β [°]	γ [°]
6T LT-phase [143]	4.4708	0.7851	0.6029	90.00	90.76	90.00
6T β-phase [141, 142]	0.5667	0.7800	4.7288	90.00	100.6	90.00
C_{60} fcc [171]	1.4156	1.4156	1.4156	90.00	90.00	90.00
DIP [178]	0.709	0.867	1.690	90.00	92.2	90.00

7.3 Results

7.3.1 C_{60} on 6T

7.3.1.1 Characterization of The Templating Layers

For the investigation of the growth behaviour of C_{60} on 6T layers, the growth parameters of the latter were varied, resulting in films with different crystal structures and surface roughnesses. The substrate temperature during the deposition was varied between 308 K and 373 K and the films grown at 373 K were prepared with two different nominal thicknesses (5 nm and 20 nm). This resulted in thin films with different templating layers as summarized in Table 7.2.

The templates were characterised using X-ray reflectivity (XRR) and grazing incidence X-ray diffraction (GIXD). For XRR the momentum transfer has only a component which is perpendicular to the sample surface and therefore this technique probes the out-of-plane film structure. Information on the crystallinity, electron density profile, film thickness and roughness can be extracted [120–122]. On the contrary, GIXD is used to probe the in-plane structure of a thin film and q_{xy} is the in-plane momentum transfer [120–122]. Figure 7.2a and c show the data for the XRR and GIXD, respectively. Thicker 6T films show high out-of-plane order as evidenced by out-of-plane Bragg peaks at either $q_z = 0.28\,\text{Å}^{-1}$, $0.56\,\text{Å}^{-1}$ and $0.84\,\text{Å}^{-1}$ for the 20.9 nm 373 K film or $q_z = 0.266\,\text{Å}^{-1}$ and $0.513\,\text{Å}^{-1}$ for the 17.0 nm 308 K film (Fig. 7.2a).
The Parratt fits are shown as solid lines in Fig. 7.2a. The nominally 5.0 nm film was fitted up to $0.4\,\text{Å}^{-1}$. From the extracted electron density profile (Fig. 7.2b) we see that this film consists of two monolayers, each 2.64 nm thick. This is very

close to the value reported for the size of a single 6T molecule [90, 143]. This indicates that the molecules arrange in an almost upright standing orientation. This is in agreement with our previous results that 6T tends to form crystallites of the β-phase close to the substrate [83]. Since the film consists of only two monolayers we assume that it comprises mostly of β-phase domains. The top surface is smooth with a roughness of only 0.3 nm. The GIXD data (in-plane) (Fig. 7.2c) show only Bragg peaks which can be associated with the β-phase and peaks which originate from the LT-phase (like 6T LT (0 1 1) and (0 2 1)) are not observed. This confirms the estimation that the film consists of only β-phase crystallites which is in agreement with real-time growth results, showing that close to the substrate the film growth is dominantly in the β-phase [83].

Thicker films (nominally 20 nm) were prepared at two different substrate temperatures, 373 K and 308 K. The film structure is in agreement with earlier reports [83]. The out-of-plane data of the film prepared at 373 K (black curve in Fig. 7.2) show only damped, weak oscillations in the low q_z range, indicating a roughness of 5.3 nm. The XRR data are dominated mostly by Bragg reflections of the LT-phase. The extracted electron density profile (Fig. 7.2b) shows that the film consists of five completely full layers and eight partially filled layers on top, constituting the roughness and an island-like growth. The thickness of one single molecule-layer is 2.29 nm which corresponds very well to the value reported for the LT-phase [143]. The in-plane data reveal that there are crystallites of the β-phase, however the reflections belonging to the LT-phase are dominant. The films prepared at 308 K are different from the high temperature films. Here, the structure is dominated by the β-phase but the roughness is similar to the one of the 373 K film. In this case the extracted electron density profile (Fig. 7.2b) indicates that the film consists of four completely filled layers and six incompletely filled layers, where the latter are less filled compared with the ones of the 373 K film. The monolayer thickness extracted from the fit is 2.44 nm which is close to the value reported for the β-phase [141]. The in-plane data show weak reflections which can be associated with the LT-phase. To summarize, the three different templating layers have different crystal structures (also in different quality) and roughnesses. There are three different scenarios: The 5 nm thin film consists purely of the β-phase and is very smooth. The nominal 20 nm film prepared at 373 K is dominated by the LT-phase and the roughness is significantly higher than the one of the 5 nm. The 303 K film has more domains of the β-phase than of the LT-phase and the roughness is similar to the one of the high temperature film.

7.3.1.2 C_{60} Films on Top of 6T Templates

On the different templating layers previously described, C_{60} films with a nominal thickness of 20 nm were deposited. The substrate temperature, and hence also

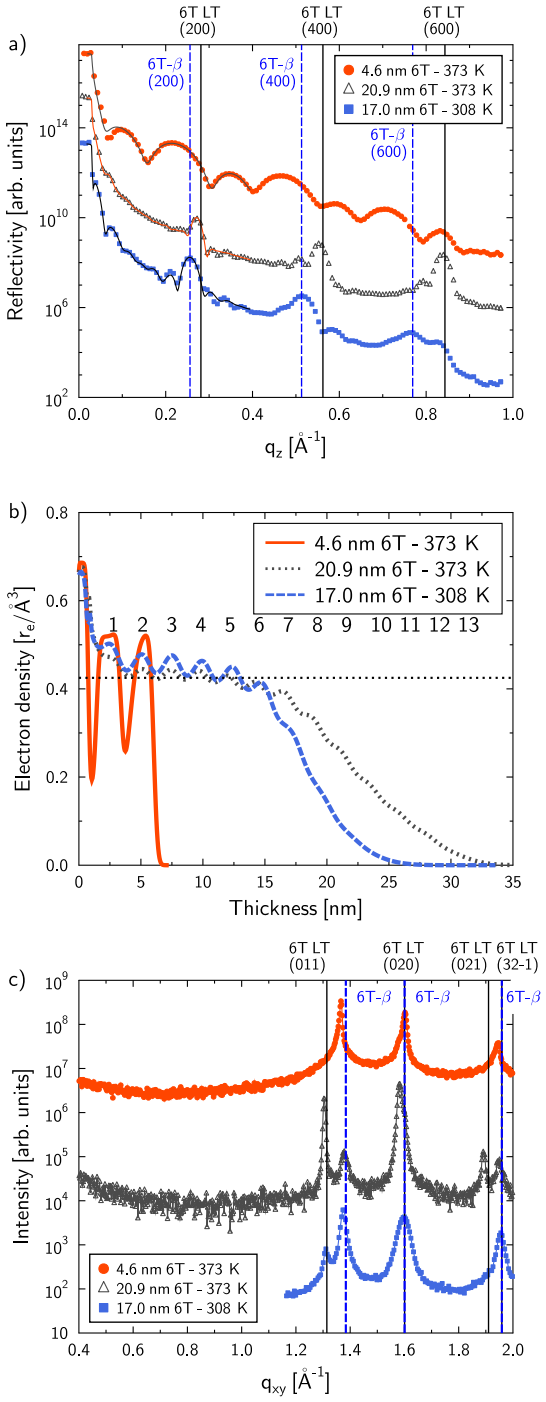

Figure 7.2: a) XRR and c) GIXD data of the templating layers used for the growth of C_{60}. The solid line in a) corresponds to the fit of the data using Parratt's formalism. b) shows the extracted electron density profile of the different films; the numbers refer to layers of 6T and the dotted horizontal line indicates the difference between completely and only partially filled layers. The curves in a) and c) are shifted for clarity.

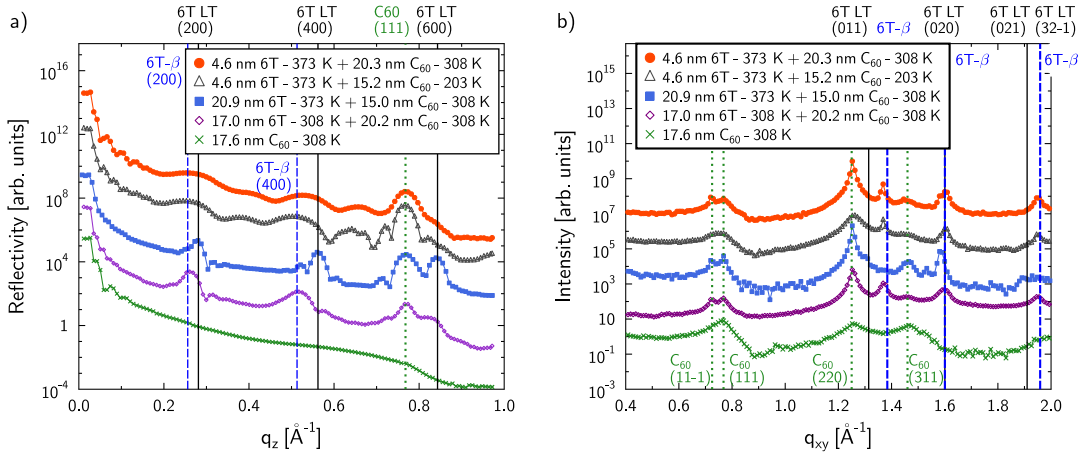

Figure 7.3: a) XRR and b) GIXD data of nominally 20 nm C_{60} deposited on the template layers, respectively. Curves are shifted for clarity.

the temperature of the 6T film, were set to 308 K, for all but one film, for which a substrate temperature of 203 K was used. XRR (GIXD) data of the resulting films are presented in Fig. 7.3a (b). For comparison, data of a 20 nm C_{60} film deposited straight on nSiO (green crosses) are also shown alongside. XRR of pure C_{60} does not show clear Bragg reflections consistent with a polycrystalline growth without any preferential direction on nSiO [176]. The in-plane data of C_{60} on nSiO show relatively broad Bragg reflections, which can be related to the fcc structure of C_{60} [171]. In thin film-growth on weakly interacting substrates, like nSiO, C_{60} usually grows polycrystalline without a preferred orientation, which can explain the relatively broad peaks [176]. As soon as a 6T template is used, the out-of-plane structure of the C_{60} improves drastically. The data for films with 6T below the C_{60} in Fig. 7.3a all show a reflection corresponding to the C_{60} (1 1 1) fcc at $q_z = 0.768\,\text{Å}^{-1}$. The coherently scattering out-of-plane domain size $D_{coh\perp}$ of C_{60} was estimated by fitting the C_{60} (1 1 1) Bragg peak. The film parameters are summarized in Table 7.2.

The highest out-of-plane coherently scattering island size (21.3 nm) is obtained for films prepared at 308 K on a templating layer of 5 nm grown at 373 K. Comparing $D_{coh\perp}$ to the estimated film thickness of C_{60}, one sees that the two values are very similar, indicating that the coherently scattering crystallites are formed over the whole film thickness. For the same templating parameters, $D_{coh\perp}$ is significantly smaller ($D_{coh\perp} = 12.3\,\text{nm}$) when the substrate temperature is set to 203 K. However, the estimated film thickness is also smaller, showing that still the crystallites grow over a relatively wide thickness range. Basically, the whole film is already ordered quite well perpendicular to the substrate surface, increasing the thickness of the templating layer does not show any further improvement ($D_{coh\perp} = 17.8\,\text{nm}$ for a C_{60} thickness of 15.0 nm). For the C_{60} film on top of the 308 K 6T film the fitted C_{60} Bragg peak is strongly distorted by the 3rd order

Table 7.2: **Summary of the 6T - C_{60} Film Parameters**

6T					C_{60}			
T [K]	d [nm]	σ [nm]	$D_{coh\parallel}$ LT [nm]	$D_{coh\parallel}$ β [nm]	T [K]	d [nm]	$D_{coh\perp}$ [nm]	$D_{coh\parallel}$ [nm]
373	4.6	0.3	n.a.	54.7	308	20.3	21.3	52.7
373	4.6	0.3	n.a.	50.4	203	15.2	12.3	11.9
373	20.9	5.3	75.7	n.a.	308	15.0	17.8	69.4
308	17.0	3.3	n.a.	25.1	308	20.2	19.9	35.1
n.a.	n.a.	n.a.	n.a.	n.a	308	17.6	n.a.	8.0

The parameters of the different templating layers: substrate temperature T, thickness d, roughness σ, coherently scattering in-plane domain size $D_{coh\parallel}$ of the LT- and β-phase. The parameters of the C_{60} layers on the templating layers: substrate temperature T, thickness d, coherently scattering out-of-plane domain size $D_{coh\perp}$, coherently scattering in-plane domain size $D_{coh\parallel}$ calculated from the width of the (2-2 0) Bragg peak.

Bragg peak of the underlying 6T β-phase, therefore both Bragg peaks were fitted. Also, in this case, the estimated $D_{coh\perp} = 19.9\,\text{nm}$ coincides very well with the estimated C_{60} thickness of 20.2 nm.
We performed real-time XRR during the deposition of C_{60} on the 5 nm 6T template at 203 K and 308 K to see the evolution of the C_{60} structure and monitor potential changes in the underlying template layer during the C_{60} deposition. The data are depicted in Fig. 7.4. For both substrate temperatures, the C_{60} Bragg peak starts to evolve after the deposition of approximately 2 nm (for out-of-plane Bragg diffractions at least two coherently scattering layers are necessary). So C_{60} grows on the template with a well-ordered crystal structure. Furthermore, a shift of the 6T Bragg reflection around $q_z = 0.5\,\text{Å}^{-1}$ is observed, which corresponds to the second order Bragg peak of the β-phase, with increasing amount of deposited C_{60}. In case of the 203 K film the Bragg peak is shifted from 0.470 to $0.504\,\text{Å}^{-1}$ (corresponding to a shift from 2.68 to 2.49 nm in real-space) and in the 308 K film the shift is from 0.474 to $0.515\,\text{Å}^{-1}$ (out-of plane repeat distance changes from 2.65 to 2.44 nm), respectively. In both cases, the q_z value of the Bragg peak is close to the one expected for the β-phase (q_z of the (4 0 0) β-peak should be $0.513\,\text{Å}^{-1}$). Most likely, the additional C_{60} is slightly compressing the underlying 6T, leading to a small change of the 6T tilt angle and hence the layer distance.

The in-plane structure of the different C_{60} films was characterized via GIXD (Fig. 7.3b). Beside the Bragg reflections of the 6T templating layers (previously described) Bragg peaks which can be assigned to the C_{60} fcc structure are observed [171].

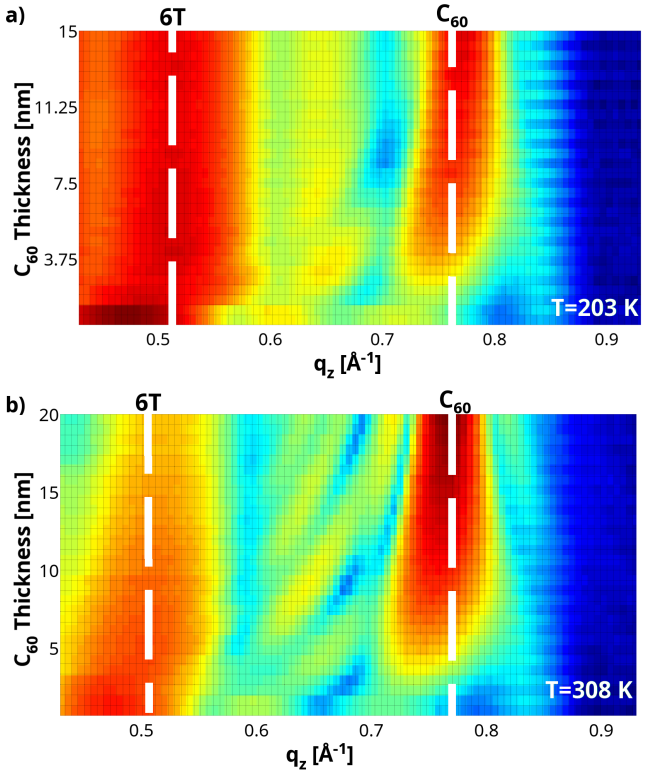

Figure 7.4: Real-time XRR data of the deposition of C_{60} on 5 nm of 6T at a substrate temperature of a) 203 K and b) 308 K. The time step between two successive scans was 190 s which corresponds to 0.5 nm deposited C_{60}. The labels 6T and C_{60} indicate the Bragg peak positions of the 6T-β (4 0 0) and the C_{60} (1 1 1) reflections, respectively. Note that C_{60} thickness can be transcribed to growth time.

Overall, the C_{60} Bragg peaks on 6T templates are relatively sharp. For the films prepared at 308 K on a templating layer, a peak at $q_{xy} = 0.725$ Å^{-1} is observed, which is not visible for the pure C_{60} or the film grown at a substrate temperature of 203 K. From reports of C_{60} on DIP templating layers [176] we conclude that this peak is the projection of the C_{60} (1 1 -1) peak onto the q_{xy} plane, and hence an indicator of very well aligned crystalline domains within the C_{60}.
For a more detailed investigation, the 6T and the C_{60} in-plane coherently scattering crystal size $D_{coh\|}$ was calculated form the widths of the Bragg peaks. The values for the 6T LT (0 1 1) peak, the 6T peak at $q_{xy} = 1.38$ Å^{-1} corresponding to the β-phase and the C_{60} (2 -2 0) are listed in Table 7.2. By comparing the values of the 6T crystallites to those of the C_{60} layer one sees that the crystallites of both materials are of similar size in the in-plane direction. It seems that for 373 K this effect is independent of the type of crystal structure of the bottom layer, *e.g.* β-phase vs. LT-crystal phase. For the case when the substrate temperature during the C_{60} deposition is only 203 K (on the nSiO) $D_{coh\|}$ of C_{60} is smaller than that for the other films and also significantly smaller than $D_{coh\|}$ of the 6T templating

layer. However, the crystallite size (11.9 nm) is still larger than the value of pure C_{60} at 308 K ($D_{coh\|} \approx 8.0$ nm).
In general, the 6T template layers improve the crystallinity of the C_{60} for all preparation conditions. The C_{60} tends to organise in crystal domains with the (1 1 1) plane parallel to the substrate surface. $D_{coh\|}$ of the C_{60} and that of the 6T are very similar, indicating that there is a strong templating effect of the underlying 6T on the C_{60}.

7.3.2 DIP on 6T

7.3.2.1 Characterization of the Templating Layers

For the investigation of the templating effects of 6T on the rod-like molecule DIP three different layers of 6T were prepared. The 6T film structure was modified by altering the substrate temperature during the growth. XRR and GIXD data of the templating layers prepared at 373 K (red circles), 308 K (black triangles) and 233 K (blue squares) are shown in Fig. 7.5a and b, respectively. The thickness of all templating layers was nominally 20 nm. For the 373 K template the out-of-plane Bragg reflections up to the (10 0 0) LT peak indicate that the film is very well ordered perpendicular to the substrate surface. The peaks can be identified as belonging to the standing-up orientation of 6T LT crystal phase. Close to the LT (2 0 0) and (4 0 0) peaks, the first two orders of the Bragg peak of the standing-up β-phase are also observed. The data of the 308 K template film indicates that this film is not as nicely ordered as the 373 K template one. Furthermore, this film is dominated by the β-phase and only a minor fraction consists of the LT-crystal phase. The template prepared at 233 K shows only broad Bragg peaks of the β-phase. No peaks corresponding to the LT-phase are observed. The presence of the β-phase Bragg peaks indicate that some molecules still organise (although weakly) in a standing-up orientation. The film parameters extracted from fitting the data are listed in Table 7.3.

The GIXD data (Fig. 7.5b) confirms that the film prepared at 373 K consists of upright-standing molecules mostly within the LT-crystal phase, but some fraction is in the β-phase. It has been reported using real-time observations during growth that this β-phase is predominant during early stages of growth and beyond a critical thickness the molecules grow mostly in the LT-phase [83]. The film prepared at 308 K consists mostly of the standing-up configuration of the β-phase (Note that the diffraction intensity around the 6T LT (0 2 0) reflection might also partly originate from the β-phase). For the film grown at 233 K, the structure of the film is different. In this case, only standing-up molecules in the β-phase can be identified. However, weak reflections at $q_{xy} = 0.28$ Å^{-1}, 0.56 Å^{-1} and 0.84 Å^{-1} indicate that a fraction of the film consists of 6T molecules that orient in the lying-down configuration as is expected for growth at low substrate temperature. From the absence of the (-4 1 1) peak in the out-of-plane data (at

$q_z = 1.411\text{Å}^{-1}$ in Fig. 7.5a) we conclude that the (0 1 0) plane of the lying-down 6T is parallel to the substrate surface. However, it can not be completely excluded that some fractions of the 6T are oriented with the (-4 1 1) plane parallel to the surface, as also observed for lying-down 6T on Cu(1 1 0) [158].

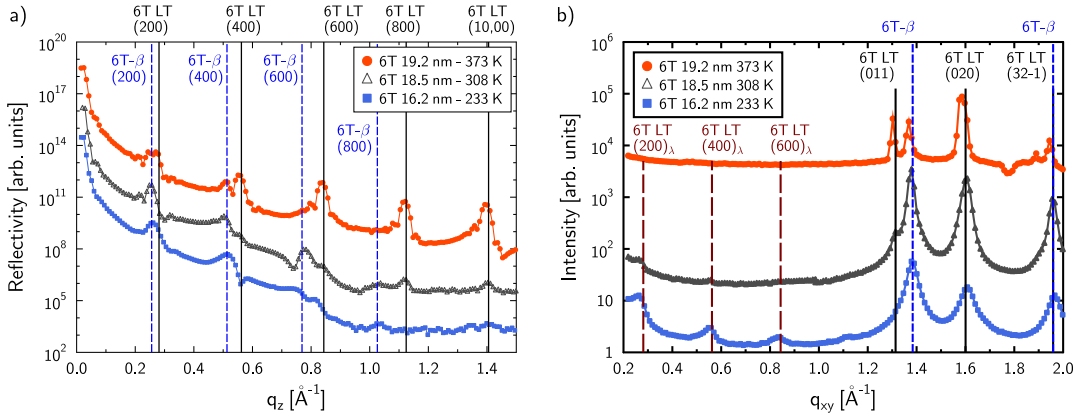

Figure 7.5: a) XRR and b) GIXD data of the 6T templating layers used for the growth of DIP. The curves are shifted with respect to each other for clarity. The annotations with a small λ indicate a lying-down orientation of 6T and the other ones correspond to Bragg peaks of standing-up oriented domains. Adopted from [83].

7.3.2.2 DIP Films on Top of 6T

To investigate the influence of the 6T templating layer on the growth of DIP, we prepared DIP layers with a nominal thickness of 20 nm on top of the 6T layers. The substrate temperature during the deposition of the DIP was the same as the one used for the preparation of the templating layers, *i. e.* 233 K, 308 K and 373 K, respectively. Fig. 7.6a and b show the XRR and GIXD data of the complete heterostructures, respectively. The 373 K film shows Bragg reflections at $q_z = 0.37\,\text{Å}^{-1}$ and $0.74\,\text{Å}^{-1}$ which corresponds to the standing-up (σ-orientation) of DIP [186]. In the 308 K film the weak out-of-plane Bragg peaks of the σ-orientation DIP imply that the out-of-plane order of the DIP film is significantly smaller than in the 373 K film. At low substrate temperature, 233 K, the XRR data do not show any indications of standing-up DIP at all. The very weak reflection at $q_z = 1.22\,\text{Å}^{-1}$ stems from a lying orientation of the DIP [179].

The in-plane data of the 6T/DIP films (Fig. 7.6b) indicate similar orientation of the molecules as obtained from the XRR data. $D_{coh\|}$ values extracted from the data are summarized in Table 7.3. For the lying 6T (λ-orientation) the (2 0 0) peak at $q_{xy} = 0.27\,\text{Å}^{-1}$, for the lying DIP ($\lambda$-orientation) the (0 0 1) peak at $q_{xy} = 0.37\,\text{Å}^{-1}$, for the 6T β-phase the peak at $q_{xy} = 1.38\,\text{Å}^{-1}$, for the standing-up orientation of the 6T LT-phase the (0 1 1) peak at $q_{xy} = 1.30\,\text{Å}^{-1}$ and for the standing DIP molecules (σ-orientation) the (1 1 0) peak at $q_{xy} = 1.16\,\text{Å}^{-1}$ were

considered, respectively. The 373 K film shows only reflections stemming from crystallites comprising of standing-up oriented molecules. $D_{coh\|}$ of the standing molecules for 6T and DIP is very similar for this film. Interestingly, the ratio of the intensities of the 6T LT (0 1 1) and the 6T β (at $q_{xy} = 1.38\,\text{Å}^{-1}$) reflections in the final heterostructure is quite different compared with the pure templating layer. In the latter (Fig. 7.5b), both peaks show very similar intensities, however, in the film with DIP on top the LT peak is significantly stronger than the β-peak. This is most likely due to an annealing effect on the pure 6T, because the sample was kept at 373 K for approximately 130 minutes (duration of the post-growth measurements and of the preparation for the DIP deposition). We will discuss the transition between the two crystal structures in detail later with the real-time data taken during DIP deposition. A small fraction of the 308 K film consists of lying-down molecules, indicated by the small peaks in the low q_{xy} range. $D_{coh\|}$ for 6T and DIP lying-down domains is very similar (14.3 and 15.2 nm, respectively). The peak with the highest intensity corresponding to the 6T layer is the one of the standing up β-phase. Furthermore, peaks corresponding to standing-up orientation of DIP (at $q_{xy} = 1.15\,\text{Å}^{-1}$, $1.46\,\text{Å}^{-1}$ and $1.71\,\text{Å}^{-1}$) are observed. Again, $D_{coh\|}$ of the standing-up orientation of 6T and DIP are very similar (20.5 nm and 21.1 nm). The films prepared at 233 K show relatively strong reflections in the low q_{xy} range, stemming from domains of lying-down 6T and DIP. Also in this case $D_{coh\|}$ of 6T and DIP is very similar, however, the intensity of the lying-down DIP domains is significantly higher than the one of 6T and also than the intensity of the standing-up DIP. This indicates that most of the DIP is arranged in a lying-down orientation. Standing-up molecules of the 6T are found only in the β-structure and very weak peaks of standing-up DIP indicate that only a small fraction of this orientation is present in the film. $D_{coh\|}$ of standing up 6T and DIP is again of similar magnitudes (15.4 nm and 10.3 nm).
In general, we have seen that low substrate temperatures promote the growth of lying-down DIP, whereas high substrate temperatures lead to better ordered DIP films (*e.g.* higher $D_{coh\|}$) with a standing-up orientation. This is similar to results reported for DIP on nSiO [178]. Interestingly, for all substrate temperatures and both orientations (standing-up and lying-down), there is a strong correlation of $D_{coh\|}$ between the templating 6T layer and the top DIP layer. This leads to the proposition that the domains of DIP are arranged in the same orientation as the underlying 6T domains, *i.e.* lying-down DIP on lying-down 6T and standing-up DIP on standing-up 6T.

For a better understanding of the templating effect on the growth process of the overlayer we performed real-time GIXD scans during the deposition of the DIP layer. Two different q_{xy} ranges ($0.2 - 0.7\,\text{Å}^{-1}$ and $1.25 - 1.8\,\text{Å}^{-1}$) were measured alternately and are shown in Fig. 7.7. In the top row (a-c) the data of the first q_{xy} range and in the second row (d-f) the data of the second q_{xy} range are plotted, respectively. For the 233 K film, mainly the evolution of the lying DIP can be followed (Fig. 7.7a). Approximately after 24 mins (~ 5 nm) of film growth

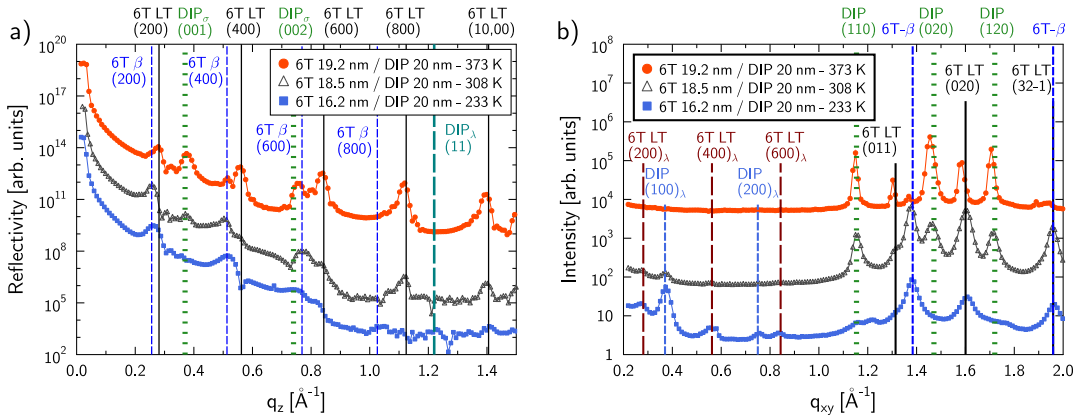

Figure 7.6: a) XRR and b) GIXD data of nominally 20 nm DIP films prepared at 233 K, 308 K and 373 K substrate temperature on 6T layers. Peaks labeled with a small λ correspond to lying-down oriented molecules whereas peaks of standing-up oriented molecules have either no or a small σ label. Curves are shifted for clarity.

Table 7.3: **Summary of the 6T - DIP Film Parameters**

6T						DIP	
T [K]	d [nm]	σ [nm]	$D_{coh\|\|}$ λ [nm]	$D_{coh\|\|}$ LT [nm]	$D_{coh\|\|}$ β [nm]	$D_{coh\|\|}$ λ [nm]	$D_{coh\|\|}$ σ [nm]
373	19.2	3.1	n.a.	44.0	n.a.	n.a.	40.5
308	18.5	3.1	14.3	n.a.	20.5	15.2	21.1
233	16.2	3.8	15.4	n.a.	15.4	17.0	10.3

Parameters of the different templating layers: substrate temperature T, film thickness d, roughness σ, in-plane coherently scattering domain sizes $D_{coh\|\|}$ of the lying 6T (6T$_\lambda$ - (2 0 0)$_\lambda$ peak), the 6T-LT phase ((0 1 1) peak) and the 6T β-phase (peak at q_{xy} =1.38 Å^{-1}). Parameters of the DIP layer: $D_{coh\|\|}$ of lying-down oriented molecules (DIP$_\lambda$ - (0 0 1)$_\lambda$ peak) and of standing-up oriented molecules (DIP$_\sigma$ - (1 1 0) peak).

the formation of the Bragg peak starts to appear, indicating the formation of crystalline domains. The DIP $(0\,0\,1)_\lambda$ peak gets stronger and sharper over the whole growth process.

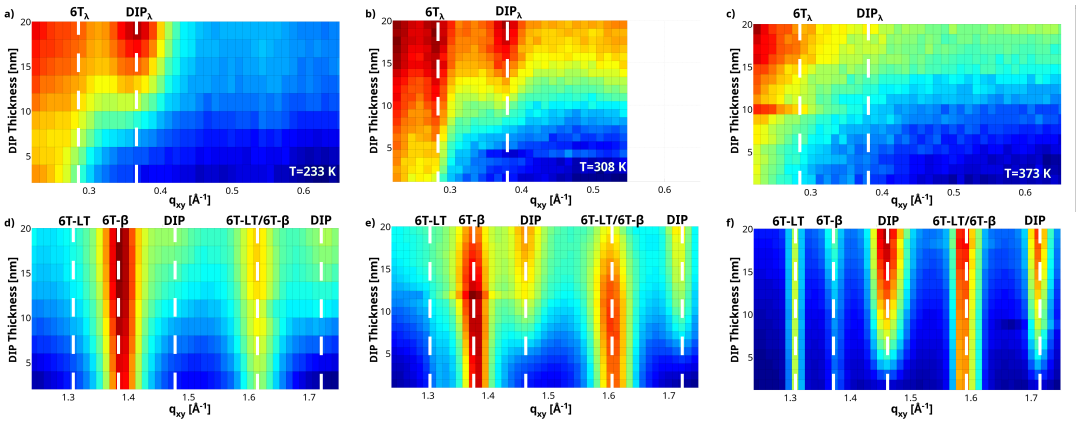

Figure 7.7: Real-time GIXD data taken during the deposition of the DIP deposition on 6T. a), b) and c) depict the q_{xy} range which shows the evolution of the lying-down orientation of the molecules for 233 K, 308 K and 373 K substrate temperature, respectively. 6T$_\lambda$ ($q_{xy} = 0.28\,\text{Å}^{-1}$ (2 0 0) LT-phase) and DIP$_\lambda$ ($q_{xy} = 0.37\,\text{Å}^{-1}$ (1 0 0)) indicate the positions of Bragg peaks corresponding to lying-down molecules of the materials. d), e) and f) show the q_{xy} range where reflections of molecules in the standing-up orientation are detected for 233 K, 308 K and 373 K substrate temperature, respectively. Here 6T-LT ($q_{xy} = 1.31\,\text{Å}^{-1}$ (0 1 1) LT-phase) and 6T-β indicates Bragg peak positions which can be unambiguously associated with the 6T LT and β-phase, respectively, whereas the peak at $q_{xy} = 1.6\,\text{Å}^{-1}$ can be associated either with the LT ((0 2 0) reflection) or the β-phase. The DIP label indicates Bragg peak positions of standing-up DIP molecules ($q_{xy} = 1.46\,\text{Å}^{-1}$ (0 2 0) and $q_{xy} = 1.71\,\text{Å}^{-1}$ (1 2 0)). Note that DIP thickness can be transcribed to growth time.

The signal of the DIP standing-up domains (Fig. 7.7d) is relatively weak. For films at 308 K, the growth of the lying-down DIP is quite similar to the one of the film prepared at 233 K. For the first 5 nm of growth, no indications of lying-down DIP can be found (Fig. 7.7d) and only after this thickness, crystallites start forming. Nevertheless, the intensity of the corresponding DIP Bragg peak is only increasing slowly, and, as already mentioned, the intensity at the end of the film growth is significantly lower than the one in the 233 K film. The standing-up oriented DIP molecules start to form domains only after approximately 5 nm, as evidenced by the formation of the DIP (0 2 0) and (1 2 0) peak at $q_{xy} = 1.46\,\text{Å}^{-1}$ and $1.71\,\text{Å}^{-1}$, respectively. During the growth, $D_{coh\|}$ of the DIP (0 2 0) and (1 2 0) peaks increases from 12.5 to 16.0 nm and 13.5 to 21.6 nm, respectively (blue symbols in Fig. 7.8).

At a substrate temperature of 373 K, no domains with lying-down oriented molecules can be observed (Fig. 7.7c). The (0 1 1) 6T LT-phase peak ($q_{xy} =$

1.30 Å^{-1}) stays constant during the whole film growth. However, the intensity of the Bragg peak corresponding to the 6T β-phase (q_{xy} = 1.38 Å^{-1}) increases during the DIP deposition. At the beginning of the DIP deposition this peak is almost not visible, which is contrary to the post-growth characterization of the 6T templating layer. As previously mentioned, this might be explained by a post-growth annealing. Then, during the DIP deposition, the intensity of the β-phase Bragg peak starts to increase again after 10 nm deposition of DIP showing that domains corresponding to the 6T β-phase start evolving again. However, $D_{coh\parallel}$ of the 6T β-phase is not changing. In contrast with the films prepared at lower substrate temperature, in the case of 373 K the DIP crystallites of the σ-orientation are formed almost immediately after the start of the deposition; already after the growth of 1 monolayer, reflections from DIP are observed. During further growth, the intensities of the DIP Bragg peaks increases with more amount of material being deposited but the *fwhm* of the peaks are not changing significantly. During the first 5 nm of growth $D_{coh\parallel}$ of the DIP (0 2 0) and (1 2 0) peaks increase to $\sim$ 20 nm and $\sim$ 30 nm and then stay more or less constant for the rest of the film growth (red symbols in Fig. 7.8). Please note that $D_{coh\parallel}$ of the DIP (1 2 0) peak after a film thickness of $\sim$ 20 nm is resolution limited (shaded area in Fig. 7.8) and therefore we cannot rule out a larger $D_{coh\parallel}$.

7.4 Discussion

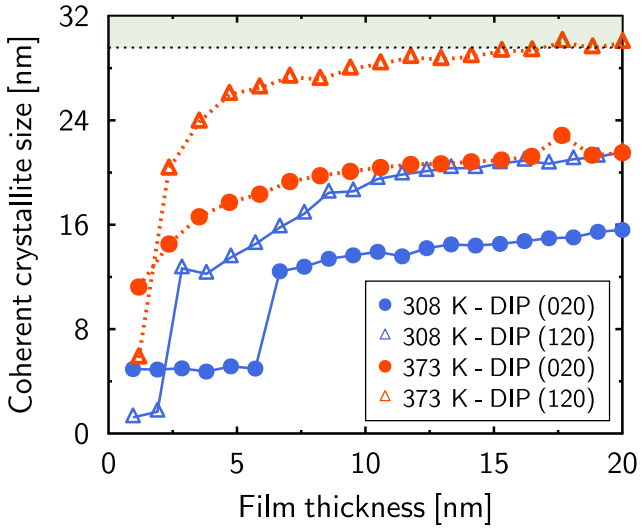

Figure 7.8: Evolution of the coherently scattering island sizes for the DIP (0 2 0) and (1 2 0) reflections of the films prepared at 308 K and 373 K substrate temperature. The shaded area indicates the resolution limit of the DIP (1 2 0) peak.

The results of the bilayers of 6T and C_{60} as well as of 6T and DIP have

shown that 6T has a strong templating effect on both materials used as top-layer. The in-plane coherently scattering size $D_{coh\parallel}$ of the templating 6T layers and the one of the material deposited on top show a strong correlation, indicating that generally the top material seems to adopt the configuration of the bottom material and forms nicely organised domains right on-top of the crystallites of the templating layer. C_{60} on 6T seems to organise itself from the beginning with its (1 1 1) plane parallel to the substrate plane instead of growing with completely randomly oriented domains, most likely due to a different surface potential distribution of the 6T layer compared with nSiO. This also results in a better defined out-of-plane structure of the film. At lower substrate temperatures (203 K) the templating effect is still observed, however not as pronounced as observed for the films prepared at 308 K or 373 K. At 203 K the thermal energy provided by the substrate is not enough to allow the C_{60} to diffuse on the substrate surface to find a potential minimum on-top of the 6T.

A templating effect of DIP is also observed on 6T. Since the coherent domain sizes of the underlying 6T and the DIP deposited on top are very similar, we expect a growth scenario where the DIP crystallites are formed directly on top of the respective domains below. Both materials deposited on top, C_{60} and DIP, act as electron acceptor in contact with 6T and hence form donor-acceptor pairs with the latter [27]. In such pairs charge transfer mechanisms are likely to occur and usually lead to relatively strong coupling between the molecules. This might be the reason for the orientational templating of DIP on 6T and the well-oriented growth of C_{60} on 6T, which was already reported also for DIP [198] and pentacene [203].
Furthermore, the structural change of the bottom 6T templating layer during the deposition of DIP at 373 K indicates that organic thin films are sensitive to post-growth treatment. In this case the additional material leads to a partial reorganization of the 6T layer wherein domains of the LT structure change into domains of the β-phase, which is not a pure annealing effect since this transition is not observed for 6T films without a DIP overlayer. However, the structural change of the 6T layer during the deposition of C_{60} (decrease in the out-of-plane repeat distance) is similar to an annealing effect where 6T domains are transformed into the thermodynamically more stable LT-phase.

7.5 Conclusion

In conclusion, we have investigated the growth of the electron donor-acceptor pairs 6T - C_{60} and 6T - DIP by means of X-ray scattering techniques in real-time and *in situ*. For both material combinations a very strong correlation between the coherently scattering domain size of the templating 6T layer and of the acceptor material is observed. This pronounced templating effect might be attributed to a strong interaction between the materials, potentially by a charge transfer from the

donor to the acceptor material. The deposition of C_{60} on top of 6T has a similar effect as an annealing step of pure 6T. Furthermore, the re-appearance of the β-phase crystallites in the 6T bottom layer during the deposition of DIP indicates that post-growth treatment of an organic thin film, in our case the deposition of an additional organic semiconductor on top, can, under certain circumstances, change the original layer structure.

Chapter 8

Growth and Annealing Kinetics of α-Sexithiophene and C_{60} Mixed Films

The results presented in this section are published in Ref. [204][1].

8.1 Introduction

The material combination α-sexithiophene ($C_{24}H_{14}S_6$, 6T) and Buckminsterfullerene C_{60} (Fig. 8.1a and b) can be employed as donor-acceptor pair, in the PHJ geometry [27] as well as in the BHJ one [24, 205]. For PHJs, interesting effects of the mutual arrangement and orientation of the two materials on the open-circuit voltage are reported [28]. For BHJ devices with 6T and C_{60} or C_{70}, respectively, an improvement of the solar cell device-parameters upon annealing is found [25, 193]. Several studies have shown that this kind of post-growth treatment can be employed to modify device parameters [206–208], including optical ones [209, 210] as well as the structure [211–213].
Pure 6T tends to grow in different crystal structures, depending on the type of layer (*i.e.* thin film or single crystal) and the preparation conditions [141–144, 151, 155]. In thin films, 6T mostly adopts two different crystal structures in the standing-up orientations, either the low-temperature single crystal phase (LT-phase) [143] or the β-phase [141,142]. Also, coexistence of both phases in thin films has been observed [82, 83]. The LT-phase is dominant for low deposition rates or at elevated substrate temperature (373 K), whereas the β-phase dominates at higher deposition rates and at low substrate temperatures (233 K and 308 K) [82, 83]. Generally, for nSiO substrates the β-phase is formed closely

[1] C. Lorch, K. Broch, V. Belova, G. Duva, A. Hinderhofer, A. Gerlach, M. Jankowski, and F. Schreiber, **submitted to J. Appl. Cryst.**: *Growth and Annealing Kinetics of α-Sexithiophene and Buckminsterfullerene C_{60} Mixed Films.*

to the substrate and above a certain thickness a transition to growth dominated by the LT-phase occurs [83]. The β-phase is energetically less stable compared to the LT-phase, but kinetically favoured [82,83].The rotational symmetry of C_{60} at room temperature [174] simplifies the possible growth scenarios, because there are no different orientations, *i.e.* standing-up versus lying-down molecules. Thin films of C_{60} are found to show low structural order on inorganic substrates such as SiO_2 [175], quartz glass [214] and sapphire [215]. However, on organic layers like pentacene [203, 215], diindenoperylene [176] or sexiphenyl [94, 216] an enhanced crystallinity of C_{60} layers is reported, similar to templating layers of 6T [28, 192].

In order to characterize the mixing behavior of C_{60} and 6T, we performed

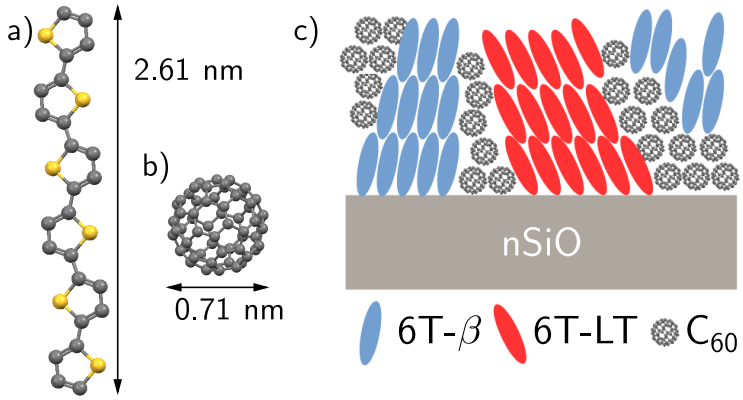

Figure 8.1: a) Schematic of the 6T molecule (size from Ref. [143]) and b) the C_{60} molecule (size from Refs. [199,200]). c) Schematic of the mixing of 6T and C_{60} with the two different crystal phases indicated, which are observed in the growth of the mixtures.

real-time *in situ* grazing incidence X-ray diffraction (GIXD) experiments. The films were characterized post-growth, using X-ray reflectivity (XRR), wide-range GIXD-scans and recording reciprocal space maps. After detailed post growth characterization, the films were annealed in order to investigate structural changes. Performing the experiments directly under high vacuum conditions ensures that effects such as degradation of the structure or incorporation of impurities due to the exposure to ambient conditions are excluded. Furthermore, transient effects can only be identified, if the growth is followed directly in real-time [22, 78, 106, 180, 181, 191, 201, 217]. Films with three different mixing ratios were prepared. Nominally, the molecular ratios were set to 6T:C_{60} 3:1, 1:1 and 1:3. All films were grown at 303 K or 373 K substrate temperature. As reference samples, films of the pure materials were prepared. In the following, we will refer to the data as 6T:C_{60} ($m:n$) 303 K (373 K) for the different ratios ($m:n$) prepared at different substrate temperature. Depending on the substrate temperature, either the 6T LT-phase or the 6T β-phase dominates the growth whereas the C_{60} grows mainly in randomly oriented domains (Fig. 8.1c).

8.2 Experimental

6T was purchased from Sigma Aldrich and purified twice by temperature gradient sublimation. C_{60} was purchased from Creaphys and used without further purification. The samples were prepared and studied in a portable vacuum chamber ($p = 1 \cdot 10^{-8}$ mbar) [137]. Before the installation, the silicon (nSiO) substrates with a native oxide layer of 2.0 nm were cleaned in an ultrasonic bath with acetone, isopropanol and demineralized water. Before each sample preparation the substrates were heated to 770 K to desorb the previously grown film. The deposition rates between $0.3 - 0.5$ nm/min were monitored using a water-cooled quartz crystal microbalance (QCM), which was calibrated via XRR. The nominal thickness of all films was 20 nm. The nSiO substrates were mounted on a molybdenum sample holder, cooled by liquid nitrogen and heated resistively. The substrate temperature was monitored using a K-type thermocouple attached to the sample holder in close proximity to the substrates. All samples were measured at the same temperature as prepared. All experiments were performed at the ID03 beamline at the European Synchrotron Radiation Facility (ESRF) using a monochromatic X-ray beam at 20.0 keV (wavelength 0.6199 Å). Diffraction images were recorded using a MaxiPix area detector [202]. Slits directly in front of the detector were used to mimic a 0d point detector where needed. For the qualitative peak analysis no instrumental broadening is included in the calculations, therefore the reported values for the coherently scattering sizes are lower limits. The critical angle of nSiO is $\alpha_c = 0.08°$. To obtain maximum surface sensitivity, we chose an incidence angle of $\alpha_i = 0.075°$ for the measurements. The time difference between the start of two successive real-time GIXD scans was 260 seconds. With the used deposition rates this results in a 1.3-2.1 nm thickness resolution. For further analysis, 2d reciprocal space maps were recorded with fully open detector slits.

8.3 Results

8.3.1 X-ray Reflectivity

XRR was used to investigate the out-of-plane structure of the 6T:C_{60} mixed and pure films. Fig. 8.2a depicts the data obtained for the films prepared at a substrate temperature of 303 K. The structure of the pure 6T film at 303 K is consistent with the one reported previously [83]. The out-of-plane structure shows features belonging to the β-phase as well as the LT-phase, in particular, Bragg peaks of the standing-up oriented LT-phase up to the $12th$ order. Under the applied preparation conditions, pure C_{60} does not form a well ordered out-of-plane structure, since no characteristic out-of-plane reflections of C_{60} are observed. All

Bragg peaks seen for the mixtures prepared at 303 K originate from 6T domains [141–143].

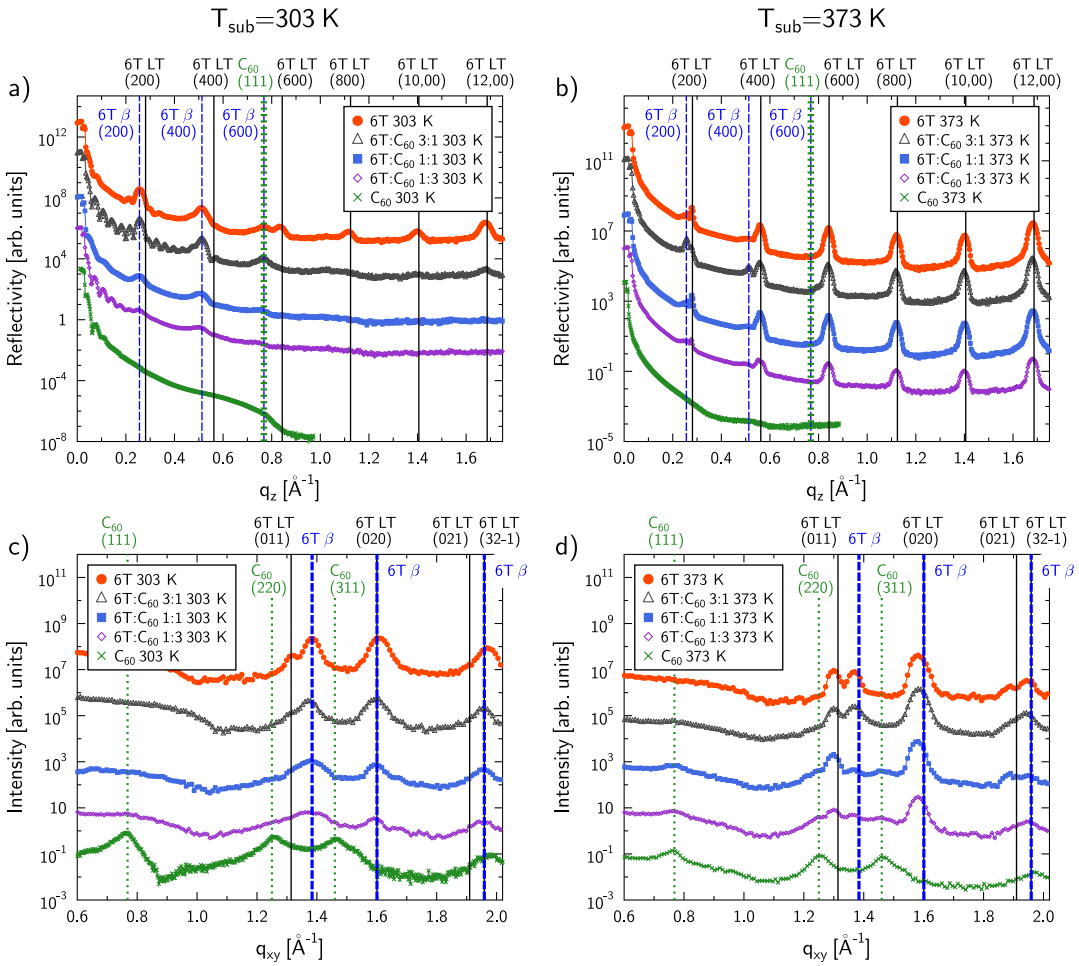

Figure 8.2: a), b) XRR data and c), d) GIXD data of different mixing ratios at a),c) 303 K and b),d) 373 K substrate temperature.

For the 6T:C_{60} (3 : 1) 303 K mixture the first six orders of the Bragg reflections corresponding to the β phase are clearly visible [141, 142]. Note that the 6T β (6 0 0) reflection is found at the identical q_z value as the C_{60} (1 1 1) reflection [170]. However, since the mixture contains significantly more 6T, and in the other mixtures with a higher amount of C_{60} this feature is not as well pronounced, it is very likely that this peak can be assigned to the 6T β-phase. A slight distortion of the 6T β (4 0 0) peak and a small hump at the position of the (12 0 0) peak of the LT-phase, indicate that there are still small fractions of the LT-phase within the film. With increasing fraction of C_{60} in the mixtures the crystallinity of 6T decreases further. For both the 6T:C_{60} (1 : 1) 303 K and the 6T:C_{60} (1 : 3) 303 K, the (2 0 0), (4 0 0) and (6 0 0) Bragg peaks of the β-phase are very weak. There are

no more indications for any well ordered out-of-plane crystallites of the LT-phase in these mixtures. The Kiessig oscillations in a q_z range up to around 0.2 Å^{-1} stem from interferences from scattering from the top of the film surface and the surface of the substrate [120, 124]. These oscillations are damped out with an increasing roughness of the films [120]. At 303 K, especially the non-equimolar mixtures exhibit very well pronounced oscillations, indicating very smooth films. This might be explained by C_{60} filling the voids between the 6T domains or vice versa, similar to results of perfluoropentacene deposited on diindenoperylene or pentacene on perfluoropentacene, where a small step edge barrier leads to a smoothing of the bottom layer when an overlayer is deposited on top [96].

The films prepared at a substrate temperature of 373 K (Fig. 8.2b) show all, with the exception of pure C_{60}, a higher crystallinity compared to the ones prepared at 303 K. In contrast to the low temperature films, for all films the 6T LT-phase dominates over the 6T β-phase. Well pronounced Bragg peaks corresponding to the LT-phase are clearly visible up to approximately $q_z = 1.7$ Å^{-1}. By fitting the (1 2 0 0) and (1 0 0 0) and using Scherrer's equation ($D_{coh} = 2\pi K/fwhm$, with $K = 0.94$ for spherical crystallites, and $fwhm$ being the full-width at half maximum of the fitted peaks) to estimate the coherently scattering crystal size $D_{coh||}$ [127], one obtains values ~ 20 nm corresponding very well to the nominal film thickness. This indicates the presence of crystals with an extension over the whole film thickness. In contrast to the low temperature films almost no Bragg reflections arising from the β-phase are visible. Only the 6T:C_{60} (3 : 1) 373 K mixture shows the first four orders of the Bragg peaks of the β-phase. For all the films no Kiessig oscillations are observable indicating that the surface roughness is significantly larger than in the low temperature films.

8.3.2 Grazing Incidence Diffraction

GIXD measurements were performed to identify and characterize the in-plane crystalline structure of the films. For a substrate temperature of 303 K the data are plotted in Fig. 8.2c. The peaks of all films can be clearly attributed to either 6T or C_{60}. Together with the XRR data (Fig. 8.2a) we conclude that the two materials do not form a new crystal structure. The Bragg peaks of the pure materials within the mixtures indicate that there are separated domains of the pure materials. Obviously, since the peaks of the mixtures are not as pronounced as the ones of the pure material, it is very likely that not all molecules organise in crystalline domains but some molecules form volumes of statistical intermixing. The GIXD data of the pure 6T 303 K is dominated by β-phase domains. The data of pure C_{60} exhibit only reflections belonging to the C_{60} fcc structure [170]. Furthermore, 2d-area images of the scattering patterns (Fig. B.1, Appendix B) show well-defined rings with constant q-values indicating a polycrystalline structure of this film.
The GIXD data of the mixtures are dominated by features of 6T (Fig. 8.2c and

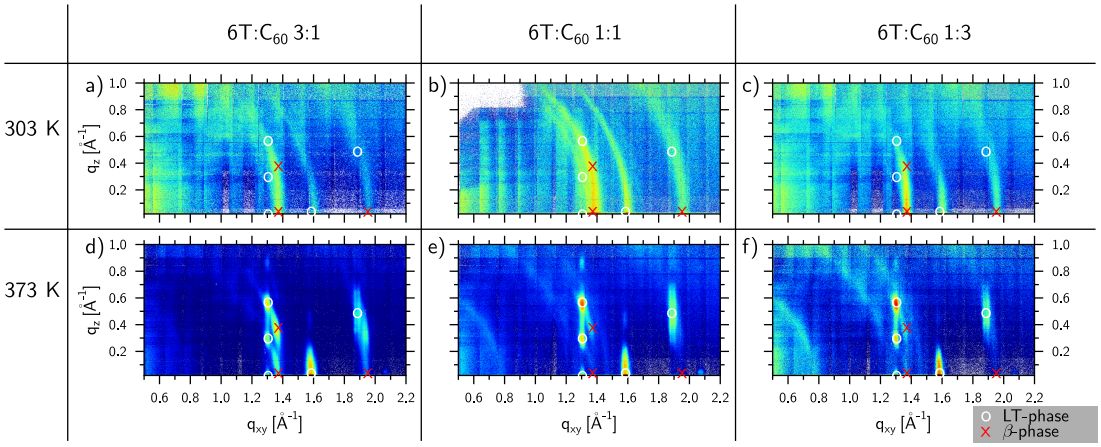

Figure 8.3: 2d reciprocal space maps of six different 6T:C_{60} mixtures. In the mixtures prepared at low substrate temperatures (a-c, top row) the peaks of 6T are smeared out and not very well defined. The rings usually seen for C_{60} (Fig. B.1) are not observed, since their signal is rather low. In the mixtures prepared at high substrate temperature (d-f, bottom row) the 6T peaks are relatively well defined. In the 6T:C_{60} (1 : 1) and (1 : 3) mixtures (e and f, respectively), weak rings arising from the C_{60} are visible. The images were taken with a MaxiPix area detector and composed of 147 single pictures using the *BINoculars* software [218, 219].

Fig. 8.3 a-c). With increasing amount of C_{60} all 6T peaks become broader, indicating that $D_{coh||}$ decrease. In the 2d GIXD data of the 303 K mixtures (Fig. 8.3a-c) all diffraction peaks are smeared out relatively strongly, indicating no well-defined domains. Overall, no reflections stemming from C_{60} can be observed.
The GIXD data of the films prepared at 373 K differ significantly from the data of the 303 K films. In general, all peaks arising from 6T (independent of the mixing ratio and the crystal structure) are shifted slightly to lower q-values. We reported the same effect for pure 6T already [83]. This shift might be explained by slightly distorted, more upright standing molecules forming a slightly expanded unit cell. In the pure 6T film the structure is dominated by the LT-phase with small fractions of the β-phase present in the film. The relative amount of β-phase in 6T is decreasing with larger C_{60} fraction. The reciprocal space maps of the high temperature mixtures (Fig. 8.3d-f) show well-defined 6T peaks. For 6T:C_{60} (1 : 1) and (1 : 3) weak rings stemming from C_{60} are visible, indicating that the C_{60} crystallites are randomly oriented, like in the pure C_{60} film.

8.3.3 Real-time Grazing Incidence Diffraction

We performed real-time GIXD measurements to follow and characterize the film growth *in situ*. For the 373 K mixtures the results are shown in Fig. 8.4. These experiments allow us to determine the thicknesses (estimated from the growth time and the measured QCM rate) at which the first domains of a certain crystal

Table 8.1: Parameters of the 6T:C_{60} mixtures.

	Ratio		t_{domain} [nm]	t_{phase} [nm]	$D_{coh\|\|}$[nm]		
T [K]	6T	C_{60}			6T (0 1 1) LT	6T β	C_{60} (1 1 1)
303	1	0	n.a.	n.a.	15.9	14.9	n.a.
303	3	1	1.0	n.a.	14.0	11.6	n.a.
303	1	1	1.4	n.a.	n.a.	6.6	n.a.
303	1	3	1.3	n.a.	n.a.	8.4.	n.a.
303	0	1	n.a.	n.a.	n.a.	n.a.	9.3
373	1	0	n.a.	n.a.	18.3	16.8	n.a.
373	3	1	1.2	4.5	18.2	12.2	n.a.
373	1	1	0.6	4.0	16.1	15.8	11.9
373	1	3	0.5	4.5	16.1	7.0	6.1
303	0	1	n.a.	n.a.	n.a.	n.a.	10.4

T is the substrate temperature during the growth. t_{domain} is the thickness from which on Bragg peaks of 6T (β- or LT-phase) are clearly visible. t_{phase} is the thickness at which the intensity of the β-phase starts to decrease and hence the transformation into the LT-phase starts. t_{domain} and t_{phase} are extracted from the real-time GIXD data. $D_{coh||}$ is the coherently scattering in-plane domain sizes of the 6T (0 1 1) LT peak, the 6T-β peak at $\sim 1.38\,\text{Å}^{-1}$ and the C_{60} (1 1 1) reflection. n.a. indicates that the corresponding reflections were not observed.

structure are forming. These values are summarized in Table 8.1 in the column t_{domain}. Since each real-time scan took around 260 seconds the values listed are upper limits and the domain formation may start earlier. The thickness at which the formation of phase separation starts can be seen as indicator if the phase separation is kinetically limited, as reported for diindenoperylene:C_{60} mixtures [106].

For 6T:C_{60}, there is only a small difference between the 303 K and 373 K films. For the 303 K films the thickness at which the formation of separated 6T domains starts is 1.0-1.4 nm and for the 373 K 0.5-1.2 nm. These thicknesses are lower than the van-der-Waals length of a single 6T molecule (~ 2.6 nm) [90, 143]. Together with the observation that almost only domains with a standing-up configuration are formed, we conclude that already in the first monolayer crystal domains are formed and therefore the phase separation between 6T and C_{60} begins and seems to be not kinetically limited for the investigated preparation conditions.

For the 373 K mixtures one observes that the peak corresponding to the β-phase first increases and, after a certain film thickness, starts to decrease. Together with this decrease, the intensity of the 6T (0 1 1) LT peak starts to increase. From the simultaneous occurrence of the two effects, we conclude that there is a transformation of already existing domains of the β-phase into domains of the

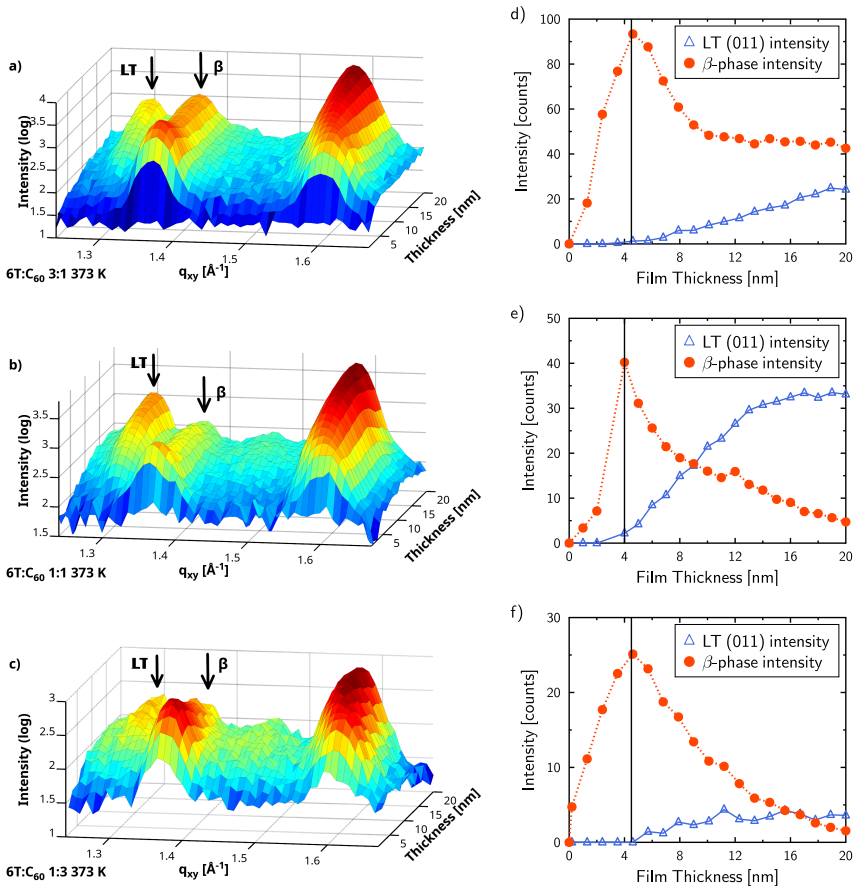

Figure 8.4: Real-time GIXD scans measured during film growth at 373 K. a) 6T:C_{60} (3 : 1) mixture. b) 6T:C_{60} (1 : 1) mixture and c) 6T:C_6 (1 : 3) mixture. d)-f) Show the evaluation of the intensities of the Bragg peaks corresponding to the LT (0 1 1) reflection and the β-phase reflection at $q_{xy} = 1.38\,\text{Å}^{-1}$ for the different mixing ratios presented on the left hand side.

LT-phase. The thicknesses at which this effect starts is also listed in Table 8.1 in the column named t_{phase}. This effect occurs, independently of the mixing ratio, at a total film thickness of approximately 4 nm, which corresponds to the second monolayer of 6T.

8.3.4 Annealing of 1:1 Mixtures and Pure 6T

A common method to improve the film quality after growth is to anneal the film. The 6T:C_{60} (1 : 1) 303 K film was heated linearly from 303 K to 373 K within 20 minutes. This temperature was kept for 20 minutes, followed by a further linear increase to 393 K. The final temperature was kept for 120 minutes. Fig. 8.5a and b depict the XRR and GIXD data of the film before and after annealing, respectively. The data of the mixture prepared at 373 K

are plotted as a reference. The out-of-plane data (Fig. 8.5a) indicates that the intensity of peaks corresponding to the β-phase decreases slightly while heating. Similar results are obtained from the GIXD data (Fig. 8.5b). Also here, features from the β-phase are less pronounced after the annealing steps. However, no significant change in the crystallinity of the films is observed after the annealing. Similar to the mixture, the 303 K pure 6T film was heated from 303 K to 373 K.

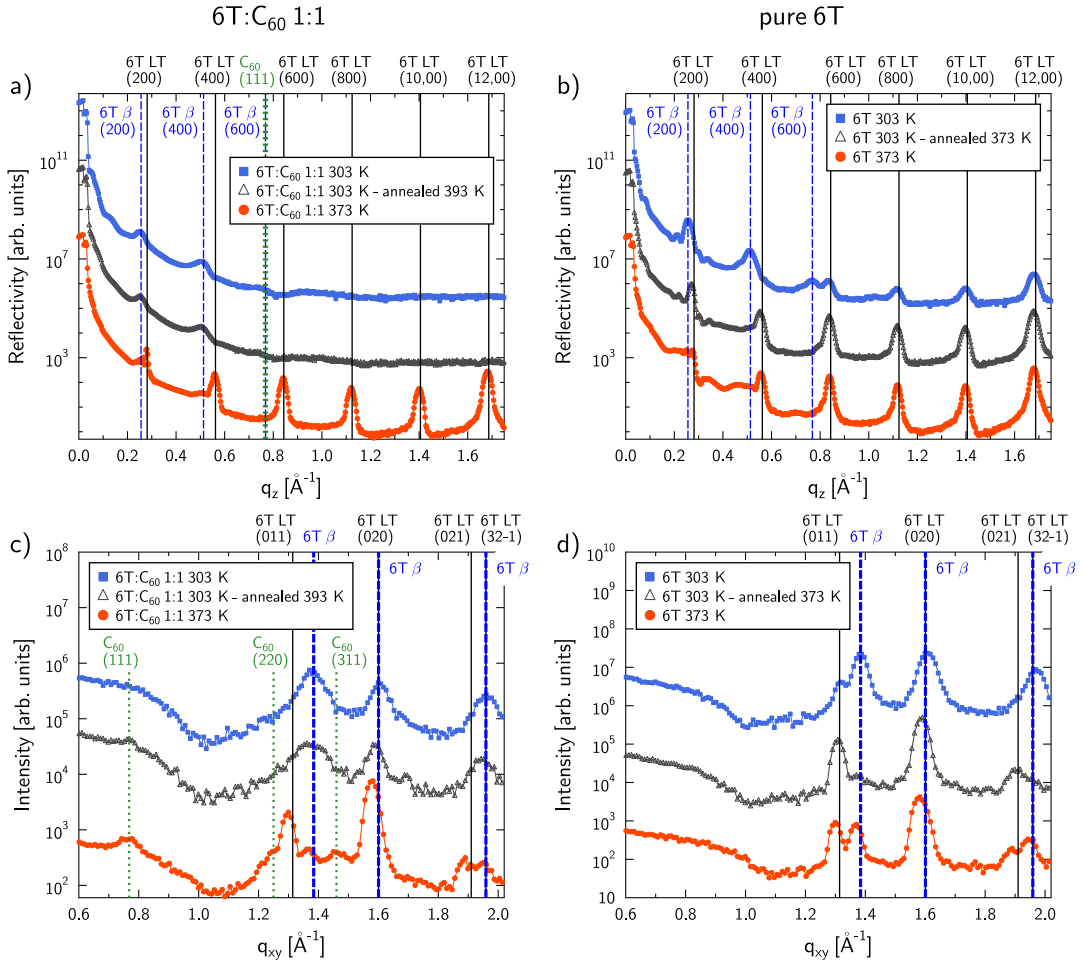

Figure 8.5: a) XRR and c) GIXD data of a 6T:C_{60} (1 : 1) film grown at a substrate temperature of 303 K (blue filled squares), the same film annealed at 393 K (black open triangles) and a film prepared directly at a substrate temperature of 373 K, respectively. b) XRR and d) GIXD data of a 6T film grown at a substrate temperature of 303 K (blue filled squares), the same film annealed at 373 K (black open triangles) and a film prepared directly at a substrate temperature of 373 K, respectively.

This increase took 20 min. Fig. 8.6 shows real-time GIXD scans during the annealing procedure. The exact annealing settings and times were as follows: Scan number 1 corresponds to the film just before the start of the annealing process. The time-span between scan number 1 and 2 are 20 minutes in which

the temperature was increased linearly from 303 K to 373 K. From scan number 2 to 7, the time between each scan is 5 minutes in which the temperature was kept constant at 373 K. Scan number 8 corresponds to the scan after annealing. The gap between scan 7 and scan 8 is approximately 50 minutes, needed for an additional post-growth characterization. Already while heating the substrate

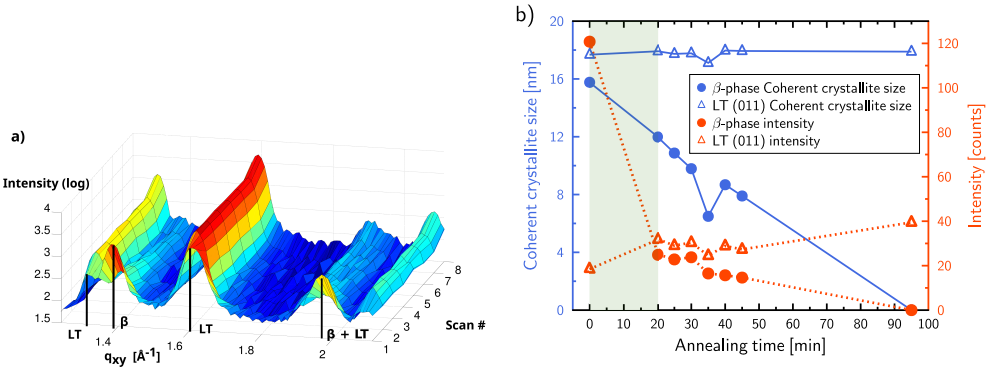

Figure 8.6: a) Real-time GIXD scans during the annealing of the pure 6T 303 K film. The time differences between the scan numbers was not constant. A detailed description of the time-steps and temperatures is given in the text. b) Evolution of the β- and LT-phase during the annealing process as a function of time. The light blue shaded area highlights the timespan during which the heating from 303 K to 373 K took place. The filled dots and open triangles represent the β- and the LT-phase, respectively. For the β-phase the peak at $q_{xy} = 1.38\,\text{Å}^{-1}$ and for the LT-phase the (0 1 1)-peak ($q_{xy} = 1.31\,\text{Å}^{-1}$) were considered. The blue solid line relates $D_{coh||}$ to the left y-axis, and the red dashed line relates the intensity to the right y-axis. Note that the 0 values for the β-phase indicate that the peak vanished completely. The theoretical resolution limit of the setup at the LT (0 1 1) peak position is 18.7 nm, which is very close the measured result. Hence, $D_{coh||}$ of the LT (0 1 1) might be larger.

from 303 K to 373 K the intensity of the peak at $q_{xy} = 1.38\,\text{Å}^{-1}$, corresponding to the β-phase, decreased significantly. At the same time the 6T LT (0 1 1) and the 6T LT (0 2 0) peaks evolve remarkably. This indicates a transformation from β-phase crystallites into LT-phase crystallites, which are energetically more stable but the formation is kinetically limited during the growth at low substrate temperatures. This evolution continues throughout the real-time measurements during the annealing. The peaks of the single scans were fitted with Pseudo-Voigt functions and $D_{coh||}$ (described above) and the intensity (area under the curve) of the different peaks were extracted. Fig. 8.6b depicts the data as a function of time. $D_{coh||}$ of the β-peak (solid blue lines with filled blue dots) is decreasing linearly with time. After 95 minutes the β-phase peak vanishes completely. $D_{coh||}$ of the LT (0 1 1)-peak is not changing during the annealing process. However, since the resolution limit of the setup is with 18.7 nm very close to the measured result. $D_{coh||}$ of the LT-phase might be larger. The

intensity of this peak is increasing over time, indicating a transformation of the β-phase into the LT-phase.
In Fig. 8.5b and d the XRR and GIXD data, respectively, of the pure 6T film before and after the annealing procedure, as well as data of a film prepared at a substrate temperature of 373 K, are shown. By comparing the XRR data before and after annealing, one notices immediately an enhancement of the out-of-plane crystallinity together with the transition of domains from the β to the LT-phase. Even more remarkable is the comparison of the annealed film with the one prepared at elevated temperature. In the XRR data of the annealed film, the β-phase ((2 0 0) and (4 0 0) peaks) are less pronounced than in the one prepared at 373 K. This is in agreement with the GIXD data of the films (Fig. 8.5d). Again, the peaks corresponding to the β-phase vanish almost completely upon annealing. As mentioned earlier, the 6T LT-phase and β-phase unit cells can be slightly modified. In contrast to the film prepared at 373 K, this effect is less pronounced for the annealed films. This is visible in Fig. 8.5d where the peaks of the LT-phase in the annealed film are less shifted compared to the ones observable for the film prepared at 373 K.

8.4 Discussion

The post-growth X-ray diffraction measurements for the 6T:C_{60} mixtures reveal interesting results. In general, C_{60} is not well ordered in any mixture investigated here. This is surprising, since in other mixed systems of C_{60} and the rod-like molecule diindenoperylene, the C_{60} forms relatively well-ordered domains [106]. In general, the kinetic energies which the molecules have after reaching the substrate play a very important role for the growth [22, 38]. This kinetic energy might be distributed and shifted between the molecules in the film and help to form different structures. Furthermore, outside influences, like optical heating can influence the growth of 6T [220].
6T in the mixtures seems to grow very similar to the pure films. However, the C_{60} influences the growth scenario in a way that always the dominant 6T phase is still more promoted. This means that at 303 K substrate temperature the mixtures show less features corresponding to the LT-phase with increasing amount of C_{60} compared to pure 6T (Fig. 8.7a and c). At 373 K, the picture is quite different. Here, the mixtures exhibit more features of the LT-phase and the β-phase is suppressed. For the 373 K films, C_{60} seems to support the nucleation of the stable 6T LT-phase (Fig. 8.7e). On the other hand, at 303 K the C_{60} seems to block the process of 6T reaching the energetically stable LT phase and locks the 6T in the kinetically favoured β-phase. The thermal energy from the substrate which is needed to overcome the activation energy for the transition to the LT-phase is partially available in the pure 6T 303 K film. However, in the 303 K mixtures

the transfer of this thermal energy might be hindered by the C_{60} molecules and hence the transition of the 6T domains from the β to the LT-phase is suppressed. From the real-time measurements during growth, we have seen that the growth scenario for all mixing ratios at 373 K is very similar. Already in the first monolayer (the first 2 nm) of the film growth, 6T starts to form coherently scattering domains. At the beginning, these domains consist mainly of the β-phase. After a certain thickness, a transformation from the β-phase to the LT-phase takes place. Interestingly, this transformations starts during the second monolayer of 6T. A similar transformation is not observed for the pure 6T. There, at a substrate temperature of 373 K the β-phase continues to nucleate throughout the whole growth process, although slower than the LT-phase after a certain critical film thickness (around 7 nm) [83]. This supports the idea that the C_{60} supports the 6T to nucleate in the more stable LT-phase, which is not possible in the pure material, since the β-phase domains are attached to the substrate and hence locked in this phase.
The annealing experiments on pure 6T and 6T:C_{60} (1 : 1) mixtures revealed further influence of C_{60} in the mixture. For the pure 6T, the additional thermal energy put into the system via the annealing process leads to nucleation of 6T in the energetically stable LT-phase (Fig. 8.7a and b). With enough annealing time almost all β-phase domains can be transformed into the LT-phase. This leads to films consisting almost purely of the LT-phase. A similar effect is reported for H_2-Phthalocyanines (H_2-Pc) where a metastable α-phase (dominant for deposition at room temperature) is transformed into a more stable and more compact β-phase upon annealing [221–223]. For 6T films prepared at 373 K, there are still fractions of the β-phase observed. For the presence of the β-phase the kinetics of the film formation process seem to play an important role. The β-phase domains tend to be more stable when formed at high substrate temperature together with (slightly distorted) LT-phase domains since they are found in the films prepared at 373 K but not in the annealed ones. This consideration is substantiated by the fact that for the 373 K film annealing was performed to some extent by keeping the substrate at 373 K while performing the post-growth measurements, which did not lead to a transformation of the β-phase into the LT-phase.
For the annealing of 6T:C_{60} (1 : 1), the result is significantly different. Here, no transformation of the β-phase to the LT-phase is observed (Fig. 8.7c and d). Possible explanations are that either the C_{60} could fill the voids between the 6T domains and act as kinetic traps, hindering the formation of the LT-phase, or that LT crystallites, which act as nucleation points, are necessary. The latter are found in pure 6T films, but not in the mixtures prepared at 303 K. This finding is similar for mixtures of pentacene (PEN) and C_{60} on nSiO for which no changes were observed upon annealing [203]. However, for the same system when a thin PEN templating layer, which usually improves the C_{60} crystallinity, is employed, an improvement of the C_{60} structure upon annealing but no changes of the PEN micro structure have been reported [203].

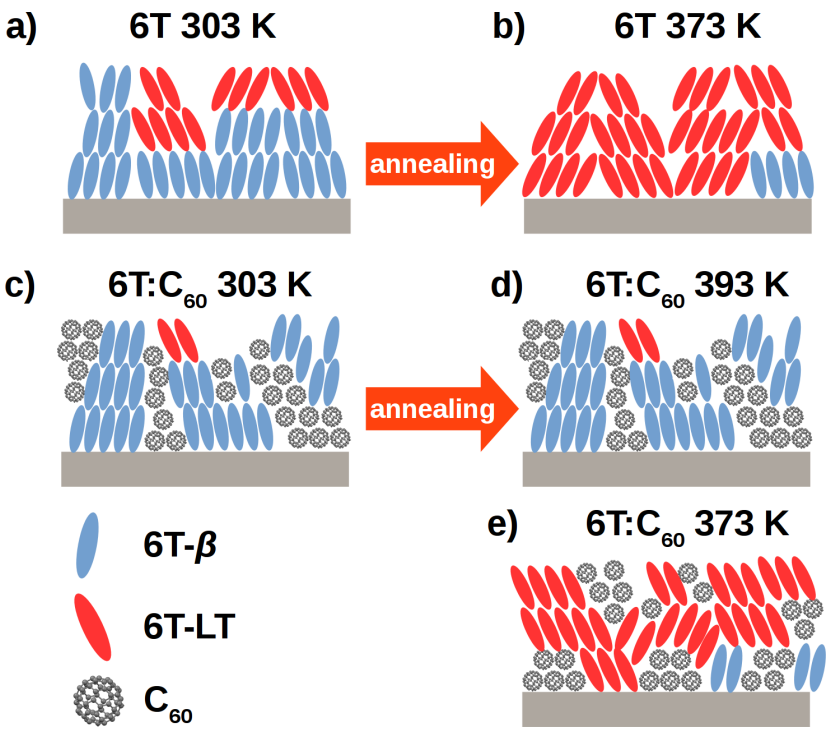

Figure 8.7: Schematic of the different scenarios reported. a) Pure 6T prepared at 303 K with the β-phase dominant close to the substrate and some LT-domains in the late state of growth. b) The annealed pure 6T film in which most of the β-domains have been transformed to the LT-phase. c) 6T:C_{60} 1:1 mixture prepared at 303 K, in which the fraction of β-phase domains is higher than in the pure 6T film. d) The 6T:C_{60} 1:1 mixture annealed to 393 K with no changes compared to the film as grown. e) The 6T:C_{60} 1:1 mixture prepared at 373 K with the LT-phase dominating the structure.

8.5 Conclusion

We investigated mixed thin films of 6T:C_{60} with nominal mixing ratios of 3:1, 1:1 and 1:3, prepared at 303 K and 373 K substrate temperature using real-time *in situ* X-ray techniques. We observed significant differences in the crystallinity of the films prepared at the different substrate temperatures. The mixtures deposited at 303 K show overall a less pronounced crystallinity and the films are dominated by the kinetically favoured β-crystal phase of 6T. In contrast, the films prepared at 373 K show a high crystallinity, consisting almost completely of standing-up crystallites of the 6T LT-phase, which is energetically more stable but kinetically suppressed. We believe that C_{60} influences the film growth since the thermal energy transfer between the molecules and the substrate and the energetic landscape are different upon the presence of C_{60} molecules.
Furthermore, the annealing of pure 6T revealed astonishing changes in the film structure. The annealed films showed only features of the LT-phase and no indications of the β-phase were found, whereas pure 6T films prepared and measured at the same substrate temperature as the annealing temperature (373 K) still showed features of the β-phase. Obviously, the kinetics of the film formation process play an important role and the domains of the β-phase seem to be more robust when prepared at elevated substrate temperature. Annealing of 6T:C_{60} (1 : 1) films did not show any drastic changes of the film structure and by no means any improvement of it. This can be attributed also to the influence of C_{60}. On the one hand, the presence of C_{60}, filling the voids in between the 6T crystallites, might block the movement of the 6T molecules prohibiting a transformation of the crystal structure. On the other hand, in the films prepared at 303 K the 6T LT-phase is suppressed due to the influence of the C_{60} and domains of the 6T LT-phase might be needed as nucleation point for the transformation from the β-phase into the LT-phase.
This behavior shows strongly that post-growth annealing of mixtures has a much weaker influence on the film structure compared to the growth on a heated substrate. After growth the energy barrier for crystallites might be too high to be thermally overcome before the desorption point is reached.

Chapter 9

Tailoring the Length Scale of Phase Separation in Diindenoperylene:C_{60} Mixtures

The results presented in this chapter are published in Ref. [224][1].

9.1 Introduction

Thin-film growth is fundamentally a non-equilibrium process since achieving equilibrium is permanently disturbed by incoming material and energy [189, 225]. Even for growth of single-compound films small changes in the preparation conditions, such as deposition rate, substrate temperature or substrate-adsorbate interaction, can lead to significantly different film structures and morphologies [37]. For mixtures of two (or more) compounds the picture is even more complex. There are at least three idealised cases of how two materials may intermix: a) solid solution – a stochastic mix of the two materials forms, b) ordered complex – two materials show a mixed phase with periodic long-range order, and c) phase separation – two ingredients tend to form separated domains of their pristine phases. The resulting mixing scenario depends on several parameters – *inter alia* the interaction energies between the different species, on the sterical compatibility in the case of molecules, but also on the preparation conditions like substrate temperature (T_{sub}) and/or deposition rate (r_{dep}) [38,62,86,104,226].
Mixtures of two organic compounds are often used in organic electronics, especially in organic photovoltaic (OPV) cells. Regarding the efficiency of the latter it has been demonstrated that the length-scale of phase separation (l_s) of the electron donating and electron accepting material is crucially important, partic-

[1] C. Lorch, H. Frank, R. Banerjee, A. Hinderhofer, A. Gerlach, G. Li Destri and F. Schreiber, Appl. Phys. Lett. **107**, 201903, (2015): *Controlling Length Scales of the Phase Separation to Optimize Organic Semiconductor Blends.*

ularly in comparison to the length-scales of the electronic processes (*i.e.* exciton diffusion length) of the system [30]. On the one hand, if l_s is too small, free charge carriers might be trapped and their extraction hindered. On the other hand, if l_s is too large, excitons might not reach the donor-acceptor interface, which is necessary for the charge separation. If l_s is even larger, electrical short circuits may occur. From these considerations one can conclude that the efficiency of OPV cells peaks for a certain l_s. This work is devoted to different ways of tailoring l_s, which can lead to improved efficiency of OPV cells.

OPV cells comprising the donor-acceptor combination of diindenoperylene (DIP)

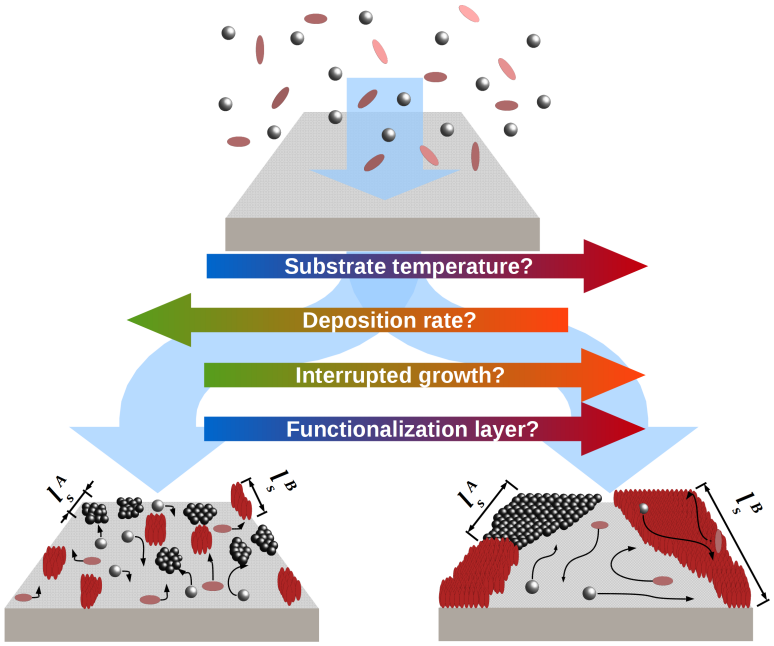

Figure 9.1: Schematic of kinetically limited phase separation in a molecular mixture with length-scales of phase separation (l_s) for both materials A (l_s^A) and B (l_s^B). A high (low) substrate temperature, a low (high) deposition rate, interrupted (continuous) growth or a functionalization layer (bare substrate) can be used to increase (decrease) the length-scale of phase separation.

and buckminster fullerene (C_{60}) have been reported to have excellent values for the solar cell parameters, in particular an extraordinarily high fill factor [26]. Furthermore, kinetically-limited delayed phase separation has been reported to occur, keeping in mind the sterical incompatibility of the molecules [106]. DIP itself has a high exciton diffusion length [227], exhibits ambipolar transport properties [29], and its structural and morphological properties have been extensively studied [79,135,178,186,213]. C_{60} is a commonly used acceptor material in OPV cells [13,228,229]. The two materials together form a prototypical system of phase separating mixtures, this offers the opportunity for a detailed understanding of

the fundamental aspects of such material pairs, in general. In bilayer geometry, where C_{60} is prepared on top of DIP, a strong templating effect of the DIP, which improves its crystal structure significantly, has been reported [176].
Here we compare different routes to engineer the length-scale of the phase separation in DIP:C_{60} mixed thin films prepared via organic molecular beam deposition. Fig. 9.1 depicts the various control parameters, which can be used for tailoring the phase separation length-scale (l_s). In the conventional approach, the growth mainly depends on the ratio of the diffusion rate of the molecules $D(T)$ to the incoming flux of molecules (*i.e.* the deposition rate r_{dep}) [225]. However, further methods can be used, such as a time-dependent deposition rate, as in interrupted growth, or surface functionalization. The bottom left-hand-side of Fig. 9.1 depicts low $D(T)$ and a high flux of incoming molecules, leading to a short length-scale when phase separating, whereas on the bottom right-hand-side relatively high $D(T)$ and a small effective incoming flux lead to relatively large domains and, hence, a larger length-scale of phase separation. We studied systematically the influence of all of the experimental parameters described above; the details of which are listed further below.
The films were characterised by *in situ* X-ray diffraction experiments, namely X-ray reflectivity (XRR) and grazing incidence X-ray diffraction (GIXD). The roughness was extracted from the XRR data and GIXD provided the averaged coherently-scattering in-plane domain size $D_{coh\parallel}$, which is used as a gauge for the phase separation length-scale l_s.

9.2 Experimental

Sublimation-grade DIP was obtained from the University of Stuttgart and C_{60} was purchased from Creaphys. The organic films were prepared via organic molecular beam deposition and investigated directly in a portable ultra-high vacuum chamber [137]. Native silicon oxide (nSiO) (oxide layer thickness $\sim 2\,\mathrm{nm}$) was used as a substrate. The pressure in the vacuum chamber was less than $2\cdot10^{-9}\,\mathrm{mbar}$ during the deposition. The preparation parameters were varied for different samples, including the substrate temperature T_{sub}, the deposition rate r_{dep} and the surface energy of the substrate by applying a thin organic (DIP or C_{60}) layer. The deposition rates were controlled with a quartz crystal microbalance (QCM), which was calibrated via XRR. The X-ray characterisation was performed at the ID10 beamline of the ESRF, with an energy of 14.0 keV (wavelength $\lambda = 0.886\,\text{Å}$). The critical angle of the samples at this energy was 0.13° and an incident angle of 0.1° was used for the GIXD scans. The XRR data were fitted using Parratt's formalism [123] with GenX [184] up to q_z-values of $0.2\,\text{Å}^{-1}$ for a quantitative analysis of the film roughness. The Bragg peaks of the GIXD data were fitted with Gaussian profiles, and Scherrer's formula was used to calculate the coherently-scattering in-plane domain size $D_{coh\parallel} = 2\pi\cdot0.94/fwhm$, where 0.94 is Scherrer's constant for

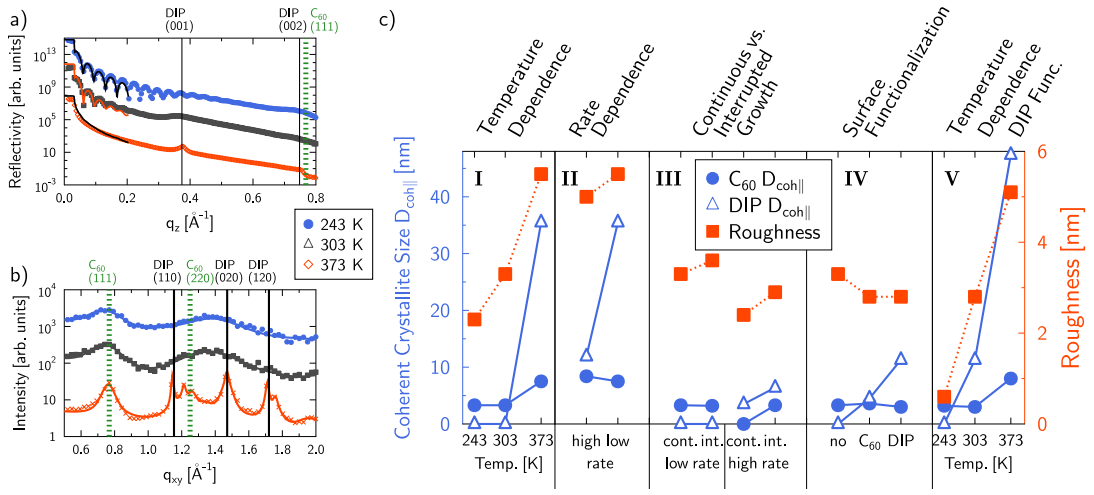

Figure 9.2: a) XRR data of DIP:C_{60} at different substrate temperatures. Solid lines are fits using Parratt's formalism. b) GIXD data of the same mixtures. Solid lines are fits to the data. c) Evolution of $D_{coh\parallel}$ and σ for different growth modifications. **I** Different substrate temperatures on bare nSiO. **II** Comparison for the high vs. low r_{dep} at $T_{sub} = 373\,\mathrm{K}$. **III** Normal vs. interrupted growth at low r_{dep} and high r_{dep} ($T_{sub} = 303\,\mathrm{K}$). **IV** Bare substrate vs. C_{60} and DIP functionalization layer at $T_{sub} = 303\,\mathrm{K}$. **V** Different substrate temperatures on DIP functionalization layer.

spherical-like particles and *fwhm* is the full-width at half-maximum of the fitted peak [127]. No broadening due to the experimental setup was included in the fit, hence the values reported here represent lower limits for $D_{coh\parallel}$.

9.3 Results

9.3.1 Methods for Tailoring the Length Scale of Phase Separation

The four different methods sketched in Fig. 9.1 were employed to tailor the length-scale of phase separation for DIP:C_{60} 1:1 mixtures. A nominal thickness of 20 nm was anticipated for all films. Table 9.1 lists the various parameters employed for the film growth. Three different T_{sub} (243 K, 303 K, 373 K) were studied to vary the diffusion length $D(T)$ of the molecules on the substrate. Furthermore, the deposition rate r_{dep} was varied. At low r_{dep} ($r_{dep}^{low} = 0.15\,\mathrm{nm/min}$) the probability that molecules can form a new domain before attaching to an existing one is much lower as compared to the high r_{dep} ($r_{dep}^{high} = 1.2 - 1.4\,\mathrm{nm/min}$). Another way to vary the growth is to interrupt the growth in a systematic manner [230]. We allowed different growth and interruption times for both the low and high rate. At r_{dep}^{low} we deposited for 400 s, which corresponds to depositing 1 nm followed by

a break of 120 s. This deposition-break cycle was repeated 20 times in total in order to reach a nominal film thickness of 20 nm. Molecules were evaporated for 75 s, followed by the flux being interrupted for 75 s, in the case of r_{dep}^{high}. The deposited material amounted to 1.5 nm per cycle. The procedure was repeated up to a total thickness of 20 nm. One additional method to change the diffusion length is to change the substrate potential by employing either a monolayer of DIP or a thin C_{60} layer before co-deposition of both materials. The resulting film architecture resembles a so-called planar mixed heterojunction, which, with the same material combination, has already been successfully employed for OPV devices [231].

9.3.2 Changing the Substrate Temperature

The XRR and GIXD data for the different T_{sub} are depicted in Fig. 9.2 a) and b), respectively.
Considering the out-of-plane data (Fig. 9.2 a)), all peaks can be associated either with standing-up DIP [186] or with the fcc C_{60} structural phase [171]. No additional peaks are observed, indicating that the materials phase separate and no new crystal structure is formed. In general, C_{60} crystallites on SiO_2 are oriented randomly with no preferred out-of-plane order [176]. With increasing substrate temperature the out-of-plane crystallinity of the DIP improves, evidenced by the enhanced DIP (0 0 1) and (0 0 2) Bragg peaks at $q_z = 0.37\,\text{Å}^{-1}$ and $q_z = 0.74\,\text{Å}^{-1}$. Another obvious trend is the increase of surface roughness (σ) with increasing substrate temperature, which can be concluded from the damping of the Kiessig oscillations in the low q_z region [124]. The extracted thicknesses and σ are summarized in Table 9.1. The evolution of σ from 2.3 nm to 5.5 nm with increasing temperature is depicted in Fig. 9.2 c).

The results of the GIXD measurements are shown in Fig. 9.2 b). As seen in the out-of-plane data as well, only Bragg peaks associated with either standing-up DIP or the fcc structure of C_{60} appear. Generally speaking, the crystallinity of the films increases with increasing T_{sub}, visible in the sharper Bragg reflections at higher T_{sub}. The values extracted from the GIXD data are listed in Table 9.1 and visualized in Fig. 9.2c **I**. At $T_{sub} = 243$ and 303 K only the C_{60} (1 1 1) peak can be distinguished clearly. The other Bragg peaks are buried under a wide hump in the $q_{xy} = 1.0 - 1.8\,\text{Å}^{-1}$ range, indicating that no large crystallites of any of the two materials are formed. Further increasing T_{sub} to 373 K, $D_{coh\|}$ of C_{60} and DIP increases from 3.3 to 7.5 nm and to 35.5 nm, respectively. Interestingly, at $T_{sub} = 373$ K two additional peaks at $q_{xy} = 1.21\,\text{Å}^{-1}$ and $1.76\,\text{Å}^{-1}$ are observed. These two peaks can be associated with domains of an ordered DIP polymorph, already observed in pure DIP films [179]. $D_{coh\|}$ of these two peaks are 23.5 nm and 16.8 nm, respectively. These peaks are not observed for any of the other films.

Table 9.1: Different deposition strategies for the preparation of DIP:C_{60} (1:1) mixtures investigated in this study. The preparation of the templating layers are described in the text. The evaporation rates marked with * are the rates employed during the open shutter for growth runs with non-continuous rate. The thicknesses d and roughnesses σ (error for both is ± 0.1 nm) were determined from XRR. The in-plane coherent crystal size $D_{coh\parallel}$ is averaged over several reflections and calculated via Scherrer's formula (error for each is ± 0.3 nm). The values in the bottom row (temp. DIP) correspond to the pure DIP template.

T_{sub} [K]	Template	r_{dep} [nm/min]	Int.	d [nm]	σ [nm]	$D_{coh\parallel}$ C_{60} [nm]	$D_{coh\parallel}$ DIP [nm]
243	no	0.15	no	18.3	2.3	3.3	n.a.
243	DIP	0.15	no	18.0	0.6	3.2	n.a.
303	no	0.15	no	17.9	3.3	3.3	n.a.
303	DIP	0.15	no	16.9	2.8	3.0	11.3
303	C_{60}	0.15	no	19.0	2.8	3.6	4.5
303	no	0.15*	400/120	19.2	3.6	3.2	n.a.
303	no	1.20	no	19.6	2.4	n.a.	3.5
303	no	1.20*	75/75	20.0	2.9	3.3	6.4
373	no	0.15	no	20.8	5.5	7.5	35.5
373	DIP	0.15	no	21.2	5.1	8.0	47.4
373	no	1.42	no	22.6	5.0	8.4	11.9
303	temp. DIP	0.15	n.a	n.a.	n.a.	n.a	6.9

9.3.3 Changing the Deposition Rate

The film prepared at 303 K with r_{dep}^{high} shows a slightly better out-of-plane crystal structure than the low-deposition-rate film. Additionally, this film is the one with the smallest surface roughness at $T_{sub} = 303$ K. In contrast to the out-of-plane data, the in-plane data of the high-rate film shows only weak peaks corresponding to DIP and no C_{60} features at all. The latter is quite surprising since all other films show at least a broad Bragg peak corresponding to the C_{60} (1 1 1) orientation. However, at $T_{sub} = 373$ K, increasing r_{dep} by one order of magnitude influences strongly the in-plane structure: $D_{coh\parallel}$ of DIP decreases from 35.5 nm to 11.9 nm. For C_{60}, $D_{coh\parallel}$ is slightly higher (from 7.5 nm to 8.4 nm) (Fig. 9.2c **II**). The latter might be due to small variations in the mixing ratio, which might vary slightly over the preparation process.

9.3.4 Time-Dependent Deposition Rate

There is basically no difference in the out-of-plane structure observed for the interrupted growth and the normal growth, at r_{dep}^{low}. Also, the in-plane structure is very similar in both cases (Fig. 9.2c **III**, left hand side). However, interrupted growth at r_{dep}^{high}, leads to a slightly better ordered film in the out-of-plane direction compared to the continuous growth with the same deposition rate. In addition, σ is slightly higher (2.4 nm vs. 2.9 nm) for the interrupted growth. The changes are more significant for the in-plane structure. Interrupting the growth causes $D_{coh\parallel}$ of DIP to increase to 6.4 nm (from 3.5 nm) and $D_{coh\parallel}$ of C_{60} to 3.3 nm, respectively, whereas the latter cannot be determined at r_{dep}^{high} without interruptions (Fig. 9.2c **III**, right hand side).

9.3.5 Functionalization of the Substrate

The DIP layer was employed at three different T_{sub} – 243 K, 303 K and 373 K – whereas that of C_{60} was used only at 303 K (Fig. 9.2c **V** and **IV**, respectively). For the DIP layers, σ is slightly smaller than the ones of films without a functionalization layer, at all T_{sub}. Coincidently, $D_{coh\parallel}$ of DIP is increased by employing a DIP layer to 11.3 nm at 303 K (where $D_{coh\parallel}$ cannot be determined without the DIP layer) and from 35.5 nm to 47.4 nm at $T_{sub} = 373$ K. $D_{coh\parallel}$ of C_{60} is not changing significantly upon employing a DIP functionalization layer, for the two higher T_{sub}. At $T_{sub} = 243$ K, $D_{coh\parallel}$ of DIP (cannot be determined) and C_{60} (3.3 nm), respectively, do not change when first depositing a pure DIP layer. For the C_{60} layer, the effect is similar. A small increase of $D_{coh\parallel}$ of DIP to 4.5 nm is observed and $D_{coh\parallel}$ of C_{60} is increased from 3.3 nm to 3.6 nm. Please note that $D_{coh\parallel}$ of the DIP monolayer is 6.9 nm and different from the values of the mixtures.

9.4 Discussion

The different preparation conditions reported within this study have a significant impact on the growth of the DIP:C_{60} mixtures. The strongest influence, within the studied parameter space, can be associated with the T_{sub} during the growth. A higher T_{sub} implies a higher diffusion energy of the molecules and this allows molecules to rearrange on the surface to an energetically favourable position, leading to a larger length-scale of phase separation l_s. Together with this, also a higher roughness σ is observed. Simultaneously, at a low T_{sub} the films show a very low crystallinity and, therefore, no real phase separation at all, yet, the films are relatively smooth. This indicates a positive correlation between l_s and σ of the films. However, it is not easy to conclude from a rougher surface a higher l_s directly since the differences in σ are relatively low compared to the differences

observed for l_s. Interestingly, no indications of lying-down DIP molecules or the low-temperature bulk crystal phase are observed at $T_{sub} = 243\,\mathrm{K}$, as is the case for pure DIP films at 233 K [178].
It is usually the case that either a high deposition rate or a low T_{sub} should have a similar effect on the phase separation. At $T_{sub} = 373\,\mathrm{K}$, the influence of decreasing r_{dep} by a factor of ten on $D_{coh\|}$ of DIP is of the same order as increasing T_{sub} from 303 K to 373 K. Nevertheless, decreasing the deposition rate at low substrate temperatures has a significantly smaller influence on l_s than increasing T_{sub}. However, higher deposition rates lead to a smoother film surface for the investigated T_{sub}.
Interrupting the growth periodically increases the average diffusion length on the surface. In the case of a relatively low deposition rate (0.15 nm/min) interrupting the growth seems to have no influence on the structure of the mixture. Nevertheless, the controlled interruption of the growth leads to actually higher crystallinity, in the case of a high deposition rate (1.2 nm/min). The growth conditions at r_{dep}^{low} and $T_{sub} = 303\,\mathrm{K}$ seem to be relatively close to equilibrium conditions, since the interruptions have no influence.
A DIP monolayer under the mixture has a strong templating effect on the film growth and improves mainly the DIP crystal structure, leading to a larger length-scale of phase separation at 303 K and 373 K. At 243 K, this effect is not observed. A C_{60} functionalization layer at $T_{sub} = 303\,\mathrm{K}$ does not show an effect as pronounced as for DIP, but it is observable. Employing a functionalization layer seems to decrease the interaction potential between the substrate and the molecules, resulting in a higher diffusion length of the molecules, and, therefore, in more phase separation. However, at low substrate temperatures the effect of the low $D(T)$ due to the low T_{sub} is outweighing the benefit of a favorable surface potential.
Using mixtures with l_s lower than the exciton diffusion lengths of the materials (for DIP and C_{60} 100 nm [227] and 40 nm [232], respectively, under ideal conditions), but still as large as possible should improve OPV cells. Our results are already close to the optimum; however, the methods presented in this work can be extended easily to increase l_s further for even better charge transport, as in the following: higher T_{sub} (with the desorption temperature as upper limit), lower r_{dep}, a specialized surface functionalization, or different preparation methods which are closer to thermal equilibrium, *e.g.* organic vapor phase deposition [233] or hot wall epitaxy [234].

9.5 Conclusion

Summarizing, we have shown all the important tools to tailor the length-scale of phase separation in organic semiconductor thin film blends. The strongest

impact observed was the substrate temperature. Also, the deposition rate as well as functionalization layers can be employed to gain a similar effect, especially in cases when the substrate temperature cannot be changed.

Chapter 10

Mixing of Non-Equimolar Diindenoperylene:C_{60} Blends

In this chapter, results of DIP:C_{60} non-equimolar mixtures are presented. The part on grazing incidence small angle X-ray scattering consists of samples prepared and measured by Rupak Banerjee, Jiri Novák, Christian Frank and Alexander Gerlach. The results presented in this chapter are part of Ref. [235][1].

10.1 Introduction

Within the study presented here, we investigated the influence of substrate temperature and mixing ratio on the kinetics of the phase separation of non-equimolar DIP:C_{60} mixtures. We performed various X-ray scattering techniques, namely X-ray reflectivity (XRR) and grazing incidence X-ray diffraction (GIXD) for probing the out-of-plane and in-plane film structure, respectively, as well as grazing incidence small angle X-ray scattering (GISAXS) to investigate the evolution of the surface morphology [120, 236]. For mixtures with an excess of DIP we observe an increase of the coherently scattering in-plane domain size $D_{coh\parallel}$ and the averaged island distance D_{island}. Furthermore, a near perfect layer-by-layer growth mode is observed for this mixing ratio. Contrary, for equimolar and C_{60} dominated mixtures the crystallinity of the films is significantly lower but also very smooth films are observed. The crystallinity of the pure phases as well as the length scale of phase separation increases with higher substrate temperatures.

[1] C. Lorch, J. Novák, R. Banerjee, S. Weimer, J. Dieterle, C. Frank, A. Hinderhofer, A. Gerlach, F. Carla, and F. Schreiber **in preparation** (2015): *Growth Behavior of Non-Equimolar Mixtures of Sterically Incompatible Organic Semiconductors.*

10.2 Experimental

DIP was obtained from the University of Stuttgart and purified twice via temperature gradient sublimation before use. C_{60} was purchased from Creaphys and used without further purification. The organic films were prepared and investigated during growth in a portable ultrahigh vacuum chamber [137]. Silicon covered with native silicon oxide (nSiO) was used as a substrate. The oxide layer thickness was approximately 2.7 nm. Before installation, the substrates were ultrasonically cleaned with acetone, isopropanol and purified water. Before each film deposition, the substrate was heated to 770 K. The pressure in the vacuum chamber was lower than 1×10^{-8} mbar during the deposition. Two series of samples were prepared. Series A consists of eight films with mixing ratios of DIP:C_{60} 1:1, 3:1 and 1:3 at substrate temperatures of 308 K, 338 K and 373 K (no 1:1 at 338 K). The total growth rate was between 0.17 and 0.22 nm/min. For this series, real-time GIXD measurements at the ID03 beamline of the ESRF were performed. The energy was set to 11.5 keV (corresponding to a wavelength of 1.08 Å). A MaxiPix area detector was employed and slits were put directly in front of the detector to mimic a point detector for real-time and postgrowth scans (XRR and wide-range GIXD). The XRR data were fitted using Parratt's formalism [123] implemented in the GenX software [184] (not shown) up to $q_z = 0.20$ Å^{-1} using a model consisting of one bilayer, representing the wetting layer (*i.e.* completely filled molecular layers, and partially filled molecular layers on top, which represent the wedding-cake like growth reported for DIP [79, 186]). The Bragg peaks in the GIXD data were fitted with Gaussians to obtain the full width at half maxima ($fwhm$) of the peaks and Scherrer's equation ($D_{coh\|} = 2\pi K/fwhm$, with $K = 0.94$ for spherical crystallites) was used to calculate $D_{coh\|}$ [127]. The instrumental broadening was not included, hence the estimated values are lower limits only.

Sample series B consists of six samples with DIP:C_{60} 3:1, 2:1, 1:1 and 1:3 mixtures and the pure materials at 303 K substrate temperature. Real-time *in situ* GISAXS measurements were performed at the X04SA beam-line of the Swiss Light Source [183] at a wavelength of 0.99987 Å. The incidence angle of the X-ray beam was fixed at α_i =0.848 °, which corresponds to the anti-Bragg point of DIP (0 0 1) out-of-plane reflection, and the scattered signal was detected using a PILATUS II two dimensional detector.

10.3 Results

10.3.1 X-Ray Reflectivity

For the sample series A, XRR measurements were performed to study the crystal structure perpendicular to the surface. Figure 10.1 depicts the data grouped for

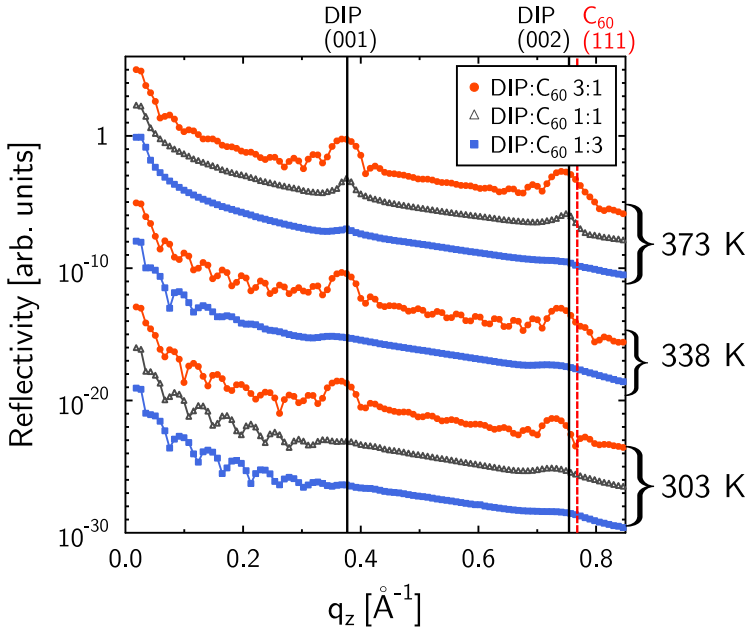

Figure 10.1: XRR data of sample series A. At substrate temperatures of 373 K (top), 338 K (middle) and 303 K (bottom) films with the mixing rations DIP:C_{60} 3:1 (red filled circles), 1:1 (black empty triangles) and 1:3 (blue filled squares) were measured. The vertical lines indicate the Bragg positions for pure DIP (solid black) and C_{60} (dashed red) thin films. The curves are vertically shifted for clarity.

the three different substrate temperatures 303 K, 338 K and 373 K. For plots presenting data measured at all three temperatures, always the DIP:C_{60} 3:1 mixture is shown at the top with red circles, followed by the 1:1 (black empty triangles) and 1:3 (blue filled squares) mixtures, respectively. The films prepared at 303 K show the most pronounced thickness oscillations in the low q_z regime (so called Kiessig oscillations, up to approximately $q_z = 0.3\,\text{Å}^{-1}$). These oscillations are a strong indication for films with a smooth top surface. With increasing substrate temperature these oscillations get more damped, due to higher surface roughness. The thickness and roughness extracted from fitting the data are summarized in Table 10.1.

The thicknesses of the films, extracted from the electron-density profiles differ significantly from each other. Therefore, comparing the absolute roughness value of the single films might be misleading. As a first qualitative impression, the films prepared at 303 K show the lowest surface roughness overall. The films with a substrate temperature of 338 K show a thickness-to-roughness ratio which is similar to the films on substrates at 303 K. For films prepared at 373 K, the roughness is higher than for 338 K and 303 K. The DIP:C_{60} 3:1 film shows the lowest roughness followed by the one with an excess of C_{60}, whereas, again the equimolar mixture is the roughest film.

Table 10.1: Summary of the film parameters extracted from the fitted XRR and GIXD data. The following values are listed: Substrate temperature T_{sub}, mixing ratio DIP:C_{60}, film thickness d , roughness σ, relative roughness σ/d , in-plane coherent crystallite size $D_{coh||}$ for DIP and C_{60}.

T_{sub} [K]	DIP:C_{60}	d [nm]	σ [nm]	σ/d	$D_{coh\|\|}$ [nm]	
					C_{60}	DIP
303	3:1	14.9 ±0.2	1.4 ±0.2	0.094 ±0.013	4.7 ±0.3	7.1 ±0.3
303	1:1	13.2 ±0.2	1.2 ±0.2	0.091 ±0.015	2.6 ±0.2	n.a.
303	1:3	11.8 ±0.2	1.2 ±0.2	0.102 ±0.017	4.1 ±0.3	n.a.
338	3:1	17.8 ±0.2	1.3 ±0.2	0.073 ±0.011	2.9 ±0.2	12.6 ±0.5
338	1:3	12.4 ±0.2	1.8 ±0.3	0.145 ±0.024	3.7 ±0.2	n.a.
373	3:1	16.0 ±0.3	2.5 ±0.3	0.156 ±0.019	5.7 ±0.4	20.5 ±0.9
373	1:1	16.3 ±0.5	4.1 ±0.4	0.252 ±0.026	7.6 ±0.5	23.4 ±0.9
373	1:3	16.5 ±0.5	2.5 ±0.5	0.152 ±0.025	6.8 ±0.5	20.1 ±0.9

The black and red dashed vertical lines in Fig. 10.1 mark the Bragg peak positions of pure DIP and C_{60}, respectively. All observed out-of-plane Bragg peaks can be clearly associated to one or the other compound. Since no other Bragg peaks are observed, it is obvious that the two materials form crystalline domains, consisting of pristine materials, and no new hybrid crystal phase is observed. For all three different substrate temperatures, in the DIP:C_{60} 3:1 mixtures (red circles) the Bragg peaks (first and second order) which can be ascribed to the standing-up domains of DIP, are clearly visible. For the same mixing ratio the C_{60} (1 1 1) Bragg peak is only a small hump on the high q_z side of the DIP (0 0 2) Bragg reflection. For the mixtures with an excess of C_{60}, independent of the substrate temperature, no well-defined Bragg peaks can be observed, only at 373 K DIP the (0 0 1) reflection is slightly visible. For an equimolar mixing ratio the substrate temperature has a relatively strong impact on the out-of-plane crystallinity. The DIP Bragg peaks get more pronounced with increasing substrate temperature. For all temperatures, the equimolar mixtures do not show any out-of-plane Bragg peaks corresponding to C_{60}. However, the out-of-plane coherent crystal size of the equimolar mixture at the highest temperature (373 K) is still smaller than the one of the DIP:C_{60} 3:1 mixture at 303 K.
Furthermore, the DIP Bragg peaks at 303 K and 338 K are slightly shifted to lower q_z values, compared to pure DIP films [19]. The first (second) DIP Bragg peak is observed at 0.363 $Å^{-1}$ (0.729 $Å^{-1}$) and 0.368 $Å^{-1}$ (0.737 $Å^{-1}$) for 303 K and 338 K, respectively. At 373 K the values are very close to the one reported (0.371 $Å^{-1}$ and 0.742 $Å^{-1}$). This shift corresponds to a decrease of the lattice vector perpendicular to the surface of 0.325 Å($\sim 2\,\%$) when the substrate temperature is increased from 303 K to 373 K and might be explained by DIP molecules

which are slightly more tilted either due to different interaction potentials of the surrounding molecules or due to different diffusion energies of the molecules at different substrate temperatures.

10.3.2 Grazing Incidence Diffraction

In addition to the XRR data, GIXD measurements were performed on the same samples. The data for the different mixing ratios prepared at different substrate temperatures are depicted in Fig. 10.2. The intensity of the different in-plane Bragg peaks increases with substrate temperature, as was also observed in the out-of-plane data. For the different mixing ratios, generally the Bragg peaks corresponding to the dominant material in the mixtures are more pronounced, at all three substrate temperatures. The calculated values are listed in Table 10.1 for the different substrate temperatures and mixing ratios.

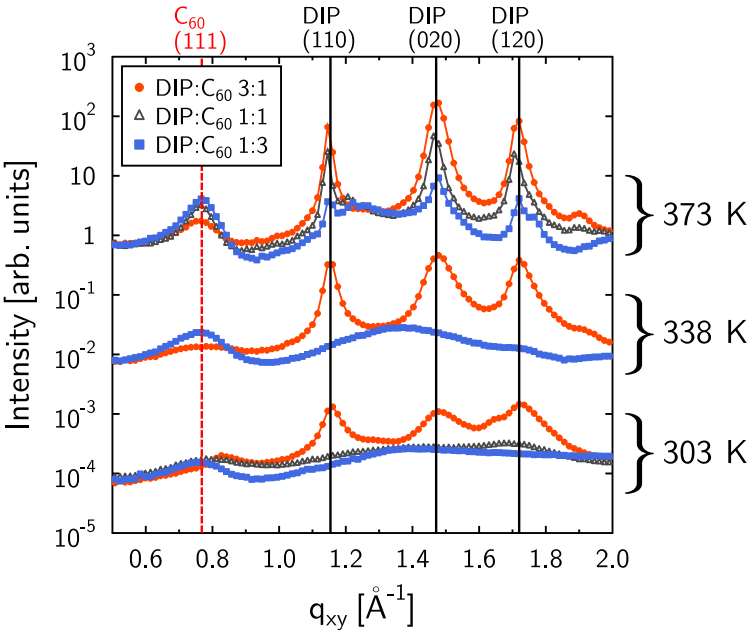

Figure 10.2: GIXD of DIP:C_{60} mixtures with different mixing ratios and prepared at different substrate temperatures.

At a substrate temperature of 303 K, the in-plane coherent crystallite size $D_{coh\|}$ is relatively small. For the equimolar mixing and the one with an excess of C_{60} only the C_{60} fcc (1 1 1) at $q_{xy} = 0.768\,\text{Å}^{-1}$ can be fitted. The other C_{60} and the DIP reflections are superimposed in a wide hump in the range $q_{xy} = 1.1-1.8\,\text{Å}^{-1}$. At 338 K the film with an excess of DIP shows well pronounced Bragg peaks, corresponding to DIP domains. On the other hand, in the mixture with more C_{60}, only the C_{60} (1 1 1) peak and a broad hump are visible. For a substrate temperature of 373 K, all three mixtures show well defined peaks. The size of the

coherently scattering domains for both, DIP and C_{60}, is almost independent of the mixing ratio. Only the relative intensities of the peaks change strongly with the mixing ratio as the intensity is proportional to the amount of material in the mixtures. From the data in Fig. 10.2 we can clearly see that with increasing substrate temperature both the crystallinity of the the pure phases as well as the degree of phase separation increases strongly. Similar to the growth of the pure materials on nSiO [79, 178, 198] C_{60} grows as a 3D powder, which we clearly see by observing C_{60} (1 1 1) reflections both in out-of-plane as well as in in-plane scans (Fig. 10.1 and Fig. 10.2, respectively), whereas DIP domains are textured with (0 0 1) planes parallel to the sample surface.

10.3.3 Real-Time Grazing Incidence Diffraction

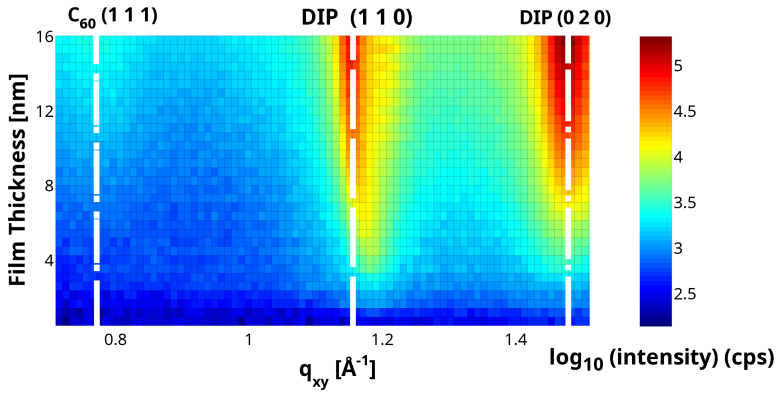

Figure 10.3: Real-time GIXD data of DIP:C_{60} 3:1 mixture prepared at 373 K. Film thickness is proportional to the growth time.

In order to investigate the evaluation of the mixing behavior during the film growth, real-time GIXD measurements were performed. The measurements allow us to determine the coherently scattering crystal-size ($D_{coh\|}$) dependent on the film thickness, during the actual growth. Figure 10.3 shows an exemplary dataset for the DIP:C_{60} 3:1 mixture at a substrate temperature of 373 K. The image shows mainly the evolution of the DIP (1 1 0) and (0 2 0) peaks. For the first 4 nm the peaks are not well defined, indicating that the coherently scattering domains form only after a certain film thickness, similar to the results already reported for lower substrate temperatures [106]. In the specific data shown in Fig. 10.3 the C_{60} peak is almost not visible, while the DIP peaks are dominant.

From the time evolution of the width of the Bragg peaks in the individual scans we calculate $D_{coh\|}$ as a function of film thickness, or equivalently growth time. For the 373 K mixtures, the $D_{coh\|}$ evolution is depicted in Fig. 10.4 and Fig. 10.5 shows the results of the DIP:C_{60} 3:1 mixtures prepared at the three different substrate temperatures.
An increase of $D_{coh\|}$, independent of the mixing ratio, is observed at 373 K (Fig.

10.4). As observed from the post-growth GIXD data (Fig. 10.2), the absolute values of $D_{coh\|}$ for the different mixing ratios are quite different. For the DIP:C_{60} 3:1 ratio $D_{coh\|}$ of the C_{60} cannot be determined. However, the increase of $D_{coh\|}$ of DIP is the most pronounced of all mixing ratios. We observe that there is a very fast increase of $D_{coh\|}$ at the beginning of growth. Later on $D_{coh\|}$ steadily increases during the entire film growth, to almost double its value in the thickness range from $2.5 - 16.0\,\text{nm}$. In contrast to this observation, for DIP:C_{60} 1:1 and 1:3 the increment in $D_{coh\|}$ as a function of thickness (for both DIP and C_{60}) is different. For these mixing ratios, also a fast increase upto a certain thickness ($\sim 5\,\text{nm}$ for 1:1 and $\sim 1\,\text{nm}$ for 1:3), followed by a rather slow increase of $D_{coh\|}$, is observed.

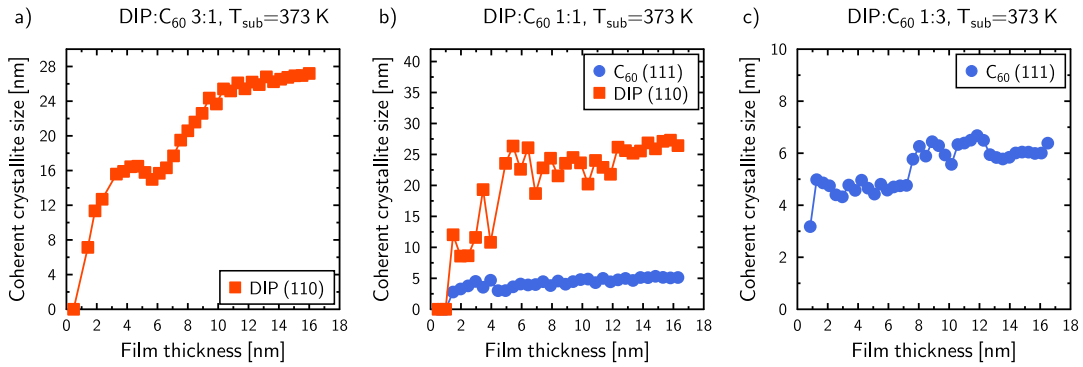

Figure 10.4: Evolution of $D_{coh\|}$ of DIP:C_{60} at 373 K with the mixing ratios a) 3:1, b) 1:1 and c) 1:3.

Next we focus on a comparison of the thickness dependence of $D_{coh\|}$ of DIP:C_{60} 3:1 mixtures grown at different substrate temperatures (Fig. 10.5). With increasing substrate temperature the sudden increase of $D_{coh\|}$ observed, appears at lower film thicknesses. In addition, the increase of $D_{coh\|}$ during the later stage of the film growth ($d > 5\,\text{nm}$) is steeper at higher substrate temperatures. However, the common observation for 3:1 mixtures at all substrate temperatures is that $D_{coh\|}$ is clearly increasing over the whole film growth. Note that the large $D_{coh\|}$ fluctuations at the beginning of the growth ($d < 5\,\text{nm}$) stem from fitting artefacts due to a weak signal at the initial stage of growth.

10.3.4 Real-Time Grazing Incidence Small-Angle Scattering

In order to characterize the evolution of the top-surface morphology of the mixtures, real-time GISAXS measurements were performed. A schematic of the

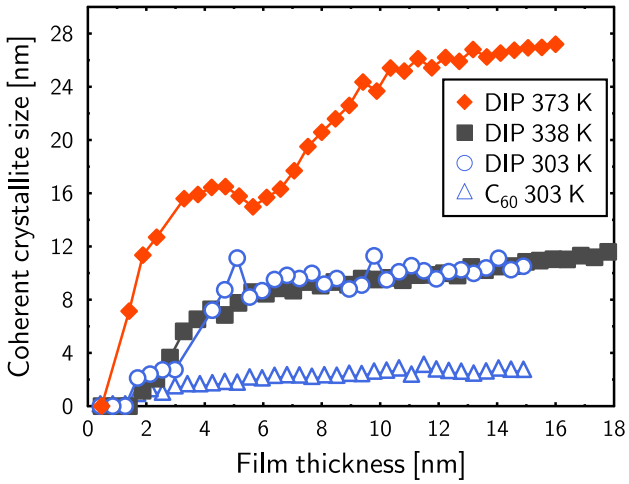

Figure 10.5: Evolution of $D_{coh\parallel}$ in DIP:C_{60} 3:1 mixtures at different substrate temperature.

typical GISAXS experimental set-up and a typical GISAXS profile are shown in Fig. 10.6. Data were extracted from three different regions indicated in the image: Firstly, the variation in intensity was monitored at the so-called anti-Bragg point of the DIP (0 0 1) peak, at $q_z = 0.185\,\text{Å}^{-1}$ [76], from which information on the growth mode, *i.e.* Frank-van der Merwe, Stranski-Krastanov or Volmer-Weber growth, can be extracted [63, 180, 237, 238]. Please note that the anti-Bragg condition corresponds to films of pure DIP, however incidentally, the same position almost coincides with the quarter-Bragg condition of C_{60} (1 1 1). Secondly, for each frame the intensity along q_z direction in the region comprising the Yoneda wing [136], *i.e.* the points in the reciprocal space map, where the exit angle equals the critical angle of the organic film (horizontal dashed line in Fig. 10.6), was integrated, resulting in intesity profiles along q_y. The peaks stemming from the correlation of island positions appearing in these profiles and also visible in the reciprocal space maps as regions of enhanced intensity centred along $q_y \approx \pm 0.1\,\text{nm}^{-1}$ were then fitted with Lorenzians. The average islands distance D_{island} was determined as $D_{island} = 2\pi/q_{cen\parallel}$, where $q_{cen\parallel}$ is the center of the peak. Furthermore, from the integrated intensity of the diffuse part of the Yoneda wing [136] the roughness evolution of the film can be estimated.

Figure 10.7 depicts the different data obtained from the GISAXS profiles as a function of film thickness for the different mixing ratios; the extracted D_{island}, the intensity of the anti-Bragg peak, as well as the integrated diffuse intensity is plotted. For different mixing ratios we find different evolutions of the signals with film thickness. The gray vertical lines are used as guides for the eye. For the pure DIP, the anti-Bragg oscillations match the monolayer thicknesses of standing-up DIP molecules. For all other films the anti-Bragg oscillations cannot be easily

explained by the DIP material deposited alone, but complex considerations including coherent and incoherent scattering from domains of different materials play a role.

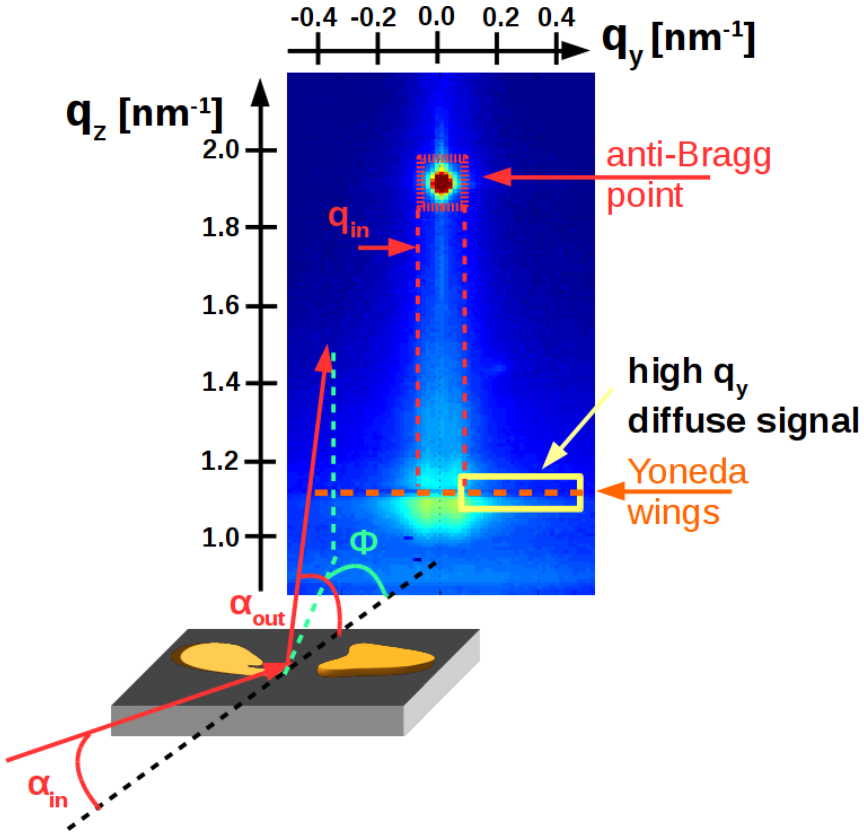

Figure 10.6: Schematic of GISAXS experiment and an example of a GISAXS real-time data acquisition. On the detector image the regions used for data extraction are indicated. The anti-Bragg point corresponds to a specular reflection at half of the q_z value of the DIP (0 0 1) Bragg peak.

The pure DIP (Fig. 10.7a) is consistent with results reported in literature [135, 182]. During the deposition of the first two monolayers D_{island} increases rapidly to $\sim$ 200 nm. From this thickness onwards, D_{island} continuous to grow further up to at least $\sim$ 300 nm, which is the resolution limit of the experiment. However, the well pronounced two anti-Bragg oscillations at the beginning of the growth indicate that DIP grows for the first two layers in a layer-by-layer growth and then the film starts to roughen quickly (damping of the anti-Bragg oscillations), as in Ref [79, 182]. The diffuse signal, which is *inter alia* a measure for the roughness of the film [239], peaks at positions of half-filled layers of the DIP film (for the first two monolayers) and afterwards increases steadily.
The blends with excess DIP, *i.e* DIP:C_{60} 3:1 and 2:1, depict very interesting evolutions of the GISAXS signal, with increasing film thickness. D_{island} increases

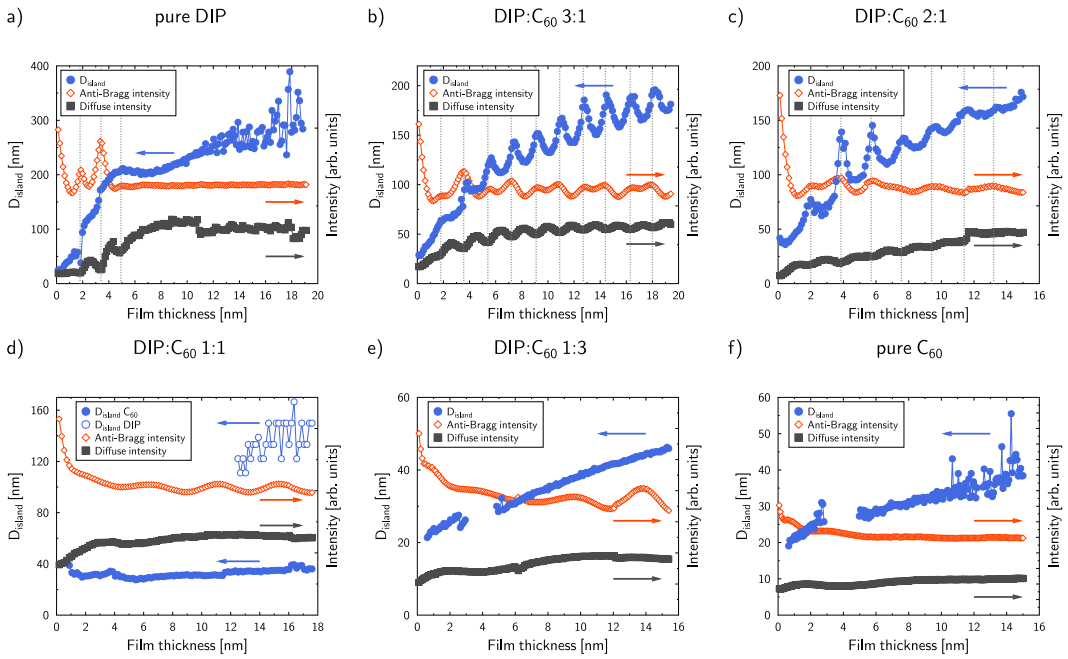

Figure 10.7: The signals extracted from the real-time GISAXS measurements for different mixing ratios all prepared at 303 K. The gray vertical lines are used as guides for the eye to relate the positions of the local maxima in the anti-Bragg signal to the signal of the diffuse intensity and D_{island}. The diffuse intensity and the anti-Bragg intensity are vertically shifted and scaled for clarity. Note that film thickness can be transcribed to growth time.

over the whole film growth, not strictly linearly but with periodic oscillations. Both the anti-Bragg as well as the diffuse intensity also show oscillations over the whole film thickness. The maxima of the diffuse intensity match positions of minima of the anti-Bragg oscillations, which shows again that the roughness of a film has a local maximum when a layer is half filled and reduces afterwards again. The oscillations can be observed over the whole film growth, indicating only slow roughening of the film, with the growth being close to the layer-by-layer mode limit. The anti-Bragg oscillations show two different periodicities which are superimposed and also show different intensity maxima values. This can be attributed to the fact that we are investigating phase separating mixtures and non trivial interference patterns, arising from the different materials, can be expected. Furthermore, it is difficult to designate the maxima of the anti-Bragg oscillations to specific monolayers for mixtures, since DIP and C_{60} are sterically different (ratio of long DIP axis to $C_{60} \sim 2:1$) and therefore the definition of a monolayer is not obvious.

In contrast to blends with DIP excess, the equimolar and C_{60} dominated mixtures show a different evolution of the GISAXS signals (Fig. 10.7d and e). D_{island} is clearly smaller than in the DIP dominated mixtures. Furthermore,

there are neither distinct oscillations in the D_{island} evolution nor in the diffuse signal visible. However, the anti-Bragg intensities for the DIP:C_{60} 1:1 and 1:3 mixtures show oscillations with a periodicity of approximately 4 nm which, surprisingly, get more pronounced with increasing film thickness. In the data of the 1:1 mixture two different features corresponding to two D_{island} are observed, one can be related to DIP and the other to C_{60}, as already observed in post-growth measurements of the same mixture [106]. D_{island} of C_{60} can be basically resolved for the whole growth, however D_{island} of DIP is only indicated by weak peaks in the signal from a thickness of 12 nm onwards. The weak peaks do not allow a fully accurate estimation of D_{island} for DIP, but the order of magnitude is similar to the values reported in literature [106]. Probably before the thickness of 12 nm no well organized islands are formed.

The data of pure C_{60} indicate that C_{60} does not grow in well-ordered layer-by-layer mode on nSiO, whereas this growth mode is observed for films on mica substrates [201]. Rather, the growth of the pure C_{60} and of DIP:C_{60} 1:1 and 1:3 seem to be similar. D_{island} has a similar magnitude and trend of the time-evolution for all three films and also the roughness evolution, estimated from the evolution of the diffuse intensity, is similar. Note that for film thicknesses between 2.5 and 4.5 nm D_{island} could not be determined for DIP:C_{60} 1:3 (and pure C_{60}), since no intensity maxima related to D_{island} were observed in the probed q_y region. In this thickness interval we assume that the films grow again in the layer-by-layer mode. We conclude that presence of DIP facilitates diffusion of more prevalent C_{60} molecules down the molecular steps at the edges of islands, which results in the layer-by-layer growth mode and smoother films compared to pure C_{60}. For C_{60} on mica also thickness regions without well defined in-plane correlation peaks are observed and probably related to completely filled layers [201].

10.4 Discussion

The real-time GIXD and GISAXS measurements revealed different time evolutions of grain sizes and surface morphologies for the different mixing ratios. For 3:1 mixtures, we observe favourable conditions for crystallization of DIP. Additionally, at 373 K we can also resolve the formation of C_{60} crystal grains. The kinetically limited phase separation reported for DIP:C_{60} 1:1 at 303 K [106] is even more pronounced in DIP:C_{60} 3:1. With increasing substrate temperature $D_{coh\parallel}$ increases, indicating a larger length scale of phase separation due to enhanced thermal energy of the molecules. All measurements indicate that DIP:C_{60} forms smoother films at all investigated substrate temperatures compared to pure phase films [79]. From the real-time GISAXS data at 303 K one can conclude a growth mode close to the layer-by-layer mode limit (Fig. 10.8a) accompanied by an increase of the $D_{coh\parallel}$ as well as of D_{island} over the whole film growth. The overall

increase of D_{island} with film thickness means that the average island density decreases with film thickness. For each subsequent layer the domain size increases. The reason for this might be that an improved surface potential landscape by the underlying organic layer leads to higher diffusion lengths of the molecules and therefore for less, but larger islands. The observed continuous filling of the single layers leading to very smooth films might be explained by the C_{60} filling the voids between the DIP crystallites. Besides an overall increase of D_{island} with film thickness an interesting intra-layer behavior of D_{island} is observed. At the beginning of each layer D_{island} decreases, which indicates that new islands are formed. During the further filling of the layer, the number of islands increases, leading to a further decrease of D_{island}. From a certain layer-filling fraction onwards (a little more than 50 %) the islands get very close together and start to coalesce (Fig. 10.8b). This can be seen by an increase of D_{island}. Presumably, the islands do not consist purely of one material and the C_{60} may decorate the step-edges of the DIP, as observed for C_{60} deposited on pentacene [240]. The difference between D_{island} and $D_{coh\|}$ indicates that the islands can include both materials and are not formed by a single coherently scattering domain. Most likely, impinging molecules, of both DIP and C_{60}, which arrive on the top, not completely filled, layer, diffuse relatively fast to the step edge and perform a jump to the layer below to fill the voids between the islands or attach to the islands and increase the islands size. The presence of C_{60} leads potentially to a reduced Ehrlich-Schwoebel barrier [57, 58], in the film. Calculations for C_{60} on top of DIP already suggest a relatively low Ehrlich-Schwoebel barrier which C_{60} has to overcome to jump to a lower layer [241].

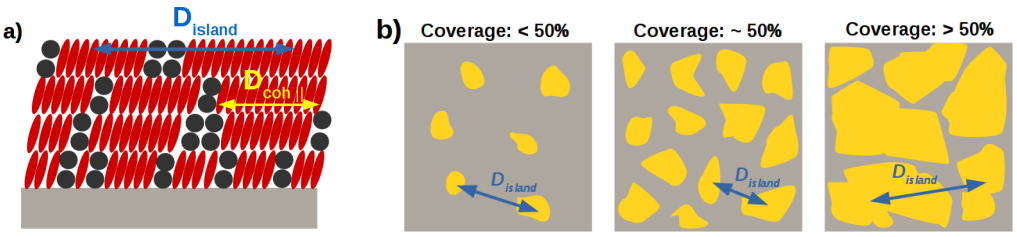

Figure 10.8: Schematic of the growth of DIP:C_{60} 3:1. a) Side view of the almost perfect layer by layer growth. b) Top view of the growth of one layer. For a coverage less than 50 % the number of islands is increasing, resulting in a decrease of D_{island}. At $\sim$ 50 % merging of the islands starts, which leads again to an increase of D_{island} for coverages larger than 50 %.

This is different to pure DIP where a rapid roughening of the film, which has been explained by local spatial inhomogeneities and resulting locally different growth rates [79] and strain effects [242], has been reported. The C_{60} in the mixtures can potentially fill voids between tilted DIP domains and lead to a more homogeneous energetic landscape for molecular diffusion in further layers.

The growth of DIP:C_{60} 1:1 and 1:3 is different. There are no oscillation of

D_{island} with film thickness and the almost constant diffuse signal indicates that the roughness of the films is not strongly changing during the growth, probably since the formed islands are randomly arranged on the surface and not as well ordered as observed for the DIP:C_{60} 3:1 mixture. The overall low roughness for a substrate temperature of 303 K suggests that also for these two mixtures the growth is close to a layer-by-layer mode. However, DIP and C_{60} do not form well-ordered crystallites as observed in the DIP:C_{60} 3:1 mixture. In this case the stochastically mixed fraction of the film seems to dominate the growth.

10.5 Conclusion

In conclusion, we have seen that the mixing ratio has a strong impact on the growth scenario of DIP:C_{60} mixtures. For mixtures in which DIP is the dominant part, the growth resembles the growth of pure DIP, including the formation of pure DIP crystallites, but instead of a rapid roughening and "wedding-cake-like" growth [79], *i.e.* a Stranski-Krastanov growth, a pure Frank-van der Merwe (layer-by-layer) growth is observed with a very smooth top surface. For DIP:C_{60} 3:1 303 K D_{island} increases continuously over the whole film thickness; however $D_{coh\parallel}$ is increasing only very slowly, which means that there is a distinct difference between the coherently scattering domain size and the average island distance (which is related to the island size).
For higher substrate temperatures a stronger increase of $D_{coh\parallel}$ is observed, showing that the length scale of phase separation is increasing with film thickness.
On the other hand, equimolar and C_{60} dominated mixtures show a different growth scenario. The films exhibit a significant lower crystallinity and a weaker increase of $D_{coh\parallel}$ with film thickness. However, at 303 K also a growth mode which is close to the limit of the pure layer-by-layer growth can be expected.

Part III

Conclusion and Outlook

Chapter 11

Summary and Discussion

The goal of this work was the investigation of the thin film structure consisting of the organic semiconductors (OSCs) α-sexithiophene (6T), buckminsterfullerene (C_{60}) and diindenoperylene (DIP), which have been employed in organic photovoltaic cells (OPV cells). The materials were studied in different combinations and spatial arrangements. In the following, first the obtained results are summarized and general guidelines for the growth of OSCs are proposed. This is discussed together with possible consequences for OPV cells. Finally, perspectives for possible further investigations are suggested.

11.1 Results of Pure 6T

11.1.1 Temperature Dependence of the Thin Film Growth

In thin film growth of pure 6T on nSiO, two different phases are observed (Chapter 6) [83]. Depending on the substrate temperature during the deposition and the film thickness either the low-temperature crystal phase (LT-phase) or the β-phase dominate the growth. The major difference between the LT and the β-phase is that the LT-phase is very well ordered and, in contrast, the β-phase is less ordered with a smaller coherently scattering island size. In addition, molecules are slightly more tilted towards the substrate surface in the LT-phase. Therefore, the transition dipole moment of the molecules is better aligned to the incoming light under normal incidence for the LT-phase than for the β-phase. This leads to a slightly higher absorption for the LT-phase.
Close to the substrate (up to film thicknesses of 5 nm), 6T thin films grow predominantly in the β-phase. From these thicknesses onwards, the dominant phase depends strongly on the substrate temperature. At 303 K the β-phase continues to dominate the growth. On the other hand, the LT-phase dominates the growth for thicknesses of 5 nm or more at 373 K. In the literature, similar film structures depending on the deposition rates have been reported: a relatively low deposition rate leads to a structure dominated by the LT-phase, whereas a high deposition

rate results in a film structure where the β-phase is predominantly observed [82].

11.1.2 Annealing of 6T Thin Films

Post-growth annealing to 373 K of 6T films that were prepared at 303 K (dominated by the β-phase) leads to a significant change of the structure (Section 8.3.4) [204]. Domains of the β-phase are transformed into the LT-phase. Interestingly, annealed 6T films show less contributions of the β-phase than 6T films prepared at 373 K. For the latter, an additional annealing at 373 K does not change or improve the crystallinity of the film. These findings indicate that domains of the β-phase which are formed at high substrate temperature are more stable than domains formed at a low substrate temperature.

Overall, one can conclude that crystallites of the LT-phase seem to be thermodynamically more stable than the β-phase. Nevertheless, the formation of the LT-phase is kinetically limited during the film growth at 303 K.

11.2 Results of 6T/C_{60} and 6T/DIP Thin Films with Planar Geometries

In a planar heterostructure with 6T underneath of C_{60} or DIP, strong correlations of the in-plane coherently scattering domain sizes ($D_{coh\parallel}$) of the 6T layer and the top layers are observed (Chapter 8) [192]. From very similar values for $D_{coh\parallel}$ one can deduce that the crystallites in the overlayer are formed directly on top of domains of the underlying 6T. Moreover, DIP molecules adopt the orientation of the 6T molecules, *i.e.* a lying-down or standing-up orientation of the molecules. For C_{60} deposited on top of the 6T, a preferred orientation of the molecules is observed ((1 1 1) plane parallel to the substrate surface), whereas C_{60} forms randomly oriented domains when deposited on nSiO [176]. The templating effect of 6T on C_{60} and DIP might be attributed to the fact that both material combinations form an electron donor-acceptor pair resulting in a strong interaction energy between the materials.

In addition, the formation of DIP crystallites is temperature dependent. At relatively low substrate temperatures, $D_{coh\parallel}$ can only be determined for film thickness of ~ 5 nm onwards. At 373 K, crystallites with measurable $D_{coh\parallel}$ are formed already from the very beginning of the growth. This indicates again the importance of the kinetics for the film growth.

Furthermore, the deposition of any of the two compounds investigated on top of 6T leads to structural changes of the latter. Upon deposition of C_{60} on top of a thin 6T film (2 monolayers), a change of the structure of the underlying 6T from β-phase crystallites into the LT-phase is observed. This might be related to the changes observed during an annealing procedure of pure 6T. However, the difference is that additional energy is not provided by heating the substrate

but rather by incoming new molecules, having a certain kinetic energy (Section 7.3.1.2). The effects observed during the deposition of DIP on top of 6T are in marked contrast to the ones observed during C_{60} deposition. In this case, the DIP causes a transformation from the LT-phase into the β-phase in the 6T (Section 7.3.2.2). These findings reveal that the deposition of a second material on top of an already deposited film can have a strong and often hardly predictable influence on the structure of the latter.
Similar results are expected from molecular dynamic simulations of C_{60} on top of pentacene (PEN), where an intermixing of the two materials and a simultaneous transformation and disruptions of the PEN layers is suggested. In this case, the changes in the structure of the thin films are mainly due to strong intermolecular interactions, observed for arrangements where C_{60} is close to the long molecular axis of PEN, which occur if PEN forms islands (or "wedding-cakes") of standing-up oriented molecules [243].

11.3 Results of 6T:C_{60} Mixtures

In 6T:C_{60} mixtures the structure of the single materials is similar to the one of thin films of the pure materials (Chapter 8) [204]. As expected for sterically incompatible compounds, a phase separation of the two materials is observed. However, the nucleation of 6T domains depends strongly on the temperature of the mixture: at 303 K almost exclusively the 6T β-phase is observed and, on the other hand, at 373 K almost only the 6T LT-phase is seen. Actually, real-time experiments have shown that in the latter case a transformation of β-phase crystallites into LT-phase crystallites occurs in the mixtures, starting at a film thickness which corresponds to approximately two monolayers of pure 6T.

A major difference of the mixtures compared to pure 6T is its behavior upon annealing (Section 8.3.4) [204]. In contrast to pure 6T, which shows a clear improvement in crystallinity and a transformation of β-phase crystallites into LT-phase crystallites, no changes are observed upon annealing of 6T:C_{60} 1:1 mixtures from 303 K to 393 K. This might be attributed to the fact that the C_{60} in the mixture blocks the movement of the 6T which would be necessary for the transformation of the β-phase into the LT-phase.

11.4 Results of DIP:C_{60} Mixtures

Mixtures of DIP and C_{60} represent a prototypical system for phase separating mixtures. For this material combination the phase separation is kinetically limited [106]. Within this work different routes to tailor the length scale of the phase separation, which is (from a perspective of the electronic processes) basically the same as $D_{coh\|}$, were investigated (Chapter 9) [224]. Especially the substrate

temperature during deposition can be used to increase this length scale. The increase in the substrate temperature from 303 K to 373 K during growth leads to an increase of $D_{coh\parallel}$ by a factor of ~ 4 (Section 9.3.2). Furthermore, reducing the deposition rate can have a similar effect. However, we observed an increase of $D_{coh\parallel}$ only at elevated temperatures. Apparently, the temperature dependent diffusion length on the substrate dominates the effect of a reduced probability of aggregation of molecules (leading to a reduced mobility of the molecules) resulting from a lower deposition rate (Section 9.3.3). The results of interrupting the growth repeatedly resemble the results obtained for the different deposition rates. At low deposition rates the interruption of the growth has almost no effect, no significant change in $D_{coh\parallel}$ can be observed. At a relatively high deposition rate the interruptions lead to an increased length scale of phase separation. Probably at low deposition rates, the system is already close to the equilibrium and a further decrease of the effective deposition rate (that is what the interruptions basically are) does not lead to a further improvement (Section 9.3.4). Another method to alter the length scale of phase separation is surface functionalization. By employing thin layers of pure materials, the diffusion length of the molecules can be enhanced compared to the bare substrate. Especially a monolayer of DIP increased $D_{coh\parallel}$ significantly at room temperature and elevated temperatures in comparison to the growth on bare nSiO. Only at low temperatures (243 K) no effect can be observed. Again, in the latter case the temperature effect seems to dominate over the benefits of an increased diffusion length of the molecules, arising from a DIP monolayer (Section 9.3.5). With an increase of the length scale of phase separation, *i.e.* a higher crystallinity, usually also an enhanced surface roughness is observed.

In the case of non-equimolar mixing ratios the situation is different (Chapter 10) [235]. In general, the crystallinity of the pure material phases in the mixtures is reduced compared to pure films. In mixtures with an excess of DIP, the latter grows under the investigated conditions in crystalline domains with a standing-up orientation. However, C_{60} (at all mixing ratios) grows similarly to the pure material on nSiO [176] with randomly oriented crystallites and no preferred crystal orientation. Interestingly, the mixtures show (at least at room temperature) a low surface roughness and a growth mode which is probably very close to the layer-by-layer limit. Enhanced surface diffusion of the molecules and reduced Ehrlich-Schwoebel barriers [57, 58] for the molecules to descend to a lower layer, are likely the reason for this nearly perfect layer-by-layer growth.
The effect of an increasing length scale of phase separation with film thickness [106] is stronger at higher substrate temperatures and also for mixtures with an excess of DIP. This is likely related to enhanced diffusion properties of the molecules.

11.5 Guidelines for the Growth of OSCs and Implications for OPV Cells

In organic photovoltaics the efficiency of the devices are strongly correlated with the structure of the active layers [28, 30, 244]. As already described in Sec. 2.3.1 the overall efficiency of OPV cells (η_{int}) can be expressed as the product of the efficiencies of sub-processes relevant for the energy conversion:

$$\eta_{int} = \eta_{Abs} \cdot \eta_{ED} \cdot \eta_{CT} \cdot \eta_{CC} \tag{11.1}$$

η_{Abs} is the efficiency of absorbing incoming photons, η_{ED} is the efficiency of the excitons reaching the donor-acceptor interface, η_{CT} is the efficiency of exciton dissociation and charge separation, and η_{CC} is the efficiency of the separated charges reaching the electrodes and being collected over the latter.
Usually, it is desired to optimize the structure to obtain the highest overall efficiency. The open circuit voltage V_{OC}, and hence also the efficiency, depend on the energetic arrangement of the highest occupied molecular orbital (HOMO) of the electron donor and the lowest unoccupied molecular orbital (LUMO) of the electron acceptor [229, 245]. It can only be altered to some extent by the structure of the active layer [28, 244]. In the following, guidelines for an improvement of the sub-efficiencies of Eqn. (11.1) are summarized. Nevertheless, from a mere structural point of view, it is impossible to state if the improvement of one sub-efficiency does not cause a lower efficiency for another sub-process, which can result in a reduction in the overall efficiency. Neither can quantitative statements be made. In general, the growth of thin films depends strongly on the ratio of the incoming flux of material and the diffusion length $D(T)$ of the particles on the substrate [225]. From the temperature dependent findings of the 6T growth (Chapter 6) [83] (together with the rate-dependent results from the literature [82]) and the findings from DIP:C_{60} mixtures (Chapter 9) [224], one can conclude that the effects of an elevated substrate temperature and a lower deposition rate are similar. This is valid for both pure materials as well as for mixtures of two phase separating organic compounds.
In the following structural features which can potentially influence the single sub-efficiencies are summarized:

- **Absorption of incoming photons η_{Abs}:** The absorption is mainly an intrinsic material property but often found to be anisotropic (*e.g.* in the case of rod-like molecules). If the transition dipole moment of the molecules are aligned parallel to the electric field vector of the incoming light, the absorption is enhanced. For both 6T and DIP the transition dipole moment is oriented along the long molecular axis [140, 246]. Therefore, molecules in a lying-down configuration increase the absorption under normal incidence. At very low substrate temperatures during the growth, the molecules tend to grow in a lying-down orientation. However, low substrate temperatures

lead to a very small $D_{coh\parallel}$ which decreases the efficiency of the charge and exciton transport in the material. Molecules in a lying-down configuration can be also achieved by a thin template layer of a lying-down material with a strong coupling to the overlayer material (Section 7.3.2.2) [95, 192].

- **Exciton diffusion η_{ED}:** The exciton diffusion length is also a material property. Defects in the film, like crystal grain boundaries, typically reduce the exciton diffusion length. Large crystallite sizes correspond to low defect densities and hence improve the actual exciton diffusion length. In mixtures, the length scale of phase separation should ideally be similar to the exciton diffusion length of the materials so that the majority of the excitons can reach the donor-acceptor interface where they become separated. As described previously (Chapter 9) [224], particularly high substrate temperatures during the growth and low deposition rates lead to larger crystallite sizes (and also a larger length scale of phase separation) and can therefore potentially improve η_{ED}.
  In a planar heterostructure with the acceptor material on top of the donor, or vice versa, an increase of the contact area, and thus a higher probability of the excitons to reach the interface, can be obtained if the bottom material has a rough surface. Often, high surface roughness is observed for films with a high crystallinity. Therefore the same growth conditions as mentioned for large crystallites in the mixtures might be suitable for an enhanced η_{ED}. Similarly, for amorphous organic films, high substrate temperatures and low deposition rates can lead to an increased surface roughness [185]. The fact that the deposition of the overlayer can alter the structure of the underlying material must not be neglected (Sections 7.3.1.2 and 7.3.2.2) [192]. This has also to be considered for the evaporation of a (metal) top electrode.
  As observed, annealing procedures can improve the crystallinity, particularly for pure layers. In mixtures, kinetic traps resulting from the intermixing of the materials on a molecular scale, might prohibit a change in the structure during annealing (Section 8.3.4) [204].

- **Charge transfer η_{CT}:** The exciton dissociation is a complex and not entirely understood process [11, 111]. In the literature, different parameters are discussed which can influence the exciton dissociation at the donor-acceptor interface and also the open-circuit voltage (V_{OC}). On the one hand, it is suggested that the interface should be well ordered to prevent geminate recombination [247]. On the other hand, inhomogeneities in the acceptor distribution at the interface, which are expected to create efficient exciton dissociation sites, as well as smoothness of the interface can increase the exciton dissociation probability [248]. Furthermore, the formation of interface dipoles can reduce the driving force for exciton dissociation, however, the HOMO-LUMO gap (relevant for V_{OC}) can be increased [111].

In addition, the relative orientation of the donor and acceptor molecules can influence the exciton dissociation. In the case of PEN and C_{60}, an orientation where the C_{60} is found close to the short side of the PEN has a higher exciton dissociation rate, compared to a configuration where the C_{60} is close to the long side of the molecules [249].
Since the arguments described above do not indicate one optimal situation for η_{CT}, it is difficult to suggest structural features and hence growth parameters for an improved exciton dissociation. In order to prevent an immediate recombination of the electron and the hole, good charge transport properties, as described in the next point, are required for the free charge carriers to be removed quickly from the donor-acceptor interface.

- **Charge collection η_{CC}:** For the collection of the separated charges the same arguments as mentioned for η_{ED} are valid. Ideally, there are direct percolation paths from the donor-acceptor interface to the electrodes should for an effective charge collection. In a planar geometry (Figure 11.1a), this is usually the case. However, in a mixed active layer (Figure 11.1b), this is not necessarily given. A thin layer of the pure materials between the mixture and the electrodes can be used in order to enhance the probability of forming a direct percolation path from the electrodes to the interface (Section 9.3.5). Another benefit of these pure layers is that they can act as a selective electrode. This is the case if the specific material has good transport properties either for electrons or holes but not for the respective other specie. In OPV cells this geometry is usually denoted as planar mixed heterojunction (PM-HJ) (Figure 11.1c) [250].

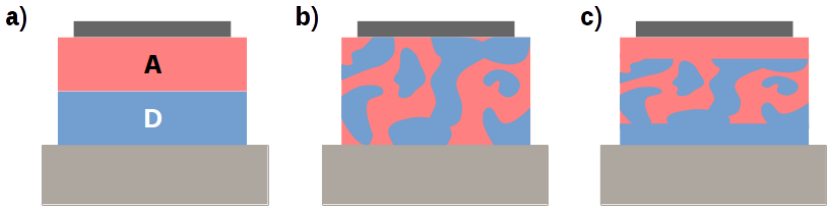

Figure 11.1: Schematic of different geometries in OPV cells. a) Planar heterojunction (PHJ) with the acceptor (A) deposited on top of the donor (D). b) Bulk heterojunction with an active layer of a phase separated mixture of the donor and the acceptor. c) Planar mixed heterojunction (PMHJ) in which the BHJ is sandwiched in between pure layers of the donor and the acceptor. The light gray blocks at the bottom represent the substrate whereas the small dark gray layers on top indicate metal contacts.

11.6 Outlook

Within this thesis not all aspects of the structure of thin films consisting of 6T, C_{60} and DIP could be addressed and the results obtained give rise to further interesting questions.

- For a better understanding of the substrate temperature-dependent growth and annealing experiments of 6T (Chapter 6 and Section 8.3.4), a more detailed description of the thermodynamics of the system might be interesting. The annealing experiments for films prepared at 308 K could be performed more slowly in order to determine the exact temperature where the transformation from the β-phase into the LT-phase occurs. Further annealing of films prepared at 373 K (consisting of a mixture of β- and LT-phase) could give additional information on whether β-phase crystallites which are formed at elevated temperatures, are stable up to the temperature point at which the molecules desorb or if they are transformed into the LT-phase at higher temperatures.

- In the mixtures investigated in this work, usually a very low roughness was observed (Chapters 8, 9 and 10). This is not unique for the mixtures studied within this project but seems to be a rather general property of most mixed organic thin films. Nevertheless, so far no explanation, why these mixtures show a very low roughness is known. It would be interesting if this scenario is also observed for mixtures with more extreme mixing ratios. Furthermore, the investigation of thicker films (which are usually rougher) might show at which thickness the mixtures start to become rougher (if they do).

- We have shown different tools to tailor the length scale of phase separation in mixed films (Chapter 9). However, systematic studies on real device parameters of OPV cells as function of the length scale of phase separation are necessary to determine the ideal case. The results could give more insight into the limiting factors in OPV devices.

- For a better understanding of the growth of mixtures, Monte-Carlo simulations of the growth of sterically incompatible particles might lead to further information about the mechanisms which are relevant for the kinetics of the phase separation.

Appendix A

Hamaker Constant Calculations

The Hamaker constant for two different materials A and B is defined as [251]:

$$A = \pi^2 \cdot \rho_A \cdot \rho_B \cdot C, \tag{A.1}$$

where rha_A and rho_B are the particle densities of the materials and C is the interaction parameter from the van-der-Waals potential, which can usually be assumed for small molecules:

$$V(r) = -\frac{C}{r^6}. \tag{A.2}$$

In the literature usually for C the term C_6 is used [70, 71], indicating that in this case higher order interaction terms are neglected. The values for C can be theoretically obtained from time-dependent Hartree-Fock level or time-dependent density-functional theory calculations [70, 71]. In Table A.1 the homomolecular Hamaker constants for Pentacene and C_{60} are listed, together with the values used for calculations. Obviously $\rho_A = \rho_B$ for the homomolecular Hamaker constant .

	Density [g/cm^3]	Mol. Mass [g/mol]	C_6 [atomic units]	A [J]	A [kJ/mol]
Pentacene [71]	1.30	278.36	28100	$2.1002 \cdot 10^{-19}$	126.475
C_{60} [70]	1.65	720.64	101000	$1.8144 \cdot 10^{-19}$	109.264

Table A.1: Hamaker constants for pentacene and C_{60} calculated from interaction parameters from the literature. C_6 values are from Refs. [70, 71].

Appendix B

C_{60} at 373 K

Fig. B.1 depicts a 2d reciprocal space map image of a 20 nm C_{60} film prepared at 373 K substrate temperature. The well-defined diffraction rings reveal that the domains are not organised in a preferred orientation.

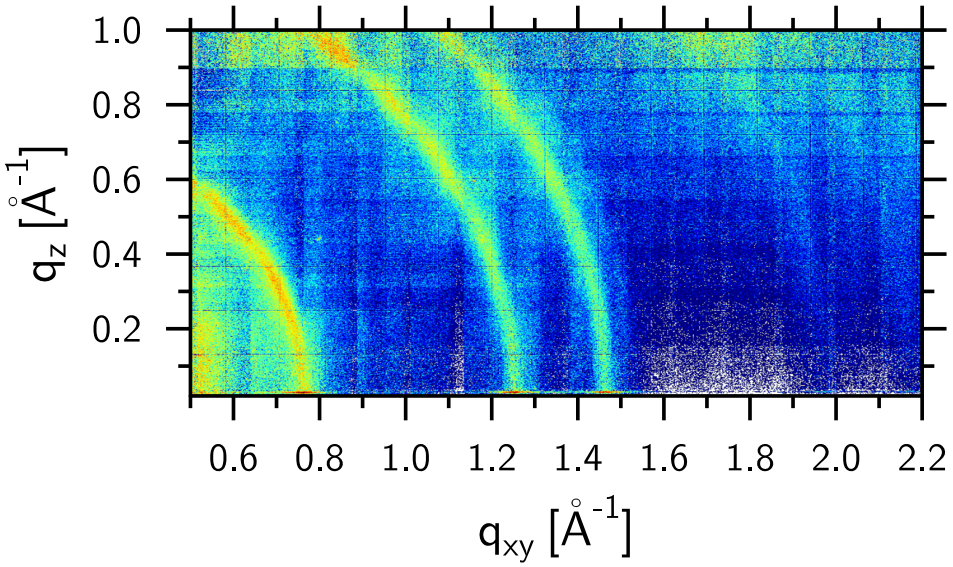

Figure B.1: Reciprocal space map of a 20 nm C_{60} film prepared at 373 K. The image was taken with a MaxiPix area detector and composed of 147 single pictures using the *BINoculars* software [218, 219].

Appendix C

Equimolar DIP:C_{60} Mixtures

C.1 Deposition of Thin Surface Modification Layers

The deposition of a complete monolayer of DIP was estimated using the intensity of the reflected X-ray beam under the so-called “anti-Bragg" condition. [238, 252, 253] For the thin C_{60} layer, the growth was controlled via the QCM and the thickness set to 4 nm. For all the surface modification layers T_{sub} was fixed at 303 K.

C.2 X-Ray Data of DIP:C_{60} 1:1 mixtures

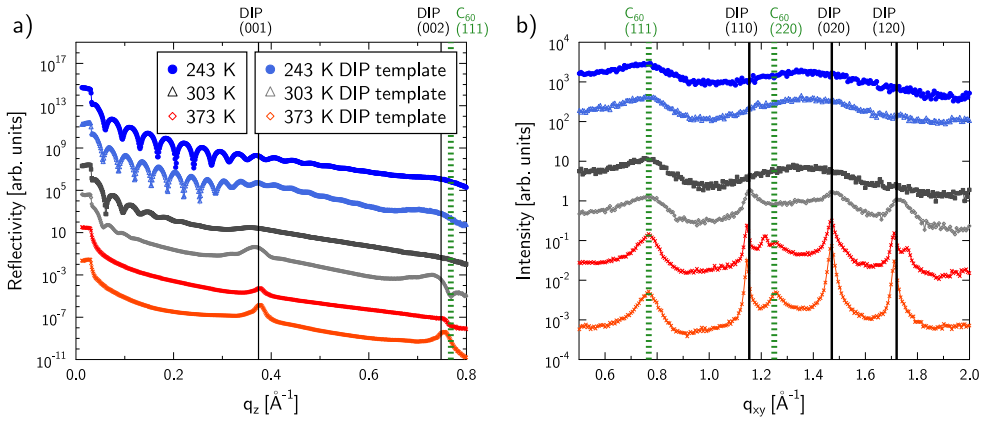

Figure C.1: a) XRR and b) GIXD data of the prepared mixtures at different substrate temperatures. Always two successive curves show the data of the films prepared at the same substrate temperature, whereby the top curve (darker color) is without and the bottom one (brighter color) with a DIP templating layer between the substrate and the mixture.

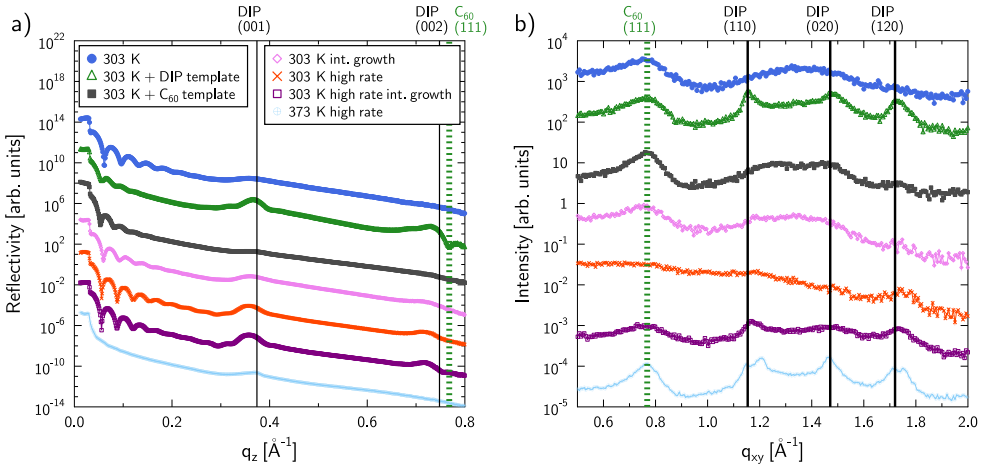

Figure C.2: a) XRR and b) GIXD data of the films prepared with different growth modifications.

List of Figures

List of Tables

Nomenclature and acronyms

$D_{coh\parallel}$	Coherently Scattering In-Plane Domain Size
$D_{coh\perp}$	Coherently Scattering Out-Of-Plane Domain Size
D_{island}	Surface Island Size
$erfc$	Complementary Gaussian Error-Function
η_{Abs}	Efficiency of Photon Absorption
η_{CC}	Efficiency of Charge Transport and Collection
η_{CT}	Efficiency of Exciton Dissociation and Charge Transfer
η_{ED}	Efficiency of Exciton Diffusion
η_{int}	Internal Efficiency of an Organic Solar Cell
$fwhm$	Full Width Half Maximum
r_{dep}	Deposition Rate
σ_{rms}	Root Mean Square Roughness
T_{sub}	Substrate Temperature
V_{OC}	Open Circuit Voltage
6P	*para*-Sexiphenyl
6T	α-Sexithiophene
BHJ	Bulk Heterojunction
C_{60}	Buckminsterfullerene
DIP	Diindenoperylene

ESRF	European Synchrotron Radiation Facility
fcc	Face Centered Cubic
GISAXS	Grazing Incidence Small Angle X-Ray Scattering
GIXD	Grazing Incidence X-Ray Diffraction
H_2-PC	H_2-Phthalocyanines
hcp	Hexagonal Closed Packed
HOMO	Highest Occupied Molecular Orbital
IQE	Internal Quantum Efficiency
ITO	Indium Tin Oxide
LT-Phase	Low Temperature Phase
LUMO	Lowest Unoccupied Molecular Orbital
nSiO	Native Silicon Oxide
OFET	Organic Field Effect Transistor
OLED	Organic Light Emitting Diode
OMBD	Organic Molecular Beam Deposition
OPV	Organic Photovoltaics
OSC	Organic Semiconductors
PEN	Pentacene
PHJ	Planar Heterojunction
PM-HJ	Planar-Mixed Heterojunction
QCM	Quartz Crystal Microbalance
sc	Simple Cubic
SLD	Scattering Length Density
SLS	Swiss Light Source
UHV	Ultra-High Vacuum
XRR	X-Ray Reflectivity

Bibliography

[1] A. Pochettino, Atti Acad. Lincei Rend. **15(1)**, 355 (1906).

[2] A. Pochettino, Atti Acad. Lincei Rend. **15(2)**, 171 (1906).

[3] T. Tsutsui and K. Fujita, Adv. Mater. **14**, 949 (2002): *The shift from "hard" to "soft" electronics.*

[4] C. D. Dimitrakopoulos and D. J. Mascaro, IBM J. Res. & Dev. **45**, 11 (2001): *Organic thin-film transistors: A review of recent advances.*

[5] T. Mori, J. Phys.: Condens. Matter **20**, 184010 (2008): *Molecular materials for organic field-effect transistors.*

[6] Y. Wakayama, R. Hayakawa, and H.-S. Seo, Sci. Technol. Adv. Mater. **15**, 024202 (2014): *Recent progress in photoactive organic field-effect transistors.*

[7] Y. Yang, J. Ouyang, L. Ma, R.-H. Tseng, and C.-W. Chu, Adv. Funct. Mater. **16**, 1001 (2006): *Electrical Switching and Bistability in Organic/Polymeric Thin Films and Memory Devices.*

[8] Q.-D. Ling, D.-J. Liaw, C. Zhu, D. S.-H. Chan, E.-T. Kang, and K.-G. Neoh, Prog. Polym. Sci. **33**, 917 (2008): *Polymer electronic memories: Materials, devices and mechanisms.*

[9] P. Heremans, G. H. Gelinck, R. Müller, K.-J. Baeg, D.-Y. Kim, and Y.-Y. Noh, Chem. Mater. **23**, 341 (2011): *Polymer and Organic Nonvolatile Memory Devices.*

[10] *Organic Photovoltaics: Concepts and applications*, Wiley-VCH (Weinheim), edited by C. Brabec, V. Dyakonov, J. Parisi, and N. Sariciftci (2003).

[11] B. Kippelen and J.-L. Brédas, Energy Environ. Sci. **2**, 251 (2009): *Organic photovoltaics.*

[12] S. R. Forrest, MRS Bull. **30**, 28 (2005): *The Limits to Organic Photovoltaic Cell Efficiency.*

[13] H. Hoppe and N. S. Sariciftci, J. Mater. Res. **19**, 1924 (2004): *Organic solar cells: An overview.*

[14] C. Deibel and V. Dyakonov, Rep. Prog. Phys. **73**, 096401 (2010): *Polymer-fullerene bulk heterojunction solar cells.*

[15] Website of Enerdata: `http://www.enerdata.net/`, accessed 2015/05/25.

[16] Website of the U.S. Energy Information Administration: `http://www.eia.gov/`, accessed 2015/05/25.

[17] Website of the National Center for Photovoltaics: `http://www.nrel.gov/ncpv/`, accessed 2015/09/15.

[18] C. W. Tang, Appl. Phys. Lett. **48**, 183 (1986): *Two-layer organic photovoltaic cell.*

[19] S. Kowarik, A. Gerlach, M. W. A. Skoda, S. Sellner, and F. Schreiber, Eur. Phys. J. Special Topics **167**, 11 (2009): *Real-time studies of thin film growth: Measurement and analysis of X-ray growth oscillations beyond the anti-Bragg point.*

[20] S. Kowarik, A. Gerlach, S. Sellner, L. Cavalcanti, and F. Schreiber, Adv. Eng. Mater. **11**, 291 (2009): *Dewetting in an organic semiconductor thin film observed in real-time.*

[21] A. Gerlach, S. Sellner, S. Kowarik, and F. Schreiber, phys. stat. sol. (a) **205**, 461 (2008): *In-situ X-ray scattering studies of OFET interfaces.*

[22] S. Kowarik, A. Gerlach, and F. Schreiber, J. Phys.: Condens. Matter **20**, 184005 (1 (2008): *Organic molecular beam deposition: Fundamentals, growth dynamics, and in-situ studies.*

[23] S. Kowarik, Ph.D. thesis, Wadham College, Oxford, 2006.

[24] S. Veenstra, G. Malliaras, H. Brouwer, F. Esselink, V. Krasnikov, P. van Hutten, J. Wildeman, H. Jonkman, G. Sawatzky, and G. Hadziioannou, Synth. Met. **84**, 971 (1997): *Sexithiophene-C_{60} blends as model systems for photovoltaic devices.*

[25] S. Alem, A. K. Pandey, K. N. N. Unni, J.-M. Nunzi, and P. Blanchard, J. Vac. Sci. Technol. A **24**, 645 (2006): *Molecular model T6:C_{60} bulk-heterojunction solar cells.*

[26] J. Wagner, M. Gruber, A. Hinderhofer, A. Wilke, B. Bröker, J. Frisch, P. Amsalem, A. Vollmer, A. Opitz, N. Koch, F. Schreiber, and W. Brütting, Adv. Funct. Mater. **20**, 4295 (2010): *High fill factor and open circuit voltage in organic photovoltaic cells with diindenoperylene as donor material.*

[27] U. Hörmann, J. Wagner, M. Gruber, A. Opitz, and W. Brütting, phys. status solidi RRL **5**, 241 (2011): *Approaching the ultimate open circuit voltage in thiophene based single junction solar cells by applying diindenoperylene as acceptor.*

[28] U. Hörmann, C. Lorch, A. Hinderhofer, A. Gerlach, M. Gruber, J. Kraus, B. Sykora, S. Grob, T. Linderl, A. Wilke, A. Opitz, R. Hansson, A. S. Anselmo, Y. Ozawa, Y. Nakayama, H. Ishii, N. Koch, E. Moons, F. Schreiber, and W. Brütting, J. Phys. Chem. C **118**, 26462 (2014): *V_{OC} from a morphology point of view: the Influence of molecular orientation on the open circuit voltage of organic planar heterojunction solar cells.*

[29] A. K. Tripathi and J. Pflaum, Appl. Phys. Lett. **89**, 082103 (2006): *Correlation between ambipolar transport and structural phase transition in diindenoperylene single crystals.*

[30] A. Opitz, J. Wagner, W. Brütting, I. Salzmann, N. Koch, J. Manara, J. Pflaum, A. Hinderhofer, and F. Schreiber, IEEE J. Sel. Top. Quant. **16**, 1707 (2010): *Charge separation at molecular donor-acceptor interfaces: correlation between morphology and solar cell performance.*

[31] R. Farchioni and G. Grosso, Springer-Verlag (Berlin), *Organic Electronic Materials* (2001).

[32] T. W. Kelley, P. F. Baude, C. Gerlach, D. E. Ender, D. Muyres, M. A. Haase, D. E. Vogel, and S. D. Theiss, Chem. Mater. **16**, 4413 (2004): *Recent progress in organic electronics: Materials, devices, and processes.*

[33] S. R. Forrest, Nature **428**, 911 (2004): *The path to ubiquitous and low-cost organic electronic appliances on plastic.*

[34] H. E. Katz and J. Huang, Annu. Rev. Mater. Res. **39**, 71 (2009): *Thin-Film Organic Electronic Devices.*

[35] *Physics of organic semiconductors*, 2nd ed., Wiley-VCH (Weinheim), edited by W. Brütting and C. Adachi (2012).

[36] O. D. Jurchescu, Ph.D. thesis, Rijksuniversiteit Groningen, 2006.

[37] S. R. Forrest, Chem. Rev. **97**, 1793 (1997): *Ultrathin organic films grown by organic molecular beam deposition and related techniques.*

[38] F. Schreiber, phys. stat. sol. (a) **201**, 1037 (2004): *Organic molecular beam deposition: Growth studies beyond the first monolayer.*

[39] *Handbook of Organic Conductive Molecules and Polymers*, John Wiley & Sons (Chichester), edited by H. S. Nalwa (1997).

[40] N. C. Greenham, Phil. Trans. R. Soc. A **371**, 20110414 (2013): *Polymer solar cells.*

[41] M. Schwoerer and H. C. Wolf, Wiley-VCH (Weinheim), *Organic molecular solids* (2005).

[42] E. A. Meyer, R. K. Castellano, and F. Diederich, Angew. Chem. Int. Ed. **42**, 1210 (2003): *Interactions with Aromatic Rings in Chemical and Biological Recognition.*

[43] A. Kitaigorodsky, in *Molecular Crystals and Molecules*, Academic Press (London, New York), edited by E. M. Loebl (1973).

[44] R. Eisenschitz and F. London, Z. Physik **60**, 491 (1930): *Über das Verhältnis der van der Waalsschen Kräfte zu den homöopolaren Bindungskräften.*

[45] J. Vrbancich and G. L. D. Ritchie, J. Chem. Soc., Faraday Trans. 2 **76**, 648 (1980): *Quadrupole Moments of Benzene, Hexafluorobenzene and Other Non-dipolar Aromatic Molecules.*

[46] A. Hinderhofer, Ph.D. thesis, Eberhard Karls Universität Tübingen, 2011.

[47] G. R. Desiraju and A. Gavezzotti, Acta Cryst. B **45**, 473 (1989): *Crystal structures of polynuelear aromatic hydrocarbons. Classification, rationalization and prediction from molecular structure.*

[48] G. R. Desiraju and A. Gavezzotti, J. Chem. Soc., Chem. Commun. **10**, 621 (1989): *From molecular to crystal structure; polynuclear aromatic hydrocarbons.*

[49] K. Reichenbächer, H. I. Süss, and J. Hulliger, Chem. Soc. Rev. **34**, 22 (2005): *Fluorine in crystal engineering - "the little atom that could".*

[50] I. Salzmann, S. Duhm, G. Heimel, J. P. Rabe, N. Koch, M. Oehzelt, Y. Sakamoto, and T. Suzuki, Langmuir **24**, 7294 (2008): *Structural Order in Perfluoropentacene Thin Films and Heterostructures with Pentacene.*

[51] K. Broch, U. Heinemeyer, A. Hinderhofer, F. Anger, R. Scholz, A. Gerlach, and F. Schreiber, Phys. Rev. B **83**, 245307 (2011): *Optical evidence for intermolecular coupling in mixed films of pentacene and perfluoropentacene.*

[52] A. Hinderhofer, C. Frank, T. Hosokai, A. Resta, A. Gerlach, and F. Schreiber, J. Chem. Phys. **134**, 104702 (2011): *Structure and morphology of coevaporated pentacene-perfluoropentacene thin films.*

[53] L. E. Scriven, MRS Proc. **121**, 717 (2011): *Physics and Applications of DIP Coating and Spin Coating.*

[54] L. Wengeler, M. Schmitt, K. Peters, P. Scharfer, and W. Schabel, Chem. Eng. Process. Process Intensif. **68**, 38 (2013): *Comparison of large scale coating techniques for organic and hybrid films in polymer based solar cells.*

[55] H. Sirringhaus, T. Kawase, R. H. Friend, T. Shimoda, M. Inbasekaran, W. Wu, and E. P. Woo, Science **290**, 2123 (2000): *High-Resolution Inkjet Printing of All-Polymer Transistor Circuits.*

[56] M. Knudsen, Ann. Phys. **333**, 999 (1909): *Die Molekularströmung der Gase durch Öffnungen und die Effusion.*

[57] G. Ehrlich and F. G. Hudda, J. Chem. Phys. **44**, 1039 (1966): *Atomic View of Surface Self-Diffusion: Tungsten on Tungsten.*

[58] R. L. Schwoebel and E. J. Shipsey, J. Appl. Phys. **37**, 3682 (1966): *Step Motion on Crystal Surfaces.*

[59] G. Hlawacek, P. Puschnig, P. Frank, A. Winkler, C. Ambrosch-Draxl, and C. Teichert, Science **321**, 108 (2008): *Characterization of Step-Edge Barriers in Organic Thin-Film Growth.*

[60] X. Zhang, E. Barrena, D. Goswami, D. G. de Oteyza, C. Weis, and H. Dosch, Phys. Rev. Lett. **103**, 136101 (2009): *Evidence for a Layer-Dependent Ehrlich-Schwoebel Barrier in Organic Thin Film Growth.*

[61] J. A. Venables, G. D. T. Spiller, and M. Hanbücken, Rep. Prog. Phys. **47**, 399 (1984): *Nucleation and growth of thin films.*

[62] A. Pimpinelli and J. Villain, Cambridge University Press (Cambridge), *Physics of Crystal Growth* (1998).

[63] J. A. Venables, Cambridge University Press (Cambridge), *Introduction to surface and thin film processes* (2000).

[64] I. V. Markov, World Scientific Press (New Jersey, London, Singapore, Hong Kong), *Crystal growth for beginners*, 2nd ed., (2004).

[65] J. Krug, Adv. Phys. **46**, 139 (1997): *Origins of scale invariance in growth processes.*

[66] J. Krug, Physica A **313**, 47 (2002): *Four lectures on the physics of crystal growth.*

[67] F. Brochard-Wyart, J. M. Di Meglio, D. Quere, and P. G. De Gennes, Langmuir **7**, 335 (1991): *Spreading of nonvolatile liquids in a continuum picture.*

[68] P. G. de Gennes, Rev. Mod. Phys. **57**, 827 (1985): *Wetting: statics and dynamics.*

[69] B. Lewis and J. C. Anderson, Academic Press (London, New York, San Francisco), *Nucleation and Growth of Thin Films* (1978).

[70] A. Jiemchooroj, P. Norman, and B. E. Sernelius, J. Chem. Phys. **123**, 124312 (2005): *Complex polarization propagator method for calculation of dispersion coefficients of extended π-conjugated systems: The C_6 coefficients of polyacenes and C_{60}.*

[71] M. A. L. Marques, A. Castro, G. Malloci, G. Mulas, and S. Botti, J. Chem. Phys. **127**, 014107 (2007): *Efficient calculation of van der Waals dispersion coefficients with time-dependent density functional theory in real time: Application to polycyclic aromatic hydrocarbons.*

[72] J. N. Israelachvili, in *Chapter 13 - Van der Waals Forces between Particles and Surfaces*, third ed., Academic Press (San Diego), edited by J. N. Israelachvili (2011), pp. 253 – 289.

[73] J. Pflaum, J. Niemax, and A. Tripathi, Chem. Phys. **325**, 152 (2006): *Chemical and structural effects on the electronic transport in organic single crystals.*

[74] U. Heinemeyer, A. Hinderhofer, M. I. Alonso, J. O. Ossó, M. Garriga, M. Kytka, A. Gerlach, and F. Schreiber, phys. stat. sol. (a) **205**, 927 (2008): *Uniaxial anisotropy of organic thin films determined by ellipsometry.*

[75] F. M. zu Heringdorf, M. C. Reuter, and R. M. Tromp, Nature (London, U. K.) **412**, 517 (2001): *Growth dynamics of pentacene thin Films.*

[76] A. Dürr, B. Nickel, V. Sharma, U. Täffner, and H. Dosch, Thin Solid Films **503**, 127 (2006): *Observation of competing modes in the growth of diindenoperylene on SiO_2.*

[77] B.-E. Schuster, M. B. Casu, I. Biswas, A. Hinderhofer, A. Gerlach, F. Schreiber, and T. Chassé, Phys. Chem. Chem. Phys. **11**, 9000 (2009): *Role of the substrate in electronic structure, molecular orientation, and morphology of organic thin films: diindenoperylene on rutile TiO_2(110).*

[78] S. Kowarik, A. Gerlach, S. Sellner, F. Schreiber, L. Cavalcanti, and O. Konovalov, Phys. Rev. Lett. **96**, 125504 (2006): *Real-time observation of structural and orientational transitions during growth of organic thin films.*

[79] A. C. Dürr, F. Schreiber, K. A. Ritley, V. Kruppa, J. Krug, H. Dosch, and B. Struth, Phys. Rev. Lett. **90**, 016104 (2003): *Rapid Roughening in Thin Film Growth of an Organic Semiconductor (Diindenoperylene).*

[80] C. C. Mattheus, A. B. Dros, J. Baas, G. T. Oostergetel, A. Meetsma, J. L. de Boer, and T. T. Palstra, Synth. Met. **138**, 475 (2003): *Identification of polymorphs of pentacene.*

[81] C. C. Mattheus, G. A. de Wijs, R. A. de Groot, and T. T. M. Palstra, J. Am. Chem. Soc. **125**, 6323 (2003): *Modeling the polymorphism of pentacene.*

[82] A. Moser, I. Salzmann, M. Oehzelt, A. Neuhold, H.-G. Flesch, J. Ivanco, S. Pop, T. Toader, D. R. Zahn, D.-M. Smilgies, and R. Resel, Chem. Phys. Lett. **574**, 51 (2013): *A disordered layered phase in thin films of sexithiophene.*

[83] C. Lorch, R. Banerjee, C. Frank, J. Dieterle, A. Hinderhofer, A. Gerlach, and F. Schreiber, J. Phys. Chem. C **119**, 819 (2015): *Growth of competing crystal phases of α-sexithiophene studied by real-time X-ray scattering.*

[84] N. Karl, in *Charge carrier mobility in organic crystals*, Springer (Berlin), edited by R. Farchioni and G. Grosso (2001).

[85] J. Sworakowski, K. Janus, S. Nespurek, and M. Vala, IEEE T. Dielect. El. In. **13**, 1001 (2006): *Local States in Organic Materials: Charge Transport and Localization.*

[86] A. Hinderhofer and F. Schreiber, ChemPhysChem **13**, 628 (2012): *Organic-organic heterostructures: Concepts and applications.*

[87] I. V. Markov, World Scientific (Singapore, London), *Crystal growth for beginners : fundamentals of nucleation, crystal growth and epitaxy* (1994).

[88] M. Oehzelt, G. Koller, J. Ivanco, S. Berkebile, T. Haber, R. Resel, F. P. Netzer, and M. G. Ramsey, Adv. Mater. **18**, 2466 (2006): *Organic heteroepitaxy: p-sexiphenyl on uniaxially oriented α-sexithiophene.*

[89] G. Koller, S. Berkebile, J. R. Krenn, F. P. Netzer, M. Oehzelt, T. Haber, R. Resel, and M. G. Ramsey, Nano Lett. **6**, 1207 (2006): *Heteroepitaxy of organic-organic nanostructures.*

[90] T. Djuric, G. Hernandez-Sosa, G. Schwabegger, M. Koini, G. Hesser, M. Arndt, M. Brinkmann, H. Sitter, C. Simbrunner, and R. Resel, J. Mater. Chem. **22**, 15316 (2012): *Alternately deposited heterostructures of α-sexithiophene-para-hexaphenyl on muscovite mica(001) surfaces: crystallographic structure and morphology.*

[91] H. L. Zhang, W. Chen, L. Chen, H. Huang, X. S. Wang, J. Yuhara, and A. T. S. Wee, Small **3**, 2015 (2007): *C_{60} molecular chains on α-sexithiophene nanostripes.*

[92] L. Chen, W. Chen, H. Huang, H. Zhang, J. Yuhara, and A. Wee, Adv. Mater. **20**, 484 (2008): *Tunable arrays of C_{60} molecular chains.*

[93] R. Wang, H. Y. Mao, H. Huang, D. C. Qi, and W. Chen, J. Appl. Phys. **109**, 084307 (2011): *Scanning tunneling microscopy and photoelectron spectroscopy investigation of the sexithiophene:C60 donor-acceptor nanostructure formation on graphite.*

[94] W. Chen, H. Zhang, H. Huang, L. Chen, and A. T. S. Wee, ACS Nano **2**, 693 (2008): *Orientationally Ordered C_{60} on p-Sexiphenyl Nanostripes on Ag(111).*

[95] S. Heutz, R. Cloots, and T. S. Jones, Appl. Phys. Lett. **77**, 3938 (2000): *Structural templating effects in molecular heterostructures grown by organic molecular-beam deposition.*

[96] A. Hinderhofer, A. Gerlach, S. Kowarik, F. Zontone, J. Krug, and F. Schreiber, Europhys. Lett. **91**, 56002 (2010): *Smoothing and coherent structure formation in organic-organic heterostructure growth.*

[97] Y. Zhang, E. Barrena, X. Zhang, A. Turak, F. Maye, and H. Dosch, J. Phys. Chem. C **114**, 13752 (2010): *New Insight into the Role of the Interfacial Molecular Structure on Growth and Scaling in Organic Heterostructures.*

[98] D. G. de Oteyza, E. Barrena, J. O. Ossó, S. Sellner, and H. Dosch, Chem. Mater. **18**, 4212 (2006): *Site-Selective Molecular Organization in Organic Heterostructures.*

[99] D. G. de Oteyza, E. Barrena, S. Sellner, J. O. Ossó, and H. Dosch, Surf. Sci. **601**, 4117 (2007): *Role of the substrate thickness for the structural properties of organic-organic heterostructures.*

[100] E. Barrena, D. G. de Oteyza, S. Sellner, H. Dosch, J. O. Ossó, and B. Struth, Phys. Rev. Lett. **97**, 076102 (2006): *In Situ Study of the Growth of Nanodots in Organic Heteroepitaxy.*

[101] D. de Oteyza, E. Barrena, S. Sellner, J. Ossó, and H. Dosch, Thin Solid Films **516**, 7525 (2008): *Molecular structure and growth morphologies of pentacene/fluorinated copper-phthalocyanine heterostructures.*

[102] D. G. de Oteyza, E. Barrena, Y. Zhang, T. N. Krauss, A. Turak, A. Vorobiev, and H. Dosch, J. Phys. Chem. C **113**, 4234 (2009): *Experimental Relation between Stranski-Krastanov Growth of DIP/F_{16}CoPc Heterostructures and the Reconstruction of the Organic Interface.*

[103] A. Kitaigorodsky, in *Mixed Crystals*, Springer (Berlin, Heidelberg), edited by M. Cordona (1984).

[104] A. Aufderheide, K. Broch, J. Novák, A. Hinderhofer, R. Nervo, A. Gerlach, R. Banerjee, and F. Schreiber, Phys. Rev. Lett. **109**, 156102 (2012): *Mixing-Induced Anisotropic Correlations in Molecular Crystalline Systems.*

[105] K. Broch, A. Aufderheide, L. Raimondo, A. Sassella, A. Gerlach, and F. Schreiber, J. Phys. Chem. C **117**, 13952 (2013): *Optical Properties of Blends: Influence of Mixing-Induced Disorder in Pentacene:Diindenoperylene versus Perfluoropentacene:Diindenoperylene.*

[106] R. Banerjee, J. Novák, C. Frank, C. Lorch, A. Hinderhofer, A. Gerlach, and F. Schreiber, Phys. Rev. Lett. **110**, 185506 (2013): *Evidence for Kinetically Limited Thickness Dependent Phase Separation in Organic Thin Film Blends.*

[107] K. Broch, A. Gerlach, C. Lorch, J. Dieterle, J. Novák, A. Hinderhofer, and F. Schreiber, J. Chem. Phys. **139**, 174709 (2013): *Structure formation in perfluoropentacene:diindenoperylene blends and its impact on transient effects in the optical properties studied in real-time during growth.*

[108] K. Broch, C. Bürker, J. Dieterle, S. Krause, A. Gerlach, and F. Schreiber, Phys. Status Solidi RRL **7**, 1084 (2013): *Impact of molecular tilt angle on the absorption spectra of pentacene:perfluoropentacene blends.*

[109] S. Ahmad, Journal of Polymer Engineering **34**, 279 (2014): *Organic semiconductors for device applications: current trends and future prospects.*

[110] J. C. Bernède, J. Chil. Chem. Soc. **53**, 1549 (2008): *Organic photovoltaic cells: History, principle and techniques.*

[111] J.-L. Brédas, J. E. Norton, J. Cornil, and V. Coropceanu, Acc. Chem. Res. **42**, 1691 (2009): *Molecular Understanding of Organic Solar Cells: The Challenges.*

[112] W. Cao and J. Xue, Energy Environ. Sci. **7**, 2123 (2014): *Recent progress in organic photovoltaics: device architecture and optical design.*

[113] A. Zhugayevych and S. Tretiak, Annu. Rev. Phys. Chem. **66**, 305 (2015): *Theoretical Description of Structural and Electronic Properties of Organic Photovoltaic Materials.*

[114] N. Thejo Kalyani and S. Dhoble, Renew. Sustainable Energy Rev. **16**, 2696 (2012): *Organic light emitting diodes: Energy saving lighting technology – A review.*

[115] J. Mei, Y. Diao, A. L. Appleton, L. Fang, and Z. Bao, J. Am. Chem. Soc. **135**, 6724 (2013): *Integrated Materials Design of Organic Semiconductors for Field-Effect Transistors.*

[116] O. A. Melville, B. H. Lessard, and T. P. Bender, ACS Appl. Mater. Interfaces **7**, 13105 (2015): *Phthalocyanine-Based Organic Thin-Film Transistors: A Review of Recent Advances.*

[117] D. Sun, E. Ehrenfreund, and Z. Valy Vardeny, Chem. Commun. **50**, 1781 (2014): *The first decade of organic spintronics research.*

[118] L. Ma, S. Pyo, J. Ouyang, Q. Xu, and Y. Yang, Appl. Phys. Lett. **82**, 1419 (2003): *Nonvolatile electrical bistability of organic/metal-nanocluster/organic system.*

[119] M. A. Reed, J. Chen, A. M. Rawlett, D. W. Price, and J. M. Tour, Appl. Phys. Lett. **78**, 3735 (2001): *Molecular random access memory cell.*

[120] J. Als-Nielsen and D. McMorrow, John Wiley & Sons, Ltd (Chichester), *Elements of Modern X-ray Physics*, 2nd ed. (2011).

[121] M. Birkholz, Wiley-VCH (Weinheim), *Thin Film Analysis by X-Ray Scattering* (2006).

[122] M. Tolan, Springer (Berlin, London), *X-ray scattering from soft-matter thin films : materials science and basic research*, *Springer tracts in modern physics* (1999).

[123] L. G. Parratt, Phys. Rev. **95**, 359 (1954): *Surface studies of solids by total reflection of X-rays.*

[124] H. Kiessig, Ann. Phys. **402**, 769 (1931): *Interferenz von Röntgenstrahlen an dünnen Schichten.*

[125] P. Croce and L. Névot, Rev. Phys. Appl. (Paris) **11**, 113 (1976): *Étude des couches minces et des surfaces par réflexion rasante, spéculaire ou diffuse, de rayons X.*

[126] L. Névot and P. Croce, Revue de Physique Appliquée **15**, 761 (1980): *Characterisation of surfaces by grazing x-ray reflection.*

[127] P. Scherrer, Nachr. Ges. Wiss. Göttingen, Math-Phys Kl. **1918**, 98 (1918): *Bestimmung der Größe und der inneren Struktur von Kolloidteilchen mittels Röntgenstrahlen.*

[128] A. Patterson, Phys. Rev. **56**, 978 (1939): *The Scherrer Formula of X-Ray particle size determination.*

[129] B. E. Warren, Addison-Wesley Pub. Co. (Reading, Mass.,) *X-Ray diffraction, Addison-Wesley series in metallurgy and materials.* (1969).

[130] D.-M. Smilgies, J. Appl. Crystallogr. **42**, 1030 (2009): *Scherrer grain-size analysis adapted to grazing-incidence scattering with area detectors.*

[131] R. Lazzari, F. Leroy, and G. Renaud, Phys. Rev. B **76**, 125411 (2007): *Grazing-incidence small-angle x-ray scattering from dense packing of islands on surfaces: Development of distorted wave Born approximation and correlation between particle sizes and spacing.*

[132] G. Renaud, R. Lazzari, and F. Leroy, Surf. Sci. Rep. **64**, 255 (2009): *Probing surface and interface morphology with Grazing Incidence Small Angle X-Ray Scattering.*

[133] J. Daillant and A. Gibaud, Springer (Berlin, Heidelberg), *X-Ray and Neutron Reflectivity* (2009).

[134] C. Frank, Ph.D. thesis, Universität Tübingen, 2014.

[135] C. Frank, R. Banerjee, M. Oettel, A. Gerlach, J. Novák, G. Santoro, and F. Schreiber, Phys. Rev. B **90**, 205401 (2014): *Analysis of island shape evolution from diffuse x-ray scattering of organic thin films and implications for growth.*

[136] Y. Yoneda, Phys. Rev. **131**, 2010 (1963): *Anomalous Surface Reflection of X Rays.*

[137] K. A. Ritley, B. Krause, F. Schreiber, and H. Dosch, Rev. Sci. Instrum. **72**, 1453 (2001): *A portable ultrahigh vacuum organic molecular beam deposition system for in situ x-ray diffraction measurements.*

[138] F. Dinelli, M. Murgia, P. Levy, M. Cavallini, F. Biscarini, and D. M. de Leeuw, Phys. Rev. Lett. **92**, 116802 (2004): *Spatially Correlated Charge Transport in Organic Thin Film Transistors.*

[139] M. I. Alonso, M. Garriga, N. Karl, J. O. Ossó, and F. Schreiber, Org. Electron. **3**, 23 (2002): *Anisotropic optical properties of single crystalline PTCDA studied by spectroscopic ellipsometry.*

[140] U. Heinemeyer, R. Scholz, L. Gisslén, M. I. Alonso, J. O. Ossó, M. Garriga, A. Hinderhofer, M. Kytka, S. Kowarik, A. Gerlach, and F. Schreiber, Phys. Rev. B **78**, 085210 (2008): *Exciton-phonon coupling in diindenoperylene thin films.*

[141] B. Servet, S. Ries, M. Trotel, P. Alnot, G. Horowitz, and F. Garnier, Adv. Mater. **5**, 461 (1993): *X-ray determination of the crystal structure and orientation of vacuum evaporated sexithiophene films.*

[142] B. Servet, G. Horowitz, S. Ries, O. Lagorsse, P. Alnot, A. Yassar, F. Deloffre, P. Srivastava, and R. Hajlaoui, Chem. Mater. **6**, 1809 (1994): *Polymorphism and Charge Transport in Vacuum-Evaporated Sexithiophene Films.*

[143] G. Horowitz, B. Bachet, A. Yassar, P. Lang, F. Demanze, J.-L. Fave, and F. Garnier, Chem. Mater. **7**, 1337 (1995): *Growth and characterization of sexithiophene single crystals.*

[144] T. Siegrist, R. Fleming, R. Haddon, R. Laudise, A. Lovinger, H. Katz, P. Bridenbaugh, and D. Davis, J. Mater. Res. **10**, 2170 (1995): *The crystal structure of the high-temperature polymorph of α-hexathienyl (α-6T/HT).*

[145] P. Lang, M. E. Ardhaoui, J. Wittmann, J. Dallas, G. Horowitz, B. Lotz, F. Garnier, and C. Straupe, Synth. Met. **84**, 605 (1997): *Substrate Dependent Orientation and Structure of Sexithiophene Thin Films.*

[146] M. A. Loi, E. D. Como, F. Dinelli, M. Murgia, R. Zamboni, F. Biscarini, and M. Muccini, Nat. Mater. **4**, 81 (2005): *Supramolecular organization in ultra-thin films of α-sexithiophene on silicon dioxide.*

[147] J. Ivanco, J. R. Krenn, M. G. Ramsey, F. P. Netzer, T. Haber, R. Resel, A. Haase, B. Stadlober, and G. Jakopic, J. Appl. Phys. **96**, 2716 (2004): *Sexithiophene films on clean and oxidized Si(111) surfaces: Growth and electronic structure.*

[148] R. Garcia, M. Tello, J. F. Moulin, and F. Biscarini, Nano Lett. **4**, 1115 (2004): *Size and Shape Controlled Growth of Molecular Nanostructures on Silicon Oxide Templates.*

[149] D. Oelkrug, H.-J. Egelhaaf, and J. Haiber, Thin Solid Films **284-285**, 267 (1996): *Electronic spectra of self-organized oligothiophene films with "standing" and "lying" molecular units.*

[150] J. Ivanco, T. Haber, J. Krenn, F. Netzer, R. Resel, and M. Ramsey, Surf. Sci. **601**, 178 (2007): *Sexithiophene films on ordered and disordered TiO_2(110) surfaces: Electronic, structural and morphological properties.*

[151] T. Haber, J. Ivanco, M. Ramsey, and R. Resel, J. Cryst. Growth **310**, 101 (2008): *Epitaxial growth of sexithiophene on TiO_2 (110).*

[152] M. Ardhaoui, P. Lang, J. Wittmann, B. Lotz, and F. Garnier, Synth. Met. **101**, 526 (1999): *Structure organization of sexithiophene vapour deposited onto HOPG and SiH/Si(111).*

[153] F. Biscarini, R. Zamboni, P. Samorí, P. Ostoja, and C. Taliani, Phys. Rev. B **52**, 14868 (1995): *Growth of conjugated oligomer thin films studied by atomic-force microscopy.*

[154] M. Muccini, M. Murgia, and F. Biscarini, Adv. Mater. **13**, 355 (2001): *Morphology Controlled Energy Transfer in Conjugated Molecular Thin Films.*

[155] C. Simbrunner, G. Hernandez-Sosa, M. Oehzelt, T. Djuric, I. Salzmann, M. Brinkmann, G. Schwabegger, I. Watzinger, H. Sitter, and R. Resel, Phys. Rev. B **83**, 115443 (2011): *Epitaxial growth of sexithiophene on mica surfaces.*

[156] G. Schwabegger, T. Djuric, H. Sitter, R. Resel, and C. Simbrunner, Cryst. Growth Des. **13**, 536 (2013): *Morphological and Structural Investigation of Sexithiophene Growth on KCl (100).*

[157] M. Oehzelt, S. Berkebile, G. Koller, J. Ivanco, S. Surnev, and M. Ramsey, Surf. Sci. **603**, 412 (2009): *α-Sexithiophene on Cu(1 1 0) and Cu(1 1 0)-(2 $\times$ 1)O: An STM and NEXAFS study.*

[158] M. Koini, T. Haber, S. Berkebile, G. Koller, M. Ramsey, R. Resel, and M. Oehzelt, J. Cryst. Growth **311**, 1364 (2009): *Growth of sexithiophene crystals on Cu(110) and Cu(110)-(2$\times$1)O stripe phase - The influence of surface corrugation.*

[159] S. Prato, L. Floreano, D. Cvetko, V. De Renzi, A. Morgante, S. Modesti, F. Biscarini, R. Zamboni, and C. Taliani, J. Phys. Chem. B **103**, 7788 (1999): *Anisotropic ordered planar growth of α-sexithienyl thin films.*

[160] M. Kiguchi, G. Yoshikawa, and K. Saiki, J. Appl. Phys. **94**, 4866 (2003): *Temperature and thickness dependence of molecular orientation of α-sexithienyl on Cu(111).*

[161] M. Kiguchi, G. Yoshikawa, S. Ikeda, and K. Saiki, Surf. Sci. **566-568**, 603 (2004): *Molecular orientation control of sexithienyl thin film on Cu substrates.*

[162] G. Yoshikawa, M. Kiguchi, S. Ikeda, and K. Saiki, Surf. Sci. **559**, 77 (2004): *Molecular orientations and adsorption structures of α-sexithienyl thin films grown on Ag(110) and Ag(111) surfaces.*

[163] E. Osawa, Kagaku (Kyoto) **25**, 854 (1970): *Superaromaticity.*

[164] E. Osawa, H. W. Kroto, P. W. Fowler, and E. Wasserman, Philosophical Transactions of the Royal Society A: Mathematical, Physical and Engineering Sciences **343**, 1 (1993): *The Evolution of the Football Structure for the C_{60} Molecule: A Retrospective [and Discussion].*

[165] H. W. Kroto, J. R. Heath, S. C. O'Brien, R. F. Curl, and R. E. Smalley, Nature **318**, 162 (1985): *C_{60}: Buckminsterfullerene.*

[166] H. W. Kroto, A. W. Allaf, and S. P. Balm, Chem. Rev. **91**, 1213 (1991): *C_{60}: Buckminsterfullerene.*

[167] D. Jariwala, V. K. Sangwan, L. J. Lauhon, T. J. Marks, and M. C. Hersam, Chem. Soc. Rev. **42**, 2824 (2013): *Carbon nanomaterials for electronics, optoelectronics, photovoltaics, and sensing.*

[168] S. Yang, C. Pettiette, J. Conceicao, O. Cheshnovsky, and R. Smalley, Chem. Phys. Lett. **139**, 233 (1987): *Ups of buckminsterfullerene and other large clusters of carbon.*

[169] A. Skumanich, Chem. Phys. Lett. **182**, 486 (1991): *Optical absorption spectra of carbon 60 thin films from 0.4 to 6.2 eV.*

[170] W. Krätschmer, L. D. Lamb, K. Fostiropoulos, and D. R. Huffman, Nature **347**, 354 (1990): *Solid C_{60}: a new form of carbon.*

[171] J. L. de Boer, S. van Smaalen, V. Petricek, M. Dusek, M. A. Verheijen, and G. Meijer, Chem. Phys. Lett. **219**, 469 (1994): *Hexagonal close-packed C_{60}.*

[172] P. A. Heiney, J. E. Fischer, A. R. McGhie, W. J. Romanow, A. M. Denenstein, J. P. McCauley Jr., A. B. Smith, and D. E. Cox, Phys. Rev. Lett. **66**, 2911 (1991): *Orientational ordering transition in solid C_{60}.*

[173] W. I. F. David, R. M. Ibberson, J. C. Matthewman, K. Prassides, T. J. S. Dennis, J. P. Hare, H. W. Kroto, R. Taylor, and D. R. M. Walton, Nature **353**, 147 (1991): *Crystal structure and bonding of ordered C_{60}.*

[174] Q.-M. Zhang, J.-Y. Yi, and J. Bernholc, Phys. Rev. Lett. **66**, 2633 (1991): *Structure and dynamics of solid C_{60}.*

[175] T. B. Singh, N. S. Sariciftci, H. Yang, L. Yang, B. Plochberger, and H. Sitter, Appl. Phys. Lett. **90**, 213512 (2007): *Correlation of crystalline and structural properties of C_{60} thin films grown at various temperature with charge carrier mobility.*

[176] A. Hinderhofer, A. Gerlach, K. Broch, T. Hosokai, K. Yonezawa, K. Kato, S. Kera, N. Ueno, and F. Schreiber, J. Phys. Chem. C **117**, 1053 (2013): *Geometric and electronic structure of templated C_{60} on diindenoperylene thin films.*

[177] M. A. Heinrich, J. Pflaum, A. K. Tripathi, W. Frey, M. L. Steigerwald, and T. Siegrist, J. Phys. Chem. C **111**, 18878 (2007): *Enantiotropic Polymorphism in Di-indenoperylene.*

[178] S. Kowarik, A. Gerlach, S. Sellner, L. Cavalcanti, O. Konovalov, and F. Schreiber, Appl. Phys. A **95**, 233 (2009): *Real-time X-ray diffraction measurements of structural dynamics and polymorphism in diindenoperylene growth.*

[179] A. C. Dürr, N. Koch, M. Kelsch, A. Rühm, J. Ghijsen, R. L. Johnson, J.-J. Pireaux, J. Schwartz, F. Schreiber, H. Dosch, and A. Kahn, Phys. Rev. B **68**, 115428 (2003): *Interplay between morphology, structure, and electronic properties at diindenoperylene-gold interfaces.*

[180] B. Krause, F. Schreiber, H. Dosch, A. Pimpinelli, and O. H. Seeck, Europhys. Lett. **65**, 372 (2004): *Temperature dependence of the 2D-3D transition in the growth of PTCDA on Ag(111): A real-time X-ray and kinetic Monte Carlo study.*

[181] U. Heinemeyer, K. Broch, A. Hinderhofer, M. Kytka, R. Scholz, A. Gerlach, and F. Schreiber, Phys. Rev. Lett. **104**, 257401 (2010): *Real-Time Changes in the Optical Spectrum of Organic Semiconducting Films and Their Thickness Regimes during Growth.*

[182] C. Frank, J. Novák, R. Banerjee, A. Gerlach, F. Schreiber, A. Vorobiev, and S. Kowarik, Phys. Rev. B **90**, 045410 (2014): *Island size evolution and molecular diffusion during growth of organic thin films followed by time-resolved specular and off-specular scattering.*

[183] P. R. Willmott, D. Meister, S. J. Leake, M. Lange, A. Bergamaschi, M. Böge, M. Calvi, C. Cancellieri, N. Casati, A. Cervellino, Q. Chen, C. David, U. Flechsig, F. Gozzo, B. Henrich, S. Jäggi-Spielmann, B. Jakob, I. Kalichava, P. Karvinen, J. Krempasky, A. Lüdeke, R. Lüscher, S. Maag, C. Quitmann, M. L. Reinle-Schmitt, T. Schmidt, B. Schmitt, A. Streun, I. Vartiainen, M. Vitins, X. Wang, and R. Wullschleger, J. Synchrotron Radiat. **20**, 667 (2013): *The Materials Science beamline upgrade at the Swiss Light Source.*

[184] M. Björck and G. Andersson, J. Appl. Cryst. **40**, 1174 (2007): *GenX: An extensible X-ray reflectivity refinement program utilizing differential evolution.*

[185] A. Farahzadi, P. Niyamakom, M. Beigmohamadi, N. Meyer, D. Keiper, M. Heuken, F. Ghasemi, M. R. R. Tabar, T. Michely, and M. Wuttig, Europhys. Lett. **90**, 10008 (2010): *Stochastic analysis on temperature-dependent roughening of amorphous organic films.*

[186] A. C. Dürr, F. Schreiber, M. Münch, N. Karl, B. Krause, V. Kruppa, and H. Dosch, Appl. Phys. Lett. **81**, 2276 (2002): *High structural order in thin films of the organic semiconductor diindenoperylene.*

[187] C. D. Dimitrakopoulos, A. R. Brown, and A. Pomp, J. Appl. Phys. **80**, 2501 (1996): *Molecular beam deposited thin films of pentacene for organic field effect transistor applications.*

[188] I. Bouchoms, W. Schoonveld, J. Vrijmoeth, and T. Klapwijk, Synth. Met. **104**, 175 (1999): *Morphology identification of the thin film phases of vacuum evaporated pentacene on SiO_2 substrates.*

[189] G. Witte and C. Wöll, J. Mater. Res. **19**, 1889 (2004): *Growth of aromatic molecules on solid substrates for applications in organic electronics.*

[190] A. Hinderhofer, U. Heinemeyer, A. Gerlach, S. Kowarik, R. M. J. Jacobs, Y. Sakamoto, T. Suzuki, and F. Schreiber, J. Chem. Phys. **127**, 194705 (1 (2007): *Optical properties of pentacene and perfluoropentacene thin films.*

[191] F. Liscio, C. Albonetti, K. Broch, A. Shehu, S. D. Quiroga, L. Ferlauto, C. Frank, S. Kowarik, R. Nervo, A. Gerlach, S. Milita, F. Schreiber, and F. Biscarini, ACS Nano **7**, 1257 (2013): *Molecular Reorganization in Organic Field-Effect Transistors and Its Effect on Two-Dimensional Charge Transport Pathways.*

[192] C. Lorch, R. Banerjee, J. Dieterle, A. Hinderhofer, A. Gerlach, J. Drnec, and F. Schreiber, J. Phys. Chem. C, **accepted**, (2015): *Templating Effects of α-Sexithiophene in Donor-Acceptor Organic Thin Films.*

[193] J. Sakai, T. Taima, T. Yamanari, and K. Saito, Solar Energy Materials and Solar Cells **93**, 1149 (2009): *Annealing effect in the sexithiophene:C_{70} small molecule bulk heterojunction organic photovoltaic cells.*

[194] A. Dodabalapur, H. E. Katz, L. Torsi, and R. C. Haddon, Science **269**, 1560 (1995): *Organic heterostructure field-effect transistors.*

[195] H. Huang, W. Chen, L. Chen, H. L. Zhang, X. S. Wang, S. N. Bao, and A. T. S. Wee, Appl. Phys. Lett. **92**, 023105 (2008): *"Zigzag" C_{60} chain arrays.*

[196] J. Niederhausen, P. Amsalem, A. Wilke, R. Schlesinger, S. Winkler, A. Vollmer, J. P. Rabe, and N. Koch, Phys. Rev. B **86**, 081411 (2012): *Doping of C_{60} (sub)monolayers by Fermi-level pinning induced electron transfer.*

[197] P. Amsalem, J. Niederhausen, A. Wilke, G. Heimel, R. Schlesinger, S. Winkler, A. Vollmer, J. P. Rabe, and N. Koch, Phys. Rev. B **87**, 035440 (2013): *Role of charge transfer, dipole-dipole interactions, and electrostatics in Fermi-level pinning at a molecular heterojunction on a metal surface.*

[198] A. Hinderhofer, T. Hosokai, C. Frank, J. Novák, A. Gerlach, and F. Schreiber, J. Phys. Chem. C **115**, 16155 (2011): *Templating effect for organic heterostructure film growth: Perfluoropentacene on diindenoperylene.*

[199] C. S. Yannoni, P. P. Bernier, D. S. Bethune, G. Meijer, and J. R. Salem, J. Am. Chem. Soc. **113**, 3190 (1991): *NMR determination of the bond lengths in C60.*

[200] G. B. Adams, J. B. Page, O. F. Sankey, K. Sinha, J. Menendez, and D. R. Huffman, Phys. Rev. B **44**, 4052 (1991): *First-principles quantum molecular-dynamics study of the vibrations of icosahedral C_{60}.*

[201] S. Bommel, N. Kleppmann, C. Weber, H. Spranger, P. Schäfer, J. Novák, S. Roth, F. Schreiber, S. Klapp, and S. Kowarik, Nat. Comm. **5**, 5388 (2014): *Unravelling the multilayer growth of the fullerene C_{60} in real time.*

[202] C. Ponchut, J. M. Rigal, J. Clément, E. Papillon, A. Homs, and S. Petitdemange, J. Inst. **6**, C01069 (2011): *MAXIPIX, a fast readout photon-counting X-ray area detector for synchrotron applications.*

[203] I. Salzmann, S. Duhm, R. Opitz, R. L. Johnson, J. P. Rabe, and N. Koch, J. Appl. Phys. **104**, 114518 (2008): *Structural and electronic properties of pentacene-fullerene heterojunctions.*

[204] C. Lorch, K. Broch, V. Belova, G. Duva, A. Hinderhofer, A. Gerlach, M. Jankowski, and F. Schreiber, Cryst. Growth. Des. **submitted**, (2015): *Growth and Annealing Kinetics of α-Sexithiophene and Fullerene C_{60} Mixed Films.*

[205] J. Sakai, T. Taima, and K. Saito, Organic Electronics **9**, 582 (2008): *Efficient oligothiophene:fullerene bulk heterojunction organic photovoltaic cells.*

[206] P. Peumans, S. Uchida, and S. R. Forrest, Nature **425**, 158 (2003): *Efficient bulk heterojunction photovoltaic cells using small-molecular-weight organic thin films.*

[207] F. Yang, M. Shtein, and S. R. Forrest, Nat. Mater. **4**, 37 (2005): *Controlled growth of a molecular bulk heterojunction photovoltaic cell.*

[208] R. Hamilton, C. G. Shuttle, B. O. Regan, T. C. Hammant, J. Nelson, and J. R. Durrant, J. Phys. Chem. Lett. **1**, 1432 (2010): *Recombination in Annealed and Nonannealed Polythiophene/Fullerene Solar Cells: Transient Photovoltage Studies versus Numerical Modeling.*

[209] R. Prabakaran, R. Kesavamoorthy, G. Reddy, and F. Xavier, phys. stat. sol. (b) **229**, 1175 (2002): *Structural Investigation of Copper Phthalocyanine Thin Films Using X-Ray Diffraction, Raman Scattering and Optical Absorption Measurements.*

[210] S. Heutz, G. Salvan, T. S. Jones, and D. R. T. Zahn, Adv. Mater. **15**, 1109 (2003): *Effects of Annealing on the Pproperties of Molecular Thin Film Heterostructures.*

[211] R. Ye, M. Baba, K. Ohta, and K. Suzuki, Solid-State Electron. **54**, 710 (2010): *Effects of thermal annealing on structure, morphology and electrical properties of $F_{16}CuPc/\alpha 6T$ heterojunction thin films.*

[212] M. Nothaft and J. Pflaum, phys. stat. sol. (b) **245**, 788 (2008): *Thermally and seed-layer induced crystallization in rubrene thin films.*

[213] A. Hinderhofer, T. Hosokai, K. Yonezawa, A. Gerlach, K. Kato, K. Broch, C. Frank, J. Novák, S. Kera, N. Ueno, and F. Schreiber, Appl. Phys. Lett. **101**, 033307 (2012): *Post-growth surface smoothing of thin films of diindenoperylene.*

[214] S. Yim and T. S. Jones, Appl. Phys. Lett. **94**, 021911 (2009): *Growth dynamics of C_{60} thin films: Effect of molecular structure.*

[215] K. Itaka, M. Yamashiro, J. Yamaguchi, M. Haemori, S. Yaginuma, Y. Matsumoto, M. Kondo, and H. Koinuma, Adv. Mater. **18**, 1713 (2006): *High-Mobility C_{60} Field-Effect Transistors Fabricated on Molecular- Wetting Controlled Substrates.*

[216] J. Q. Zhong, H. Huang, H. Y. Mao, R. Wang, S. Zhong, and W. Chen, J. Chem. Phys. **134**, 154706 (2011): *Molecular-scale investigation of C_{60}/p-sexiphenyl organic heterojunction interface.*

[217] J. Brock, J. Ferguson, and A. Woll, Metall. Mater. Trans. A **41**, 1162 (2010): *X-Ray Scattering Studies of the Surface Structure of Complex Oxide Films during Layer-by-Layer Growth via Pulsed Laser Deposition.*

[218] S. Roobol, W. Onderwaater, J. Drnec, R. Felici, and J. Frenken, J. Appl. Crystallogr. **48**, 1324 (2015): *BINoculars: data reduction and analysis software for two-dimensional detectors in surface X-ray diffraction.*

[219] J. Drnec, T. Zhou, S. Pintea, W. Onderwaater, E. Vlieg, G. Renaud, and R. Felici, J Appl Crystallogr **47**, 365 (2014): *Integration techniques for surface X-ray diffraction data obtained with a two-dimensional detector.*

[220] L. Pithan, C. Cocchi, H. Zschiesche, C. Weber, A. Zykov, S. Bommel, S. J. Leake, P. Schäfer, C. Draxl, and S. Kowarik, Cryst. Growth Des. **15**, 1319 (2015): *Light Controls Polymorphism in Thin Films of Sexithiophene.*

[221] S. M. Bayliss, S. Heutz, G. Rumbles, and T. S. Jones, Phys. Chem. Chem. Phys. **1**, 3673 (1999): *Thin film properties and surface morphology of metal free phthalocyanine films grown by organic molecular beam deposition.*

[222] S. Heutz, S. M. Bayliss, R. L. Middleton, G. Rumbles, and T. S. Jones, J. Phys. Chem. B **104**, 7124 (2000): *Polymorphism in Phthalocyanine Thin Films: Mechanism of the $\alpha \rightarrow \beta$ Transition.*

[223] S. Yim, S. Heutz, and T. S. Jones, J. Appl. Phys. **91**, 3632 (2002): *Model for the $\alpha \rightarrow \beta_1$ phase transition in phthalocyanine thin films.*

[224] C. Lorch, H. Frank, R. Banerjee, A. Hinderhofer, A. Gerlach, G. Li Destri, and F. Schreiber, Appl. Phys. Lett. **107**, 201903, (2015): *Controlling Length-Scales of the Phase Separation to Optimize Organic Semiconductor Blends.*

[225] T. Michely and J. Krug, Springer (Berlin), *Islands, Mounds, and Atoms. Patterns and Processes in Crystal Growth Far from Equilibrium* (2004).

[226] J. Yang, D. Yan, and T. S. Jones, Chem. Rev. **115**, 5570 (2015): *Molecular Template Growth and Its Applications in Organic Electronics and Optoelectronics.*

[227] D. Kurrle and J. Pflaum, Appl. Phys. Lett. **92**, 133306 (2008): *Exciton diffusion length in the organic semiconductor diindenoperylene.*

[228] P. Peumans and S. R. Forrest, Appl. Phys. Lett. **79**, 126 (2001): *Very-high-efficiency double-heterostructure copper phthalocyanine/C_{60} photovoltaic cells.*

[229] M. Riede, T. Mueller, W. Tress, R. Schueppel, and K. Leo, Nanotechnology **19**, 424001 (2008): *Small-molecule solar cells - status and perspectives.*

[230] S. Schinzer, M. Sokolowski, M. Biehl, and W. Kinzel, Phys. Rev. B **60**, 2893 (1999): *Unconventional MBE strategies from computer simulations for optimized growth conditions.*

[231] T. Wagner, D. R. Fritz, and P. Zeppenfeld, Org. Electron. **12**, 442 (2011): *Standing and Flat Lying α-6T Molecules Probed by Imaging Photoelectron Spectroscopy.*

[232] P. Peumans, A. Yakimov, and S. R. Forrest, J. Appl. Phys. **93**, 3693 (2003): *Small molecular weight organic thin-film photodetectors and solar cells.*

[233] M. Baldo, M. Deutsch, P. Burrows, H. Gossenberger, M. Gerstenberg, V. Ban, and S. Forrest, Adv. Mater. **10**, 1505 (1998): *Organic Vapor Phase Deposition.*

[234] A. Lopez-Otero, Thin Solid Films **49**, 3 (1978): *Hot wall epitaxy.*

[235] C. Lorch, J. Novák, R. Banerjee, S. Weimer, J. Dieterle, C. Frank, A. Hinderhofer, A. Gerlach, F. Carla, and F. Schreiber, **in preparation**, (2015): *Growth Behavior of Non-Equimolar Mixtures of Sterically Incompatible Organic Semiconductors.*

[236] *X-ray and Neutron Reflectivity : Principles and Applications*, Vol. 58 of *Lecture notes in physics*, Springer (Berlin), edited by Jean Daillant and Alain Gibaud (1999).

[237] C. L. Nicklin, C. Norris, P. Steadman, J. S. G. Taylor, and P. B. Howes, Physica B **221**, 86 (1996): *The growth of Sm on Mo(110) studied by surface X-ray diffraction.*

[238] E. Vlieg, A. W. Denier van der Gon, and J. F. van der Veen, Phys. Rev. Lett. **61**, 2241 (1988): *Surface X-ray Scattering During Crystal Growth: Ge on Ge(111).*

[239] S. K. Sinha, J. Phys. III France **4**, 1543 (1994): *X-ray diffuse scattering as a probe for thin film and interface structure.*

[240] T. Breuer and G. Witte, ACS Appl. Mater. Interfaces **5**, 9740 (2013): *Diffusion-Controlled Growth of Molecular Heterostructures: Fabrication of Two-, One-, and Zero-Dimensional C_{60}-Nanostructures on Pentacene Substrates.*

[241] J. E. Goose, E. L. First, and P. Clancy, Phys. Rev. B **81**, 205310 (2010): *Nature of step-edge barriers for small organic molecules.*

[242] X. Zhang, E. Barrena, D. de Oteyza, and H. Dosch, Surf. Sci. **601**, 2420 (2007): *Transition from layer-by-layer to rapid roughening in the growth of DIP on SiO_2.*

[243] Y.-T. Fu, C. Risko, and J.-L. Brédas, Adv. Mater. **25**, 878 (2013): *Intermixing at the Pentacene-Fullerene Bilayer Interface: A Molecular Dynamics Study.*

[244] C. Poelking, M. Tietze, C. Elschner, S. Olthof, D. Hertel, B. Baumeier, F. Würthner, K. Meerholz, K. Leo, and D. Andrienko, Nat. Mater. **14**, 434 (2015): *Impact of mesoscale order on open-circuit voltage in organic solar cells.*

[245] B. P. Rand, D. P. Burk, and S. R. Forrest, Phys. Rev. B **75**, 115327 (2007): *Offset energies at organic semiconductor heterojunctions and their influence on the open-circuit voltage of thin-film solar cells.*

[246] H.-J. Egelhaaf, P. Bäuerle, K. Rauer, V. Hoffmann, and D. Oelkrug, J. Mol. Struct. **293**, 249 (1993): *UV/Vis and IR spectroscopic studies on molecular orientation in ultrathin films of polythiophene model compounds.*

[247] V. I. Arkhipov, P. Heremans, and H. Bässler, Appl. Phys. Lett. **82**, 4605 (2003): *Why is exciton dissociation so efficient at the interface between a conjugated polymer and an electron acceptor?*

[248] M. Koehler, M. C. Santos, and M. G. E. da Luz, J. Appl. Phys. **99**, 053702 (2006): *Positional disorder enhancement of exciton dissociation at donor/acceptor interface.*

[249] Y. Yi, V. Coropceanu, and J.-L. Brédas, J. Am. Chem. Soc. **131**, 15777 (2009): *Exciton-Dissociation and Charge-Recombination Processes in Pentacene/C_{60} Solar Cells: Theoretical Insight into the Impact of Interface Geometry.*

[250] J. Xue, B. Rand, S. Uchida, and S. Forrest, Adv. Mater. **17**, 66 (2005): *A Hybrid Planar-Mixed Molecular Heterojunction Photovoltaic Cell.*

[251] H. Hamaker, Physica **4**, 1058 (1937): *The London - van der Waals attraction between spherical particles.*

[252] A. C. Mayer, R. Ruiz, R. L. Headrick, A. Kazimirov, and G. G. Malliaras, Org. Electron. **5**, 257 (2004): *Early stages of pentacene film growth on silicon oxide.*

[253] S. Kowarik, A. Gerlach, S. Sellner, F. Schreiber, J. Pflaum, L. Cavalcanti, and O. Konovalov, Phys. Chem. Chem. Phys. **8**, 1834 (2006): *Anomalous roughness evolution of rubrene thin films observed in real time during growth.*

List of Publications

- C. Lorch, J. Novák, S. Weimer, R. Banerjee, C. Frank, A. Hinderhofer, A. Gerlach, F. Carla, and F. Schreiber, **in preparation**: *Growth Behavior of Non-Equimolar Mixtures of Sterically Incompatible Organic Semiconductors*

- C. Lorch, K. Broch, V. Belova, G. Duva, A. Hinderhofer, A. Gerlach, M. Jankowski, and F. Schreiber, **submitted to J. Appl. Cryst.**: *Growth and Annealing Kinetics of α-Sexithiophene and Fullerene C_{60} Mixed Films.*

- C. Lorch, H. Frank, R. Banerjee, A. Hinderhofer, A. Gerlach, G. Li Destri and F. Schreiber, Appl. Phys. Lett. **107**, 201903 (2015): *Controlling Length Scales of the Phase Separation to Optimize Organic Semiconductor Blends.*

- A. Opitz, R. Banerjee, S. Grob, M. Gruber, A. Hinderhofer, U. Hörmann, J. Kraus, T. Linderl, C. Lorch, A. Steindamm, A.-K. Topczak, A. Wilke, N. Koch, J. Pflaum, F. Schreiber, and W. Brütting, **in preparation** Bookchapter: *Charge Separation at Nanostructured Molecular Donor-Acceptor interfaces in Elementary Processes of Organic Photovoltaics*, Advances in Polymer Science.

- C. Lorch, R. Banerjee, J. Dieterle, A. Hinderhofer, J. Drnec, A. Gerlach, and F. Schreiber, . Phys. Chem. C **119**, 23211 (2015): *Templating Effects of α-Sexithiophene in Donor-Acceptor Organic Thin Films.*

- T. Hosokai, A. Hinderhofer, F. Bussolotti, K. Yonezawa,C. Lorch, T. Watanabe, A. Vorobiev, Y. Hasegawa, Y. Yamada, Y. Kubozono, A. Gerlach, S. Kera, F. Schreiber, N. Ueno, J. Phys. Chem. C **119**, 29027 (2015): *Picene thin film growth and electronic structure on inert surfaces*

- C. Lorch, R. Banerjee, C. Frank, J. Dieterle, A. Hinderhofer, A. Gerlach, and F. Schreiber, J. Phys. Chem. C **119**, 819 (2015): *Growth of competing crystal phases of α-sexithiophene studied by real-time X-ray scattering.*

- S. Grob, A. N. Bartynski, A. Opitz, M. Gruber, F. Grassl, E. Meister, T. Linderl, U. Hörmann, C. Lorch, E. Moons, F. Schreiber, M. E. Thompson, and W. Brütting. J. Mater. Chem. A **3**, 15700 (2015): *Solvent Vapor Annealing on Perylene-Based Organic Solar Cells.*

- U. Hörmann, C. Lorch, A. Hinderhofer, A. Gerlach, M. Gruber, J. Kraus, B. Sykora, S. Grob, T. Linderl, A. Wilke, A. Opitz, R. Hansson, A. S. Anselmo, Y. Ozawa, Y. Nakayama, H. Ishii, N. Koch, E. Moons, F. Schreiber, and W. Brütting, J. Phys. Chem. C **118**, 26462 (2014): *V_{OC} from a morphology point of view: the Influence of molecular orientation on the open circuit voltage of organic planar heterojunction solar cells.*

- D. Gollmer, F. Walter, C. Lorch, J. Novák, R. Banerjee, J. Dieterle, G. Santoro, F. Schreiber, D. Kern, and M. Fleischer, Microelectron. Eng. **119**, 122 (2014): *Fabrication and characterization of combined metallic nanogratings and ITO electrodes for organic photovoltaic cells.*

- R. Banerjee, J. Novák, C. Frank, C. Lorch, A. Hinderhofer, A. Gerlach, and F. Schreiber, Phys. Rev. Lett. **110**, 185506 (2013): *Evidence for Kinetically Limited Thickness Dependent Phase Separation in Organic Thin Film Blends.*

- K. Broch, A. Gerlach, C. Lorch, J. Dieterle, J. Novák, A. Hinderhofer, and F. Schreiber, J. Chem. Phys. **139**, 174709 (2013): *Structure formation in perfluoropentacene:diindenoperylene blends and its impact on transient effects in the optical properties studied in real-time during growth.*

- T. Hosokai, A. Hinderhofer, A. Vorobiev, C. Lorch, T. Watanabe, T. Koganezawa, A. Gerlach, N. Yoshimoto, Y. Kubozono, and F. Schreiber, Chem. Phys. Lett. **544**, 34 (2012): *In situ structural characterization of picene thin films by X-ray scattering: Vacuum versus O_2 atmosphere.*

Deutsche Zusammenfassung

Organische Halbleiter finden Verwendung in verschiedenen optoelektronischen Bauelementen, die interessante Alternativen und Ergänzungen zu herkömmlichen anorganischen Bauelementen darstellen. Insbesondere bei organischen Solarzellen spielt die Struktur und Morphologie der aktiven Schicht eine wichtige Rolle für die Effizienz. Grundsätzlich sind mindestens zwei organische Halbleiter notwendig, die entweder in einer planaren Struktur (sprich Material A auf Material B) oder in einer Mischung vorliegen müssen. Im Rahmen dieser Promotion wurde die Struktur von dünnen Filmen aus Materialien, die bereits erfolgreich für organische Solarzellen eingesetzt wurden, untersucht, namentlich α-Sexithiophen (6T), Diindenoperylene (DIP) und Buckminsterfulleren (C_{60}). Reine Filme, planare Strukturen und Mischungen wurden per organischer Molekularstrahldeposition (OMBD) hergestellt und die Struktur der Filme wurde hauptsächlich mittels Röntgenstreuexperimenten direkt während des Wachstums in Echtzeit untersucht, um auch vorübergehende Effekte erfassen zu können.
Beim Wachstum von 6T wurde gezeigt, dass zwei unterschiedliche Kristallstrukturen konkurrieren, wobei die eine, eher ungeordnete β-Struktur in der Nähe des Substrats dominiert, wohingegen ab einer bestimmten Filmdicke die andere LT-Struktur (vom Englischen: "low-temperature single crystal structure") überwiegt. Die Substrattemperatur während des Wachstums kann dafür genutzt werden, entweder die β-Struktur (bei einer Substrattemperatur um ca. 300 K) beziehungsweise die LT-Struktur (bei einer Substrattemperatur um ca. 370 K) zu fördern. Durch Tempern von Filmen, die bei 300 K hergestellt wurden (hauptsächlich β-Struktur), ist es möglich die Kristallinität deutlich zu verbessern und die β-Kristallite in solche der LT-Struktur umzuwandeln.
Bei Mischungen von 6T und C_{60} haben wir herausgefunden, dass C_{60} einen wichtigen Einfluss auf die Struktur des 6Ts (in der Mischung) hat. Bei Anwesenheit von C_{60} ist jeweils die Struktur noch stärker ausgeprägt, die ohnehin schon dominiert sogar in so einem Maße, dass die unterdrückte Struktur nahezu nicht mehr vorhanden ist. Bei hoher Substrattemperatur wurde dabei eine Umwandlung der β-Struktur in die LT-Struktur während des Wachstums beobachtet. Dafür ist ver-

mutlich C_{60} verantwortlich, das dem 6T zusätzliche Energie zur Verfügung stellt, damit dieses eine Energiebarriere überwinden kann um in die energetisch stabilere LT-Struktur überzugehen. Interessanterweise hat das Tempern dieser Filme im untersuchten Bereich (ähnlich zu dem für reine 6T Filme) keinen Einfluss auf die Struktur.
Wenn C_{60} oder DIP auf einer Unterlage von 6T gewachsen wird, ist ein starker Templateeffekt zu beobachten. So passt sich die Kristallitgröße von C_{60} und DIP an die des 6T an. Außerdem verbessert sich die Kristallinität von C_{60} deutlich im Vergleich zu dem Wachstum auf reinem Siliziumoxid. Für das DIP haben wir auÃ§erdem noch eine Anpassung der relativen Orientierung der Moleküle (liegende oder stehende Ausrichtung) an die Orientierung der 6T Moleküle beobachtet. Überraschend war der Effekt, dass sich die Struktur des fertig gewachsenen 6T Films während der Abscheidung des zweiten Materials geändert hat, sprich sowohl C_{60} als auch DIP haben die Struktur des 6T verändert. Daraus lässt sich schließen, dass jeder einzelne Prozessschritt einen wichtigen Einfluss auf die Struktur, auch von bereits gefertigten Schichten, haben kann.
Für das Mischungssystem aus DIP und C_{60} wurden nahezu alle Parameter untersucht, die verwendet werden können um die Struktur der Filme einzustellen. Bei Mischungen, die in organischen Solarzellen zum Einsatz kommen, ist vor allem das Maß der Phasenseparation relevant. Bis zu einer gewissen Längenskala, nämlich der Exzitonendiffusionslänge gilt: je größer, desto besser. Wir haben Methoden untersucht um diese Phasenseparation zu kontrollieren. Der wichtigste Parameter dabei ist die Substrattemperatur. Hohe Substrattemperaturen sorgen für ein höheres Maß an Entmischung. Ähnliche Effekte lassen sich aber auch durch Verringern der Aufdampfrate oder durch wiederholtes Unterbrechen und Wiederaufnehmen des Verdampfens erreichen, wenn bestimmte Bedingungen erfüllt sind. Genauso kann der Einsatz von dünnen organischen Schichten zwischen Substrat und Mischung einen positiven Einfluss auf den Entmischungsgrad haben.
Bei Mischungen aus DIP und C_{60} wurde auch eine Wachstumsart gefunden, die sehr nahe am perfekten Lage-für-Lage-Wachstum ist, was in sehr glatten Oberflächen resultiert.
Die Erkenntnisse, die über das Wachstum von planaren Strukturen und Mischungen organischer Halbleiter gefunden wurden, sind am Ende dieser Arbeit zusammengefasst. Außerdem werden Vorschläge gemacht, wie die Struktur speziell kontrolliert werden kann um die Effizienzen der einzelnen Prozessschritte, die bei der Umwandlung von Licht in freie Ladungsträger in organischen Solarzellen ablaufen, optimiert werden können.

Acknowledgment

Here, I want to thank all the people who helped that this thesis has become a success. Prof. Dr. Frank Schreiber was an excellent supervisor and I am deeply grateful for having had the opportunity to work on this interesting project and for his support.
Prof. Dr. Wolfgang Brütting is acknowledged for agreeing to survey this work and for the cooperation with him and his group.
I am also very grateful to the Carl-Zeiss-Stiftung for their financial support of my project.
Furthermore, I want to thank Dr. Alexander Gerlach, Dr. Alexander Hinderhofer and Dr. Rupak Banerjee for their help in the laboratory, fruitful discussions and their productive support during beamtimes.
This work would not have been possible without the experiments performed at several of the latter. For experimental assistance during beamtimes I am grateful to Dr. Katharina Broch, Valentina Belova, Johannes Dieterle, Dr. Christian Frank, Giuliano Duva, Heiko Frank and Simon Weimer. In addition, I want to thank the European Synchrotron Radiation Facility (ESRF) and the Paul Scherrer Institut - Swiss Light Source (SLS) for granting beamtimes and the staff of the ID03, the ID10 (both at the ESRF) and the MS-Surf. diffraction (SLS) beamlines for their excellent support. In this regard, I have to mention especially Dr. Jakub Drnec and Dr. Maciej Jankowski for their comments on manuscripts and helpful discussions.
Hanna Maurer, Aleksandra Rötschke and Sabine Ehrlich is thanked for their help with administrative tasks and Klaus Hagdorn-Wittern, Bernd Hofferberth and Bernhard Degel were a great support with their technical assistance. I also want to thank the rest of the research group, especially the OMBD part for their support and their encouragement and proofreading of manuscripts.

I also owe particular thanks to two people who accompanied me over the years: My parents! Thank you and the rest of my family who supported me throughout my entire life. Last but definitively far away from least I want to thank my girlfriend Silvia Klemm for her promotion, patience and especially the good times during the last few years.